

ANALYSIS OF SMART FUNCTIONALLY GRADED MATERIALS
USING AN IMPROVED THIRD ORDER SHEAR DEFORMATION THEORY

A Dissertation

by

JAMES WILSON ALIAGA SALAZAR

Submitted to the Office of Graduate Studies of
Texas A&M University
in partial fulfillment of the requirements for the degree of

DOCTOR OF PHILOSOPHY

August 2006

Major Subject: Mechanical Engineering

ANALYSIS OF SMART FUNCTIONALLY GRADED MATERIALS
USING AN IMPROVED THIRD ORDER SHEAR DEFORMATION THEORY

A Dissertation

by

JAMES WILSON ALIAGA SALAZAR

Submitted to the Office of Graduate Studies of
Texas A&M University
in partial fulfillment of the requirements for the degree of

DOCTOR OF PHILOSOPHY

Approved by:

Chair of Committee,	J.N Reddy
Committee Members,	Jose Roesset
	Ozden Ochoa
	Goong Chen
Head of Department,	Dennis L. O'Neal

August 2006

Major Subject: Mechanical Engineering

ABSTRACT

Analysis of Smart Functionally Graded Materials

Using an Improved Third Order Shear Deformation Theory. (August 2006)

James Wilson Aliaga Salazar, B.S., Universidad Nacional de Ingenieria, Lima, Peru;

M.S., Pontificia Universidade Catolica do Rio de Janeiro, Rio de Janeiro, Brazil

Chair of Advisory Committee: Dr. J.N Reddy

Smart materials are very important because of their potential applications in the biomedical, petroleum and aerospace industries. They can be used to build systems and structures that self-monitor to function and adapt to new operating conditions. In this study, we are mainly interested in developing a computational framework for the analysis of plate structures comprised of composite or functionally graded materials (FGM) with embedded or surface mounted piezoelectric sensors/actuators. These systems are characterized by thermo-electro-mechanical coupling, and therefore their understanding through theoretical models, numerical simulations, and physical experiments is fundamental for the design of such systems. Thus, the objective of this study was to perform a numerical study of smart material plate structures using a refined plate theory that is both accurate and computationally economical. To achieve this objective, an improved version of the Reddy third-order shear deformation theory of plates was formulated and its finite element model was developed. The theory and finite element model was evaluated in the context of static and dynamic responses without and with actuators. In the static part, the performance of the developed finite element model is compared with that of the existing models in determining the displacement and stress fields for composite laminates and FGM plates under mechanical and/or thermal loads. In the dynamic case, coupled and uncoupled

electro-thermo-mechanical analysis were performed to see the difference in the evolution of the mechanical, electrical and thermal fields with time. Finally, to test how well the developed theory and finite element model simulates the smart structural system, two different control strategies were employed: the negative velocity feedback control and the Least Quadratic Regulator (LQR) control. It is found that the refined plate theory provides results that are in good agreement with the those of the 3-D layerwise theory of Reddy. The present theory and finite element model enables one to obtain very accurate response of most composite and FGM plate structures with considerably less computational resources.

To Myself, but specially to themselves, Margarito!, Sergei!, of course you are part of them!

ACKNOWLEDGMENTS

I would like to express my deepest gratitude to the women of my life, Ana, Sofia and Rocio, my beloved mother, grandmother and sister, who were the industrious builders of my world.

My sincere thanks and appreciation to Professor J.N. Reddy, my advisor, for the opportunity to work for him and for his help, support, and patience during the last five years of my study at Texas A&M University.

I would like to express my sincere appreciation to Professor Jose Roesset for his comprehension and patience with me. I also wish to express my gratitude to Dr. Ozden Ochoa and Goong Cheng for serving on my committee and for their advice during the course this study.

TABLE OF CONTENTS

CHAPTER		Page
I	INTRODUCTION	1
	A. Overview	1
	B. Literature Review	5
	C. Objectives	9
	D. Description of the Work	11
II	GENERAL FORMULATION	13
	A. Multiple Assumed Displacement Fields	13
	1. Strain Field	20
	B. Improved ESL Deformation Theory	25
	1. Strain Field	28
	C. Electrical Field	30
	D. Thermal Field	34
	E. Fundamental Laws of Continuum Mechanics	41
	1. Conservation of Mass	41
	2. Linear Momentum Principle	42
	3. Angular Momentum Principle	43
	4. First Law of Thermodynamics	43
	5. Second Law of Thermodynamics	45
	F. Constitutive Equation	45
	G. Fully Coupled Finite Element Formulation	47
	1. Equation Terms	48
	a. $\int_V \delta u_u^T \rho \ddot{u}_u dV$	48
	b. $\int_V \delta \varepsilon^T \sigma dV$	49
	c. $\int_S \delta u^T \bar{q}_u$	51
	d. $-\int_V \delta E^T D dV$	51
	e. $\int_S \delta \phi q_\phi dS$	52
	f. $\int_V T \dot{\eta} \delta T dV$	53
	g. $\int_V \delta \Theta^T K \Theta dV$	54
	h. $-\int_S \{\delta u_\theta^e\}^T \bar{q}_\theta \cdot \hat{n} dS$	55
III	STATIC ANALYSIS	57
	A. Symmetric Composite Laminates	57

CHAPTER	Page
B. Composite Plate Laminates with Different Boundary Conditions	60
C. Functionally Graded Plates (FGM)	66
1. FGM Plate	66
a. Mechanical Load	70
b. Thermal Load	74
2. Smart FGM Plate	81
a. Mechanical Load	82
b. Thermal Load	88
c. Electrical Load	97
IV DYNAMIC ANALYSIS	107
A. Applications	109
1. FGM Plate	109
a. Mechanical Load	109
b. Thermal Load	110
2. Smart FGM Plate	114
a. Mechanical Load	114
b. Thermal Load	115
c. Electrical Load	120
V ACTIVE VIBRATION CONTROL OF SMART FGM PLATES	122
A. Negative Velocity Feedback	122
1. Application	123
B. Optimal Control	125
C. Linear Quadratic Regulator (LQR)	127
1. Choice of the Weighted State Matrix	128
2. Application	129
VI SUMMARY AND CONCLUSIONS	131
REFERENCES	134
APPENDIX A	141
APPENDIX B	142
VITA	146

LIST OF TABLES

TABLE	Page
I	Comparison of several formulations with the analytical solution proposed by Pagano 58
II	w and σ_{xx} of cross-ply square plates with various boundary conditions 64
III	σ_{yz} and σ_{xy} of cross-ply square plates with various boundary conditions 65
IV	\bar{u} and \bar{w} for a FGM plate under a sinusoidal mechanical load 68
V	$\bar{\sigma}_{xx}$ and $\bar{\sigma}_{xy}$ for a FGM plate under a mechanical sinusoidal load . . . 69
VI	$\bar{\sigma}_{yz}$ and $\bar{\sigma}_{zz}$ for a FGM plate under a sinusoidal mechanical load . . . 71
VII	\bar{u} and \bar{w} for a FGM plate under a sinusoidal thermal field 76
VIII	$\bar{\sigma}_{xx}$ and $\bar{\sigma}_{xy}$ for a FGM plate under a sinusoidal thermal field 77
IX	$\bar{\sigma}_{yz}$ and $\bar{\sigma}_{zz}$ for a FGM plate under a sinusoidal thermal field 78
X	\bar{u} and \bar{w} for a FGM plate under a sinusoidal mechanical load 83
XI	$\bar{\sigma}_{xx}$ and $\bar{\sigma}_{xy}$ for a FGM plate under a sinusoidal mechanical load . . . 84
XII	$\bar{\sigma}_{yz}$ and $\bar{\sigma}_{zz}$ for a FGM plate under a sinusoidal mechanical load . . . 85
XIII	\bar{u} for a FGM plate under a sinusoidal thermal field 89
XIV	\bar{w} for a FGM plate under a sinusoidal thermal field 90
XV	$\bar{\sigma}_{xx}$ for a FGM plate under a sinusoidal thermal field 91
XVI	$\bar{\sigma}_{xy}$ for a FGM plate under a sinusoidal thermal field 92
XVII	$\bar{\sigma}_{yz}$ for a FGM plate under a sinusoidal thermal field 93
XVIII	$\bar{\sigma}_{zz}$ for a FGM plate under a sinusoidal thermal field 94

TABLE	Page
XIX \bar{u} for a FGM plate under a sinusoidal electrical field	98
XX \bar{w} for a FGM plate under a sinusoidal electrical field	99
XXI σ_{xx} for a FGM plate under a sinusoidal electrical field	100
XXII σ_{xy} for a FGM plate under a sinusoidal electrical field	101
XXIII σ_{yz} for a FGM plate under a sinusoidal electrical field	102
XXIV σ_{zz} for a FGM plate under a sinusoidal electrical field	103

LIST OF FIGURES

FIGURE	Page
1	Multiple assumed displacement mechanism for the case where ESL is FSDT 14
2	Deformation of the transverse normal section according to CLPT, FSDT and TSDT 15
3	Displacement representation using the LWT and the linear Lagrangian interpolation function $\Phi^I(z)$ 18
4	Fixed volume V , bounded by the surface S 42
5	Linear momentum balance 43
6	\bar{w} through thickness for a composite plate under mechanical load . . 60
7	$\bar{\sigma}_{xx}$ through thickness for a composite plate under mechanical load . 61
8	$\bar{\sigma}_{yy}$ through thickness for a composite plate under mechanical load . 61
9	$\bar{\sigma}_{xz}$ through thickness for a composite plate under mechanical load . 62
10	$\bar{\sigma}_{yz}$ through thickness for a composite plate under mechanical load . 62
11	\bar{w} through thickness for a composite plate under mechanical load . . 63
12	\bar{w} through thickness for a FGM plate under mechanical load 72
13	$\bar{\sigma}_{xx}$ through thickness for a FGM plate under mechanical load 72
14	$\bar{\sigma}_{yz}$ through thickness for a FGM plate under mechanical load 73
15	$\bar{\sigma}_{zz}$ through thickness for a FGM plate under mechanical load 73
16	Central deflection along FGM plate length under mechanical load . . 74
17	\bar{w} through thickness for a FGM plate under thermal load 79

FIGURE	Page
18	$\bar{\sigma}_{xx}$ through thickness for a FGM plate under thermal load 79
19	$\bar{\sigma}_{yz}$ through thickness for a FGM plate under thermal load 80
20	$\bar{\sigma}_{zz}$ through thickness for a FGM plate under thermal load 80
21	Central deflection along the FGM plate length under thermal load . . 81
22	\bar{w} through thickness for a smart FGM plate under mechanical load . 86
23	$\bar{\sigma}_{xx}$ through thickness for a smart FGM plate under mechanical load 86
24	$\bar{\sigma}_{yz}$ through thickness for a smart FGM plate under mechanical load 87
25	$\bar{\sigma}_{zz}$ through thickness for a smart FGM plate under mechanical load 87
26	Central deflection along the smart FGM plate length under me- chanical load 88
27	\bar{w} through thickness for a smart FGM plate under thermal load . . . 95
28	$\bar{\sigma}_{xx}$ through thickness for a smart FGM plate under thermal load . . 95
29	$\bar{\sigma}_{yz}$ through thickness for a smart FGM plate under thermal load . . 96
30	$\bar{\sigma}_{zz}$ through thickness for a smart FGM plate under thermal load . . 96
31	Central deflection along the smart FGM plate length under ther- mal load 97
32	\bar{w} through thickness for a smart FGM plate under an applied voltage 104
33	$\bar{\sigma}_{xx}$ through thickness for a smart FGM plate under an applied voltage 104
34	$\bar{\sigma}_{yz}$ through thickness for a smart FGM plate under an applied voltage 105
35	$\bar{\sigma}_{zz}$ through thickness for a smart FGM plate under an applied voltage 105
36	Central deflection along the smart FGM plate length under an applied voltage 106
37	Time response of the center of the FGM plate for $a/h=4$ 110

FIGURE	Page
38	Time response of the center of the FGM plate for $a/h=10$ 111
39	Time response of the center of the FGM plate for $a/h=50$ 111
40	Time response of the center of the FGM plate when a thermal shock is imposed 112
41	Time response of the center of the FGM plate for an imposed thermal boundary condition 113
42	Temperature increase evolution on the center point of the middle plane of the plate for an imposed thermal boundary condition 114
43	Time response of the center of the smart FGM plate for $a/h=4$. . . 115
44	Time response of the center of the smart FGM plate for $a/h=10$. . . 116
45	Time response of the center of the smart FGM plate for $a/h=50$. . . 116
46	Voltage evolution in the middle plane of the sensor for $a/h=4$ 117
47	Voltage evolution in the middle plane of the sensor for $a/h=10$ 117
48	Voltage evolution in the middle plane of the sensor for $a/h=50$ 118
49	Time response of the center of the smart FGM plate when a thermal shock is imposed 118
50	Voltage evolution in the middle plane of the sensor when a thermal shock is imposed 119
51	Time response of the center of the smart FGM plate for an imposed thermal boundary condition 120
52	Time response of the center of the smart FGM plate for an imposed sinusoidal voltage distribution 121
53	Time responses at the top part of the center of the plate for different gain values G 124
54	Voltage history of the middle plane of the sensor for different gain values G 125

FIGURE	Page
55 Time responses at the top part of the center of the plate when LQR is used	130
56 Voltage history of the middle plane of the sensor when a LQR control is applied	130

CHAPTER I

INTRODUCTION

A. Overview

A smart structure is comprised of a basic structural part, which can be made of a composite or FGM material, and distributed sensors and actuators and a microprocessor. The microprocessor (electronic system) reads and analyzes the signal captured by the sensors and sends a feedback signal, based on an integrated control algorithm, to the actuators. The actuators apply localized strains to the structure in order to modify its current response. The sensors and actuators are normally surface mounted or embedded into the structure. The most common materials that are used as sensors or actuators are piezoelectric and electrostrictive materials, shape memory alloys, magnetostrictive materials, electro and magneto rheological fluids and optical fibers. A review of the characteristics of various commercially available piezoelectric, electrostrictive, and magnetostrictive materials can be found in [1]. A comparison in terms of the output energy density can be made as follows:

Smart structures have a wide range of applications such as vibration and noise control, aeroelastic stability, damping, shape change and stress-strain distribution. For these reasons, they have been widely used in automotive and aerospace systems, machine tools, and medical devices. Practical examples can be found in embedded or surface-bonded smart actuators in the fixed-wing of an airplane or rotary wing craft of a helicopter. Moreover, shape control of large flexible space structures, precision manufacturing machines and computer systems are also examples of smart structures.

In this research, we mainly focus on the computational modelling of smart plate

The journal model is Transactions of the ASME Journal of Applied Mechanics.

structures with piezoelectric sensors and actuators. These materials undergo deformation after applying an electric field across the plate thickness (*direct effect*). This deformation involves a very small strains but cover a wide range of actuation frequency. Conversely, piezoelectric materials produce voltage as an output when they are mechanically deformed (*converse effect*). These materials behave linearly at low fields and are bipolar, but exhibit hysteresis.

The piezoelectric actuators make use of the direct effect of the piezoelectricity. In other words, they convert the input voltage into a strain/displacement actuation, and then transmits this actuation to the main structure in order to modify its mechanical state. Consequently, an actuator has a good performance when we can get more stroke or strain for a specific voltage. In some cases, when we cannot reach the necessary actuation levels, hybrid configurations, which consist of adding viscoelastic layers to the structure, are employed. Other desirable characteristics for an actuator are high stiffness, wide bandwidth frequency range, linear behavior and compactness. Several materials with these properties are employed, among them, piezoceramics are widely used in practical applications.

Piezoceramics do not have piezoelectric effect in its original state; however, this effect is induced through the application of a high DC electric field. This process is called polarization. Among all the piezoceramics the most common one is the PZT, which is a solid solution mainly comprised of lead zirconate and lead titanate mixed with other components in order to obtain specific properties. The PZT in the form of sheets are attached or embedded in the base part of the smart structure. PZTs are considered isotropic.

The converse effect of the piezoelectricity is the principle that governs piezoelectric sensors. They convert a strain or displacement into an electrical field. In this case, a sensor possesses a good performance when it has high sensitivity to strain or

displacement. Similar to actuators, bandwidth, compactness, temperature sensitivity and linearity are important characteristics that determine the performance of a sensor. In the case of piezoelectric sensors, they have a superior signal-to-noise ratio and high-frequency noise rejection compared to other kind of sensors. Moreover, they generate signals with broad spectrum frequency. Other advantages are their compactness and sensitivity over a large strain bandwidth and ease of embedability. The most common material employed for sensors is piezofilm PVDF because of its low stiffness. Sometimes piezoceramic (PZT) sensors are used for specific applications such as in [2], [3], [4] [5] and [6].

There are two main fields to consider for piezoelectric sensors or actuators: the elastic and the electrical field. Adequate mechanical and electrical inputs along with suitable configurations will produce the desired global and local effects for the structural system. Moreover, thermal effects are present in almost all applications of smart structures and make enormous contributions as well. As a result, modelling smart structures is a challenging task. Among them, we mention the following.

- The configuration of piezoelectric sensors and actuators over a host structure are very diverse. In mechanical structures such as beams, plates and shells they can be located anywhere in the plane domain whether or not we want to increase the damping, stiffness or sense the behavior of the structure. Moreover, across the thickness, they can be either embedded in the structure or attached to the top and/or the bottom of its surface. Therefore, a flexible analysis, able to take account all the possible configurations should be implemented.
- Only some regions of the total analysis domain contain piezoelectric and in the case of hybrid configurations viscoelastic characteristics, too needs to be considered. Therefore, those are the regions where we have to study the electrical field

and all its possible couplings with the elastic, thermal and viscoelastic fields. For the rest of the structure only a thermo-elastic analysis must be performed. Hence, a convenient approach to tailor these problems is to carry out a sophisticated analysis in the regions where piezoelectric and viscoelastic materials are present. In other words, in these regions, we should employ sophisticated models that are able to capture all the physical mechanisms. Meanwhile, in the rest of the domain, simple models could be employed.

- The transverse shear effects are very important in smart structures, and, when we analyze smart materials, there are three important cases to be considered. The first one is when a plate or beam gets thicker. In this case, the deformation energy due to the shear effect is considerable. Second, in the analysis of the debonding process that might occur in the region between the piezoelectric material and the host structure. Consequently, an adequate stress analysis for this region is strongly required in order to preserve the integrity of the smart structure. The final case is when viscoelastic layers are attached to the main core of the structure. The main purpose of this is to increase the structural damping of the system. In this situation, the energy dissipated by the system is a consequence of the shear effects and a good description of these effects should be included in the mathematical model for smart structures.
- Vibration control in environments with high temperature gradients is one of the main applications of smart structures that have recently called the attention of researchers. Hence, an appropriate model for these kinds of problems has two important issues that must be addressed. The first one is the dynamical analysis since the elastic, electrical and thermal fields do change with time. The second one is the couplings between the elastic, electrical and thermal effect.

For instance, FGMs normally works at high temperatures and when they are combined with piezoelectric sheets to form a smart structure, the couplings of the thermal field with the elastic and electrical ones should not be neglected.

- To implement a feasible control algorithm for any kind of system, we must have a model that describes most of its effects with very few uncertainties and with the minimum number of parameters. In the case of smart structures, a suitable model must consider all the coupling between its different physical effects. Moreover, the shear effects must be included in the elastic field and also the nonlinearity caused by the large thermal gradients that the structure might undergo.

B. Literature Review

The first practical application for piezoelectric materials was during the World War II in the 1940s when they were employed as ultrasonic detectors for submarines. Later, a great variety of acoustical transducers were developed using these materials. However, only in the 1970s researchers started carrying out numerical analysis of the electrical and mechanical effects associated with the applications previously described. In [7] the authors implemented a tetrahedral element with 4 nodes, using a linear theory for both displacement and electric field. The nodal dofs are the displacements and the electric potential. This work represented a starting point for the use of solid finite elements in the analysis of smart structures. Another work in the same line was presented in [8] where the application focuses on the response of sonar transducer. One of the most important recent works using solid finite elements can be found in [9] where Hexahedral with 8 nodes, linear displacement plus quadratic incompatible modes and linear electric field was used. The main problem with this approach is that

use of a full 3-D strategy to solve problems related to 3-D elasticity theory requires a great number of dofs, and, hence it results in an expensive element for numerical analysis purposes. Therefore, some assumptions or different strategies to simplify the problem without sacrificing the accuracy of the result are expected.

A layerwise theory (LWT) is an interesting simplification of the 3-D elasticity theory. Moreover any finite element formulated using a LWT is more computational tractable than the ones originated from a fully 3-D elasticity approach. Several layerwise theories have been proposed in the literature; however among them, the one proposed by [10] expresses the displacement field in such manner that most of the 3-D elasticity features are included. In addition, this approach can be easily extended to describe the electrical field present in smart structures. This idea was successfully implemented in [11]. In [12], the authors have also developed some others interesting works using LWT where static condensation of the electrical dofs is included to reduce the number of equations to be solved.

Most of the mechanical structures have some of its dimensions comparatively smaller than its other ones, and depending of the loading condition, we can make some assumption that will simplify the 3-D elasticity equations. For example, in the case of beams, we neglect the width effects and the length to thickness ratio is relatively big. Researchers have devoted many efforts to study smart structures using beam models because of its simplicity and practical applicability. For instance, in [13], the authors used an Euler-Bernoulli model for a beam with surface-bonded or embedded induced strain actuators (symmetric actuation), considering that the mechanical and electrical field are uncoupled. After that, the made comparisons with others approaches such as uniform-strain model, a finite element model, and an experiment. This work is valid when the host structure is comprised of an isotropic material. However, in cases where the base structure is an anisotropic material, it requires a more detailed analysis. In

[14], the authors carried out a refined Finite Element Analysis for an anisotropic beam with embedded piezoelectric actuators. After that, they successfully compared their results with a three-dimensional beam model. These two previous works mostly neglects the shear effect on the structure; however, this effect should be considered. In works like [15], the first order shear deformation theory is employed (FSDT). This theory violates the traction-free boundary condition on the top and bottom surfaces. To compensate this anomaly, a shear correction factor is used. More refined theories to capture the nonlinear distribution of transverse shear strain across the thickness can be used. These theories, however, are unable to capture accurately a drastic change of properties at ply level. For this reason, works like [16] and [12] present a coupled layer-wise analysis of composite beams with embedded piezoelectric actuators and sensors. The main advantage of this theory is its capability to obtain consistent and more detailed stress distribution, especially near the end of the actuator. Until this point, all works have been devoted to explore beams with piezoelectric materials that use extensional actuation mechanism. Nevertheless, the shear mechanism mode has also been recently explored.

In [17], the authors proposed a unified beam finite element model for extension and shear piezoelectric actuation mechanism. This is especially suitable for sandwiched beams. The model used Euler-Bernoulli theory for the surface layers and Timoshenko beam theory for the core. It was shown that the predicted induced deformation was lower with the shear-actuated beam theory. In this case the shear forces are very important and they become the main part of the analysis when viscoelastic layers along with piezoelectric are attached to the structure to create a hybrid active and passive system for control of vibration. Works of [18], [19], [20] and [21] show advantages of this beam configuration, such as an efficient damping increase in the structure. Moreover, several beam and viscoelastic models were employed to analyze

this problem.

In the cases where the length and width of the structure have to be considered as the analysis domain and the thickness is small compared to them, the plate models have proved to be successful in representing the elastic field of the smart structures. For instance, [22], developed a plate formulation based on CLPT and analyzed anisotropic plates using the Ritz method. The authors validated their result with experimental data obtained by testing a cantilevered aluminum and a composite plate with surface-bonded piezoceramic actuators, attached to the whole top and bottom surfaces. Moreover, in [23] and [24], we can observe the bending analysis of composite plates using CLPT plate theory and linear actuation characteristics of piezoelectric laminas whose electrical degrees of freedom were condensed. In these two previous works, the shear effect over the thickness was neglected; however, similar to beams, this effect must be considered in order to perform an accurate analysis for smart structures. With this observation in mind, [25] and [26] have developed finite element formulation based on the first-order shear deformation plate theory (FSDT) assuming linear variation of the voltage through the thickness of the piezoelectric materials attached to the structure. Moreover, in [27] developed a shear locking-free quadrangular finite element using the FSDT. Using this element, the authors analyzed a plate with surface-bonded thin piezo-electric actuator for vibration-control purposes. Even though the models mentioned above yield satisfactory results, their accuracy tends to decrease when the plate gets thicker. To address this problem, Reddy [28, 29] developed a higher-order shear deformation plate theory to reproduce the quadratic variation of the shear strain through the plate thickness. Even though this variation satisfies the traction-free boundary condition on top and bottom surfaces, it cannot accurately represent layer-wise variation of shear strain caused by different material properties of laminae (all equivalent single-layer theories will have this limitation).

To overcome this problem, layerwise theories (LWT) for laminated plates have been developed and applied to smart structures (see [29], [30], [31] and [32]). In these works, different LWT were employed to address the problem.

In recent times, the study of smart plates was focused on analyzing the fully coupled, thermal, electrical and mechanical effects, in composite and functionally graded material (FGM) structures. A fully coupled static 3-D elastic analysis of smart functionally graded material can be found in [33]. In this work, an asymptotic expansion technique was used for the numerical computations. This paper can be considered as an interesting benchmark for future work comparisons in smart FGMs. Moreover, a finite element method has been recently used to deal with the dynamic fully coupled analysis of smart structures where thermal, electrical and mechanical effects take place. Different plate theories were tested as well as more refined electrical field representations. For instance, [34], the authors used a higher order shear deformation theory to describe the elastic field of composite laminates with embedded piezoelectric patches. For the electrical field, a quadratic variation through thickness was employed and the thermal field was not considered; the thermal field was included in a more recent work [35]. [36] used a layerwise theory to calculate the static and dynamic response of composite plates with surface-mounted piezoelectric actuators using a completely coupled thermo-piezoelectric-mechanical model. In this work, the authors showed the importance of the transverse shear forces in modelling smart plate structures.

C. Objectives

Even though many researchers have been working in the analysis of smart structures, until now there is no general methodology that allows us to study these struc-

tures realistically. This means an approach that considers most important features associated with the elastic, electrical, and thermal fields in a smart structure is needed. Each of these fields requires their own suitable representation that depends on the application. In a slender composite beam with actuators and sensors, the elastic field can be modelled using the Euler-Bernoulli beam theory, and the electrical field using a layer wise theory. Moreover, some regions of the beam undergoes electrical and elastic effects at the same time; however, other parts may only contain elastic effect. An efficient mathematical model and associated computational model should account for all significant features of the structural response. Thus, the objectives of the present study were as follows.

- Develop a refined kinematic model and associated finite element model with various capabilities to solve problems that have both 2-D and 3-D fields.
- Use this element to investigate different issues related to smart structures such as
 - Diverse configuration of their components
 - Accurate stress-strain analysis
 - Analysis several physical effects
- Perform a fully coupled thermo-piezo-elastic analysis of smart structures not only for static response but also for dynamic response.
- Analysis of vibration control of structural elements, especially plates, using active strategies.
- Develop accurate models to facilitate the design of controllers while using LQG, LQR, negative feedback velocity and robust control algorithms.

D. Description of the Work

As discussed in the previous paragraphs, the main problem that arises in the modelling of smart materials is accurate representation of their physical effects. Along with the development of the smart structure field, new and more complicated configurations have appeared to satisfy the functional requirements of new and emerging engineering applications. Moreover, in order to accurately describe the physical effects involved in practical applications, we need a mathematical model that accounts for the coupling between various fields. As a result, a large number of coupled equations must be solved and diverse analytical and numerical techniques must be employed. Among them, the finite element method has proved to be a very efficient and systematic computational technique to solve complicated problems with complex geometries and multiphysics because of its relative simplicity and easy computer implementation (see [37, 38]).

In this research, an improved structural theory and associated finite element model that accounts for most important features of a smart structural system are developed. In the first part of this work, we present a new formulation to describe the displacement field which results in an improved version of the third-order shear deformation theory of Reddy [28]. To take account the electrical field, the layerwise formulation is improved and adapted in combination with the elastic field. Finally, the layerwise representation for the thermal field was used; however, for some cases, as indicated in the sequel, an equivalent single-layer representation was used. After these earlier developments, a finite element formulation is presented for a fully coupled thermo-electro-mechanical dynamic system using concepts of continuum mechanics but assuming linear strains and constitutive behavior.

In the second part of this study, we focus on static problems only. The theory

developed in the first part is verified in two parts. Firstly, using composite and functionally graded material (FGM) plates, we were able to test the ability of the element to handle elastic problems. Numerical results showing the displacement and stress fields over the plate are presented. Then using a functionally graded material plate, the thermo-mechanical analysis is performed and the results are compared with other theories currently available. The applicability and potential of the proposed theory is amply demonstrated. Finally, the same analysis is applied for a FGM plate with a piezoelectric layer mounted in its bottom part (smart FGM plate). Here, an improvement of the theory was utilized to obtain good results for the thermo-piezomechanical analysis.

In the third part, a dynamical analysis was carried out. Like in the static analysis part, the verifications were carried out using a FGM plate and a smart FGM plate. Several cases of importance were explored, such as, thermal and electrical shocks. However, the main issue of this part is to show the difference in the response of the structure if coupled and uncoupled analysis are performed.

Finally, a chapter devoted to the vibration control of structures is added to this work. Two main strategies were presented: the negative velocity feedback and the least squares quadratic regulator. The first one is a very simple technique that is based on the proportionality between the sensor and actuator voltage. The second one is based on an optimization principle. Some graphics are presented in order to show the suitability of those control algorithms.

CHAPTER II

GENERAL FORMULATION

A. Multiple Assumed Displacement Fields

In general, any physical field such as elastic, thermal or electrical can be represented as the combination of several representations. We can apply this idea in the case of elastic plates, by writing the displacements as the sum of the equivalent single-layer representation (ESL) and the layerwise representation (LWT), as shown in Fig. 1; it is called the approach of multiple assumed displacement fields. The multiple assumed displacement fields can be expressed as

$$\begin{aligned}
 u(x, y, z, t) &= u^{ESL}(x, y, x, t) + u^{LWT}(x, y, x, t) \\
 v(x, y, z, t) &= v^{ESL}(x, y, x, t) + v^{LWT}(x, y, x, t) \\
 w(x, y, z, t) &= w^{ESL}(x, y, x, t) + w^{LWT}(x, y, x, t)
 \end{aligned} \tag{2.1}$$

where u and v are the displacements in the x and y directions, respectively, and w is the transverse displacement.

The most important ESL theories are the classical plate theory (CLPT), the first order shear deformation theory (FSDT) and the third-order shear deformation theory (TSDT) (see [39]). In CLPT, we assume that the Kirchhoff hypothesis holds: the straight lines perpendicular to the midsurface before deformation remain perpendicular ($\epsilon_{xz} = \epsilon_{yz} = 0$) to the midsurface and straight after deformation. Moreover, the transverse normals do not experience elongation ($\epsilon_{33} = 0$). In the FSDT, the transverse normals do not remain perpendicular to the midsurface after deformation; therefore the shear strains ϵ_{xz} and ϵ_{yz} are different from zero. Finally, in the case of TSDT, we make the same assumptions as FSDT, but the straightness of a transverse

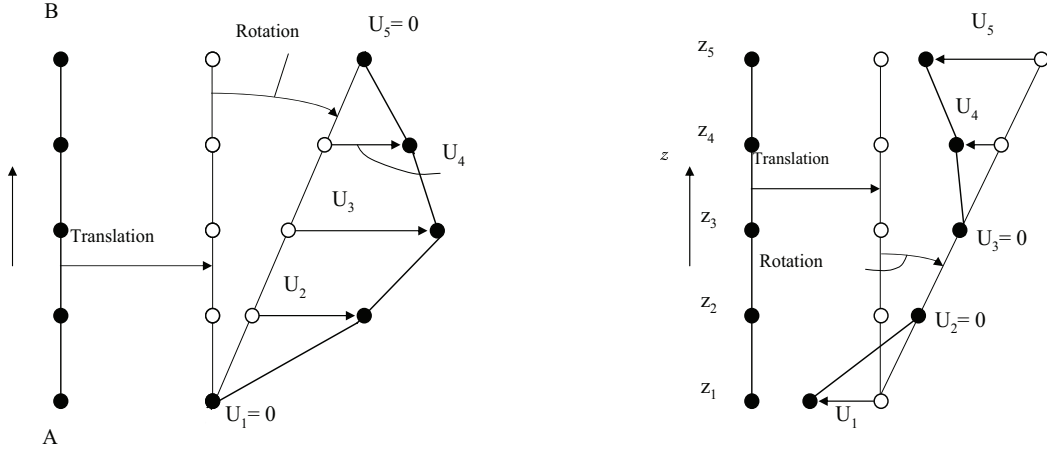


Fig. 1. Multiple assumed displacement mechanism for the case where ESL is FSDT normal after deformation is relaxed. A graphical idea of the kinematics of the deformation of a transverse normal on any edge of the plate is shown in Fig. 2. The three theories can be compactly represented using the following set of equations

$$\begin{aligned}
 u(x, y, z, t) &= u_0 - c_0 z w_{0,x} + (z - c_1 z^3) \varphi_x \\
 v(x, y, z, t) &= v_0 - c_0 z w_{0,y} + (z - c_1 z^3) \varphi_y \\
 w(x, y, z, t) &= w_0(x, y, z, t)
 \end{aligned} \tag{2.2}$$

where c_0 and c_1 are the tracers, and φ_x and φ_y are the rotations. The values of the tracers, φ_x and φ_y for the different theories are

CLPT:

$$c_0 = 1, c_1 = 0, \varphi_x = \varphi_y = 0 \tag{2.3}$$

FSDT:

$$c_0 = 0, c_1 = 0, \tag{2.4}$$

TSdT:

$$c_0 = 1, c_1 = \frac{4}{3h^2} \tag{2.5}$$

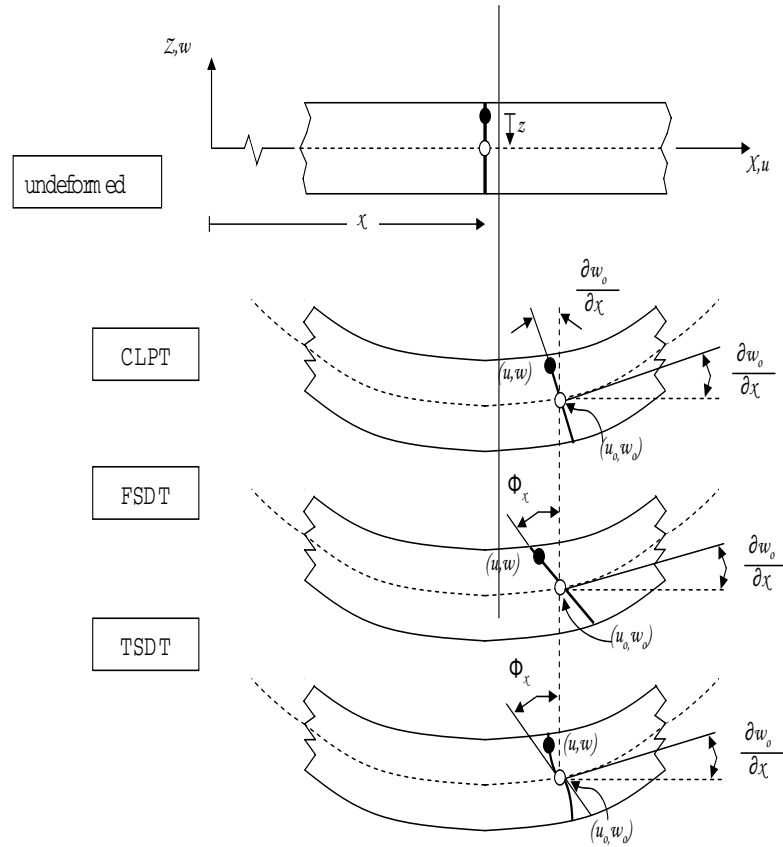


Fig. 2. Deformation of the transverse normal section according to CLPT, FSDT and TSDT

Using matrix representation for Eq. 2.2

$$u_u^{ESL} = N_{u(ESL)}(z)u_{uxy}^{ESL} \quad (2.6)$$

where

$$\begin{aligned} u_u^{ESL} &= \begin{bmatrix} u^{ESL} & v^{ESL} & w^{ESL} \end{bmatrix}^T \\ u_{uxy}^{ESL} &= \begin{bmatrix} u_0 & v_0 & w_0 & w_{0,x} & w_{0,y} & \varphi_x & \varphi_y \end{bmatrix}^T \end{aligned} \quad (2.7)$$

$$N_{u(ESL)}(z) = \begin{bmatrix} 1 & 0 & 0 & -c_0z & 0 & z - c_1z^3 & 0 \\ 0 & 1 & 0 & 0 & -c_0z & 0 & z - c_1z^3 \\ 0 & 0 & 1 & 0 & 0 & 0 & 0 \end{bmatrix} \quad (2.8)$$

the finite element representation of the vector u_{uxy}^{ESL} is

$$u_{uxy}^{e(ESL)} = N_{u(ESL)}^e(x, y)u_{u(ESL)}^e \quad (2.9)$$

where

$$N_{u(ESL)}^e(x, y) = \begin{bmatrix} N_{u(ESL)}^{e(1)}(x, y) & \cdot & \cdot & N_{u(ESL)}^{e(j)}(x, y) & \cdot & \cdot & N_{u(ESL)}^{e(n)}(x, y) \end{bmatrix} \quad (2.10)$$

$$u_{u(ESL)}^e = \begin{bmatrix} u_{u(ESL)}^{e(1)} & \cdot & \cdot & u_{u(ESL)}^{e(j)} & \cdot & \cdot & u_{u(ESL)}^{e(n)} \end{bmatrix} \quad (2.11)$$

and

$$N_{u(ESL)}^{e(j)}(x, y) = \begin{bmatrix} l_{u_0}^j & 0 & 0 & 0 & 0 & 0 & 0 & 0 \\ 0 & l_{v_0}^j & 0 & 0 & 0 & 0 & 0 & 0 \\ 0 & 0 & h_1^j & h_2^j & h_3^j & h_4^j & 0 & 0 \\ 0 & 0 & h_{1,x}^j & h_{2,x}^j & h_{3,x}^j & h_{4,x}^j & 0 & 0 \\ 0 & 0 & h_{1,y}^j & h_{2,y}^j & h_{3,y}^j & h_{4,y}^j & 0 & 0 \\ 0 & 0 & 0 & 0 & 0 & 0 & l_{\varphi_x}^j & 0 \\ 0 & 0 & 0 & 0 & 0 & 0 & 0 & l_{\varphi_y}^j \end{bmatrix} \quad (2.12)$$

where l^j and h^j are the Lagrangian and Hermite interpolation functions, respectively.

$$u_{u(ESL)}^{e(j)} = \left[u_0^j \quad v_0^j \quad w_0^j \quad w_{0,x}^j \quad w_{0,y}^j \quad w_{0,xy}^j \quad \varphi_x^j \quad \varphi_y^j \right]^T \quad (2.13)$$

As we can see above, all the equivalent layer theories are based on assumptions that do not necessarily hold when 3D effects take place in the structure. For this reason, several layerwise theories have been developed as explained in [39]. However for this work, we are going to employ the layerwise theory of Reddy due to its simplicity and versatility. The only disadvantage of this theory is that a large number of degrees of freedom (dofs) are used to describe the elastic effect over the plate.

For the layerwise representation using Reddy's theory (see [10]), the total displacement field can be expressed as

$$\begin{aligned} u^{LWT}(x, y, z, t) &= \sum_{I=1}^{NU} U_I(x, y, t) \Phi_U^I(z) \\ v^{LWT}(x, y, z, t) &= \sum_{I=1}^{NV} V_I(x, y, t) \Phi_V^I(z) \\ w^{LWT}(x, y, z, t) &= \sum_{I=1}^{NW} W_I(x, y, t) \Phi_W^I(z) \end{aligned} \quad (2.14)$$

where (U_I, V_I, W_I) denote the nodal values through the thickness, NU , NV and NW is the number of levels through the thickness or discretization in the z coordinate, and $\Phi_U^I, \Phi_V^I, \Phi_W^I(z)$ are the global interpolation functions over the z coordinate, see Fig. 3 for details. Therefore, using a matrix representation for Eq. 2.14, we have

$$u_u^{LWT} = N_{u(LWT)}(z) u_{uxy}^{LWT} \quad (2.15)$$

where

$$u_u^{LWT} = \left[u^{LWT} \quad v^{LWT} \quad w^{LWT} \right]^T \quad (2.16)$$

$$N_{u(LWT)}(z) = \left[N_{u(LWT)}^1(z) \quad \cdot \quad \cdot \quad N_{u(LWT)}^I(z) \quad \cdot \quad \cdot \quad N_{u(LWT)}^N(z) \right]^T \quad (2.17)$$

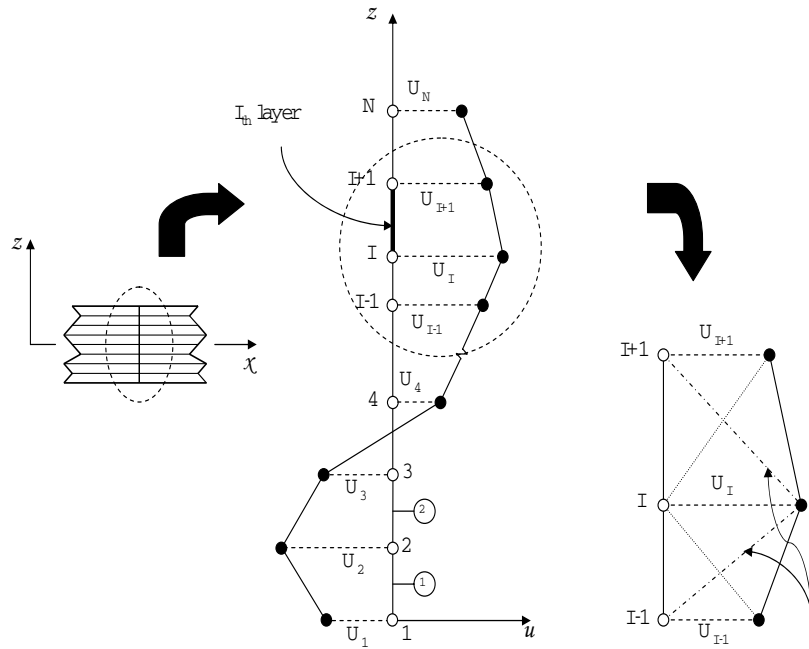


Fig. 3. Displacement representation using the LWT and the linear Lagrangian interpolation function $\Phi^I(z)$

$$u_{uxy}^{LWT} = \left[u_{uxy}^{LWT(1)} \quad \dots \quad u_{uxy}^{LWT(I)} \quad \dots \quad u_{uxy}^{LWT(N)} \right]^T \quad (2.18)$$

where $N = \max\{NU, NV, NW\}$

$$u_{uxy}^{LWT(I)} = \begin{bmatrix} U_I & V_I & W_I \end{bmatrix} ; \quad N_{u(LWT)}(z) = \begin{bmatrix} \Phi_U^I & 0 & 0 \\ 0 & \Phi_V^I & 0 \\ 0 & 0 & \Phi_W^I \end{bmatrix} \quad (2.19)$$

the finite element representation of the vector u_{uxy}^{LWT} is

$$u_{uxy}^{e(LWT)} = N_{u(LWT)}^e(x, y) u_{u(LWT)}^e \quad (2.20)$$

where

$$N_{u(LWT)}^e(x, y) = \text{diag} \left[N_{u(LWT)}^{e(1)}(x, y) \quad \dots \quad N_{u(LWT)}^{e(I)}(x, y) \quad \dots \quad N_{u(LWT)}^{e(N)}(x, y) \right] \quad (2.21)$$

$$u_{u(LWT)}^e(x, y) = \left[u_{u(LWT)}^{e(1)}(x, y) \quad \dots \quad u_{u(LWT)}^{e(I)}(x, y) \quad \dots \quad u_{u(LWT)}^{e(N)}(x, y) \right]^T \quad (2.22)$$

and

$$N_{u(LWT)}^{e(I)}(x, y) = \left[N_{u(LWT)}^{e(I)1}(x, y) \quad \dots \quad N_{u(LWT)}^{e(I)j}(x, y) \quad \dots \quad N_{u(LWT)}^{e(I)n}(x, y) \right] \quad (2.23)$$

$$u_{u(LWT)}^{e(I)} = \left[u_{u(LWT)}^{e(I)1} \quad \dots \quad u_{u(LWT)}^{e(I)j} \quad \dots \quad u_{u(LWT)}^{e(I)n} \right] \quad (2.24)$$

with

$$N_{u(LWT)}^{e(I)j}(x, y) = \begin{bmatrix} l_{U_I}^j & 0 & 0 \\ 0 & l_{V_I}^j & 0 \\ 0 & 0 & l_{W_I}^j \end{bmatrix} ; \quad u_{u(LWT)}^{e(I)j} = \left[U_I^j \quad V_I^j \quad W_I^j \right]^T \quad (2.25)$$

1. Strain Field

In this work, we are going to make two assumptions related to the strain and displacement fields. The first one is that the structure experiences small strain and displacement fields; therefore, material and spatial coordinates can be used indistinctively. The same will apply between the finite Green strain tensor and infinitesimal strain tensor, and between the second Piola-Kirchhoff stress tensor and the Cauchy stress tensor. The other assumption is that the rotations of the transverse normals are small. Based on these assumptions, the strains associated with the displacement field represented by Eq. 2.1 are

$$\begin{aligned}
\varepsilon_{xx} &= u_{,x} = \varepsilon_{xx}^{ESL} + \varepsilon_{xx}^{LWT} \\
\varepsilon_{yy} &= v_{,y} = \varepsilon_{yy}^{ESL} + \varepsilon_{yy}^{LWT} \\
\varepsilon_{zz} &= w_{,z} = \varepsilon_{zz}^{ESL} + \varepsilon_{zz}^{LWT} \\
\gamma_{yz} &= v_{,z} + w_{,y} = \gamma_{yz}^{ESL} + \gamma_{yz}^{LWT} \\
\gamma_{xz} &= u_{,z} + w_{,x} = \gamma_{xz}^{ESL} + \gamma_{xz}^{LWT} \\
\gamma_{xy} &= u_{,y} + v_{,x} = \gamma_{xy}^{ESL} + \gamma_{xy}^{LWT}
\end{aligned} \tag{2.26}$$

where

$$\begin{aligned}
\varepsilon_{xx}^{ESL} &= u_{0,x} - c_0 z w_{0,xx} + (z - c_1 z^3) \varphi_{x,x} \\
\varepsilon_{yy}^{ESL} &= v_{0,y} - c_0 z w_{0,yy} + (z - c_1 z^3) \varphi_{y,y} \\
\varepsilon_{zz}^{ESL} &= 0 \\
\gamma_{yz}^{ESL} &= (1 - c_0) w_{,y} + (1 - 3c_1 z^2) \varphi_y \\
\gamma_{xz}^{ESL} &= (1 - c_0) w_{,x} + (1 - 3c_1 z^2) \varphi_x \\
\gamma_{xy}^{ESL} &= u_{0,y} + v_{0,x} - 2c_0 z w_{0,xy} + (z - c_1 z^3) \varphi_{x,y} + (z - c_1 z^3) \varphi_{y,x}
\end{aligned} \tag{2.27}$$

whose matrix representation is

$$\varepsilon^{ESL} = B_{u(ESL)}(z)\varepsilon_{xy}^{ESL} \quad (2.28)$$

$$\varepsilon^{ESL} = \left[\varepsilon_{xx}^{ESL} \quad \varepsilon_{yy}^{ESL} \quad \varepsilon_{zz}^{ESL} \quad \gamma_{yz}^{ESL} \quad \gamma_{xz}^{ESL} \quad \gamma_{xy}^{ESL} \right]^T \quad (2.29)$$

$$\varepsilon_{xy}^{ESL} = \left[\varepsilon_u^{ESL} \quad \varepsilon_v^{ESL} \quad \varepsilon_w^{ESL} \quad \varepsilon_{\varphi_x}^{ESL} \quad \varepsilon_{\varphi_y}^{ESL} \right] \quad (2.30)$$

$$\varepsilon_u^{ESL} = \begin{bmatrix} u_{0,x} & u_{0,y} \end{bmatrix} \quad \varepsilon_v^{ESL} = \begin{bmatrix} v_{0,x} & v_{0,y} \end{bmatrix} \quad (2.31)$$

$$\varepsilon_w^{ESL} = \begin{bmatrix} w_{0,x} & w_{0,y} & w_{0,xx} & w_{0,yy} & w_{0,xy} \end{bmatrix} \quad (2.32)$$

$$\varepsilon_{\varphi_x}^{ESL} = \begin{bmatrix} \varphi_x & \varphi_{x,x} & \varphi_{x,y} \end{bmatrix} \quad \varepsilon_{\varphi_y}^{ESL} = \begin{bmatrix} \varphi_y & \varphi_{y,x} & \varphi_{y,y} \end{bmatrix} \quad (2.33)$$

$$B_{u(ESL)}(z) = \left[B_{u(ESL)}^{(u)} \quad B_{u(ESL)}^{(v)} \quad B_{u(ESL)}^{(w)} \quad B_{u(ESL)}^{(\varphi_x)} \quad B_{u(ESL)}^{(\varphi_y)} \right] \quad (2.34)$$

$$B_{u(ESL)}^{(u)} = \begin{bmatrix} 1 & 0 \\ 0 & 0 \\ 0 & 0 \\ 0 & 0 \\ 0 & 0 \\ 0 & 0 \\ 0 & 1 \end{bmatrix} \quad B_{u(ESL)}^{(v)} = \begin{bmatrix} 0 & 0 \\ 0 & 1 \\ 0 & 0 \\ 0 & 0 \\ 0 & 0 \\ 0 & 0 \\ 1 & 0 \end{bmatrix} \quad (2.35)$$

$$B_{u(ESL)}^{(w)} = \begin{bmatrix} 0 & 0 & -c_0 z & 0 & 0 \\ 0 & 0 & 0 & -c_0 z & 0 \\ 0 & 0 & 0 & 0 & 0 \\ 0 & 1 - c_0 & 0 & 0 & 0 \\ 1 - c_0 & 0 & 0 & 0 & 0 \\ 0 & 0 & 0 & -2c_0 z & 0 \end{bmatrix} \quad (2.36)$$

$$B_{u(ESL)}^{(\varphi_x)} = \begin{bmatrix} 0 & z - c_1 z^3 & 0 \\ 0 & 0 & 0 \\ 0 & 0 & 0 \\ 0 & 0 & 0 \\ 1 - 3c_1 z^2 & 0 & 0 \\ 0 & 0 & z - c_1 z^3 \end{bmatrix} \quad (2.37)$$

$$B_{u(ESL)}^{(\varphi_y)} = \begin{bmatrix} 0 & 0 & 0 \\ 0 & 0 & z - c_1 z^3 \\ 0 & 0 & 0 \\ 1 - 3c_1 z^2 & 0 & 0 \\ 0 & 0 & 0 \\ 0 & z - c_1 z^3 & 0 \end{bmatrix} \quad (2.38)$$

The finite element representation of ε_{xy}^{ESL}

$$\varepsilon_{xy}^{e(ESL)} = B_{u(ESL)}^e(x, y) u_{u(ESL)}^e \quad (2.39)$$

where

$$B_{u(ESL)}^e(x, y) = \left[B_{u(ESL)}^{e(1)}(x, y) \quad \cdot \quad \cdot \quad B_{u(ESL)}^{e(j)}(x, y) \quad \cdot \quad \cdot \quad B_{u(ESL)}^{e(n)}(x, y) \right] \quad (2.40)$$

$$u_{u(ESL)}^e = \left[u_{u(ESL)}^{e(1)} \quad \cdot \quad \cdot \quad \cdot \quad u_{u(ESL)}^{e(j)} \quad \cdot \quad \cdot \quad \cdot \quad u_{u(ESL)}^{e(n)} \right]^T \quad (2.41)$$

with

$$B_{u(ESL)}^{e(j)}(x, y) = \begin{bmatrix} l_{u_0,x}^j & 0 & 0 & 0 & 0 & 0 & 0 & 0 \\ l_{u_0,y}^j & 0 & 0 & 0 & 0 & 0 & 0 & 0 \\ 0 & l_{v_0,x}^j & 0 & 0 & 0 & 0 & 0 & 0 \\ 0 & l_{v_0,y}^j & 0 & 0 & 0 & 0 & 0 & 0 \\ 0 & 0 & h_{1,x}^j & h_{2,x}^j & h_{3,x}^j & h_{4,x}^j & 0 & 0 \\ 0 & 0 & h_{1,y}^j & h_{2,y}^j & h_{3,y}^j & h_{4,y}^j & 0 & 0 \\ 0 & 0 & h_{1,xx}^j & h_{2,xx}^j & h_{3,xx}^j & h_{4,xx}^j & 0 & 0 \\ 0 & 0 & h_{1,yy}^j & h_{2,yy}^j & h_{3,yy}^j & h_{4,yy}^j & 0 & 0 \\ 0 & 0 & h_{1,xy}^j & h_{2,xy}^j & h_{3,xy}^j & h_{4,xy}^j & 0 & 0 \\ 0 & 0 & 0 & 0 & 0 & 0 & l_{\varphi_x}^j & 0 \\ 0 & 0 & 0 & 0 & 0 & 0 & l_{\varphi_x,x}^j & 0 \\ 0 & 0 & 0 & 0 & 0 & 0 & l_{\varphi_x,y}^j & 0 \\ 0 & 0 & 0 & 0 & 0 & 0 & 0 & l_{\varphi_y}^j \\ 0 & 0 & 0 & 0 & 0 & 0 & 0 & l_{\varphi_y,x}^j \\ 0 & 0 & 0 & 0 & 0 & 0 & 0 & l_{\varphi_y,y}^j \end{bmatrix} \quad (2.42)$$

$$u_{u(ESL)}^{e(j)} = \left[u_0^j \quad v_0^j \quad w_0^j \quad w_{0,x}^j \quad w_{0,y}^j \quad w_{0,xy}^j \quad \varphi_x^j \quad \varphi_y^j \right]^T \quad (2.43)$$

The contribution of the layerwise representation to the strain field is

$$\varepsilon_{xx}^{LWT} = \sum_{I=1}^{NU} U_{I,x} \Phi_U^I(z)$$

$$\begin{aligned}
\varepsilon_{yy}^{LWT} &= \sum_{I=1}^{NV} V_{I,y} \Phi_V^I(z) \\
\varepsilon_{zz}^{LWT} &= \sum_{I=1}^{NW} W_I \Phi_{W,z}^I(z) \\
\gamma_{yz}^{LWT} &= \sum_{I=1}^{NV} V_I \Phi_{V,z}^I(z) + \sum_{I=1}^{NW} W_{I,y} \Phi_W^I(z) \\
\gamma_{xz}^{LWT} &= \sum_{I=1}^{NV} U_I \Phi_{U,z}^I(z) + \sum_{I=1}^{NW} W_{I,x} \Phi_W^I(z) \\
\gamma_{xy}^{LWT} &= \sum_{I=1}^{NU} U_{I,y} \Phi_U^I(z) + \sum_{I=1}^{NV} V_{I,x} \Phi_V^I(z)
\end{aligned} \tag{2.44}$$

whose matrix representation is

$$\varepsilon^{LWT} = B_{u(LWT)}(z) \varepsilon_{xy}^{LWT} \tag{2.45}$$

where

$$\varepsilon^{LWT} = \left[\varepsilon_{xx}^{LWT} \quad \varepsilon_{yy}^{LWT} \quad \varepsilon_{zz}^{LWT} \quad \gamma_{yz}^{LWT} \quad \gamma_{xz}^{LWT} \quad \gamma_{xy}^{LWT} \right]^T \tag{2.46}$$

$$B_{u(LWT)}(z) = \left[B_{u(LWT)}^1(z) \quad \cdot \quad \cdot \quad B_{u(LWT)}^I(z) \quad \cdot \quad \cdot \quad B_{u(LWT)}^N(z) \right] \tag{2.47}$$

$$\varepsilon_{xy}^{LWT} = \left[\varepsilon_{xy}^{LWT(1)} \quad \cdot \quad \cdot \quad \varepsilon_{xy}^{LWT(I)} \quad \cdot \quad \cdot \quad \varepsilon_{xy}^{LWT(N)} \right]^T \tag{2.48}$$

$$B_{u(LWT)}^I(z) = \begin{bmatrix} 0 & \Phi_U^I & 0 & 0 & 0 & 0 & 0 & 0 & 0 \\ 0 & 0 & 0 & 0 & 0 & \Phi_V^I & 0 & 0 & 0 \\ 0 & 0 & 0 & 0 & 0 & 0 & \Phi_{W,z}^I & 0 & 0 \\ 0 & 0 & 0 & \Phi_{V,z}^I & 0 & 0 & 0 & 0 & \Phi_W^I \\ \Phi_{U,z}^I & 0 & 0 & 0 & 0 & 0 & 0 & \Phi_W^I & 0 \\ 0 & 0 & \Phi_U^I & 0 & \Phi_V^I & 0 & 0 & 0 & 0 \end{bmatrix} \tag{2.49}$$

$$\varepsilon_{xy}^{LWT(I)} = \left[U_I \quad U_{I,x} \quad U_{I,y} \quad V_I \quad V_{I,x} \quad V_{I,y} \quad W_I \quad W_{I,x} \quad W_{I,y} \right]^T \tag{2.50}$$

The finite element representation of ε_{xy}^{LWT}

$$\varepsilon_{xy}^{e(LWT)} = B_{u(LWT)}^e(x, y) u_{u(LWT)}^e \quad (2.51)$$

where

$$u_{u(LWT)}^e(x, y) = \text{diag} \left[u_{u(LWT)}^{e(1)}(x, y) \quad \cdot \quad \cdot \quad u_{u(LWT)}^{e(I)}(x, y) \quad \cdot \quad \cdot \quad u_{u(LWT)}^{e(N)}(x, y) \right] \quad (2.52)$$

$$B_{u(LWT)}^e(x, y) = \text{diag} \left[B_{u(LWT)}^{e(1)}(x, y) \quad \cdot \quad \cdot \quad B_{u(LWT)}^{e(I)}(x, y) \quad \cdot \quad \cdot \quad B_{u(LWT)}^{e(N)}(x, y) \right] \quad (2.53)$$

with

$$B_{u(LWT)}^{e(I)}(x, y) = \left[B_{u(LWT)}^{e(I)1}(x, y) \quad \cdot \quad \cdot \quad B_{u(LWT)}^{e(I)j}(x, y) \quad \cdot \quad \cdot \quad B_{u(LWT)}^{e(I)n}(x, y) \right] \quad (2.54)$$

and

$$B_{u(LWT)}^j(x, y) = \begin{bmatrix} B_{u(LWT)}^{j(U_I)} & 0 & 0 \\ 0 & B_{u(LWT)}^{j(V_I)} & 0 \\ 0 & 0 & B_{u(LWT)}^{j(W_I)} \end{bmatrix} \quad (2.55)$$

$$B_{u(LWT)}^{j(\kappa)}(x, y) = \left[l_\kappa \quad l_{\kappa,x} \quad l_{\kappa,y} \right]^T \quad (2.56)$$

$$u_{u(LWT)}^e = \left[u_{u(LWT)}^{e(1)} \quad \cdot \quad \cdot \quad u_{u(LWT)}^{e(j)} \quad \cdot \quad \cdot \quad u_{u(LWT)}^{e(n)} \right]^T \quad (2.57)$$

$$u_{u(LWT)}^{e(j)} = \left[U_I^j \quad V_I^j \quad W_I^j \right]^T \quad (2.58)$$

B. Improved ESL Deformation Theory

As we noticed in the previous section, the multiple assumed displacement field formulation provides the capability of doing a realistic analysis of the mechanical structures since most of the 3D elasticity features are considered. However, by adding

layerwise dofs dramatically increases the total number of dofs. Moreover, combining two representation makes the computer implementation cumbersome. Consequently, it will be interesting to consider a ESL formulation that contains the characteristics of the combined two theories.

In this section, we are going to describe a novel formulation that results from improvement of the ESL theories. First, as we did in the previous sections, let us consider the displacement field represented by the Eq. 2.1. Then, continuing with the process of Multiple Assumed Displacement Field, the thickness of the plate should be divided in several mathematical layers to take into account the layerwise part of the formulation. In this case, we are going to use only one mathematical layer, but the interpolation functions used for the z coordinates are going to be Hermite instead of Lagrangian. As a consequence, each of the two levels that comprises the mathematical layer will have 6 variables, the three displacements (U , V and W) and their derivatives with respect to the z coordinate (U' , V' and W'). Since the layerwise field can model any of the deformation modes that the ESL can, there will be five redundant variables that must be set to zero, otherwise, ill-conditioned matrices will appear in our analysis. Hence,

$$U_1 = U_2 = 0, V_1 = V_2 = 0, W_1 = 0 \quad (2.59)$$

Finally, the set of equations that describe an improved equivalent single-layer field are

$$\begin{aligned} u(x, y, z, t) &= u^{ESL} + h_3(z)U_1' + h_4(z)U_2' \\ v(x, y, z, t) &= v^{ESL} + h_3(z)V_1' + h_4(z)V_2' \\ w(x, y, z, t) &= w^{ESL} + h_2(z)W_2 + h_3(z)W_1' + h_4(z)W_2' \end{aligned} \quad (2.60)$$

where the matrix representation for the improvement is

$$u_u^{IESL} = N_{u(IESL)}(z)u_{uxy}^{IESL} \quad (2.61)$$

where

$$N_{u(IESL)}(z) = \begin{bmatrix} h_3(z) & h_4(z) & 0 & 0 & 0 & 0 & 0 \\ 0 & 0 & h_3(z) & h_4(z) & 0 & 0 & 0 \\ 0 & 0 & 0 & 0 & h_2(z) & h_3(z) & h_4(z) \end{bmatrix} \quad (2.62)$$

with h_i as Hermite interpolation functions

$$u_{uxy}^{IESL} = \left[U'_1 \quad U'_2 \quad V'_1 \quad V'_2 \quad W_2 \quad W'_1 \quad W'_2 \right]^T \quad (2.63)$$

the finite element representation of the vector u_{uxy}^{IESL} is

$$u_{uxy}^{e(IESL)} = N_{u(IESL)}^e(x, y)u_u^e(IESL) \quad (2.64)$$

where

$$N_{u(IESL)}^e(x, y) = \left[N_{u(IESL)}^{e(1)}(x, y) \quad \dots \quad N_{u(IESL)}^{e(j)}(x, y) \quad \dots \quad N_{u(IESL)}^{e(n)}(x, y) \right] \quad (2.65)$$

$$u_u^e(IESL) = \left[u_{u(IESL)}^{e(1)} \quad \dots \quad u_{u(IESL)}^{e(j)} \quad \dots \quad u_{u(IESL)}^{e(n)} \right] \quad (2.66)$$

with

$$N_{u(IESL)}^{e(j)}(x, y) = \begin{bmatrix} l_{U'_1}^j & 0 & 0 & 0 & 0 & 0 & 0 \\ 0 & l_{U'_2}^j & 0 & 0 & 0 & 0 & 0 \\ 0 & 0 & l_{V'_1}^j & 0 & 0 & 0 & 0 \\ 0 & 0 & 0 & l_{V'_2}^j & 0 & 0 & 0 \\ 0 & 0 & 0 & 0 & l_{W_2}^j & 0 & 0 \\ 0 & 0 & 0 & 0 & 0 & l_{W'_1}^j & 0 \\ 0 & 0 & 0 & 0 & 0 & 0 & l_{W'_2}^j \end{bmatrix} \quad (2.67)$$

and l^j is a Lagrange interpolation function

$$u_{u(IESL)}^e = \left[U_1'^j \quad U_2'^j \quad V_1'^j \quad V_2'^j \quad W_2'^j \quad W_1'^j \quad W_2'^j \right]^T \quad (2.68)$$

1. Strain Field

The strains associated with the displacement field represented by Eq. 2.60 are

$$\begin{aligned} \varepsilon_{xx} &= \varepsilon_{xx}^{ESL} + h_3(z)U_{1,x}' + h_4(z)U_{2,x}' \\ \varepsilon_{yy} &= \varepsilon_{yy}^{ESL} + h_3(z)V_{1,y}' + h_4(z)V_{2,y}' \\ \varepsilon_{zz} &= \varepsilon_{zz}^{ESL} + h_{2,z}(z)W_2 + h_{3,z}(z)W_1' + h_{4,z}(z)W_2' \\ \gamma_{yz} &= \gamma_{yz}^{ESL} + h_2(z)W_{2,y} + h_3(z)W_{1,y}' + h_4(z)W_{2,y}' + h_{3,z}(z)V_1' + h_{4,z}(z)V_2' \\ \gamma_{xz} &= \gamma_{xz}^{ESL} + h_2(z)W_{2,x} + h_3(z)W_{1,x}' + h_4(z)W_{2,x}' + h_{3,z}(z)U_1' + h_{4,z}(z)U_2' \\ \gamma_{xy} &= \gamma_{xy}^{ESL} + h_3(z)V_{1,x}' + h_4(z)V_{2,x}' + h_3(z)U_{1,y}' + h_4(z)U_{2,y}' \end{aligned} \quad (2.69)$$

where the matrix representation for the improvement is

$$\varepsilon^{IESL} = B_{u(IESL)}(z)\varepsilon_{u_{xy}}^{IESL} \quad (2.70)$$

$$\varepsilon^{IESL} = \left[\varepsilon_{xx}^{IESL} \quad \varepsilon_{yy}^{IESL} \quad \varepsilon_{zz}^{IESL} \quad \gamma_{yz}^{IESL} \quad \gamma_{xz}^{IESL} \quad \gamma_{xy}^{IESL} \right]^T \quad (2.71)$$

$$B_{u(IESL)}(z) = \left[B_{u(IESL)}^U(z) \quad B_{u(IESL)}^V(z) \quad B_{u(IESL)}^W(z) \right] \quad (2.72)$$

$$B_{u(IESL)}^U(z) = \begin{bmatrix} 0 & h_3 & 0 & 0 & h_4 & 0 \\ 0 & 0 & 0 & 0 & 0 & 0 \\ 0 & 0 & 0 & 0 & 0 & 0 \\ 0 & 0 & 0 & 0 & 0 & 0 \\ h_{3,z} & 0 & 0 & h_{4,z} & 0 & 0 \\ 0 & 0 & h_3 & 0 & 0 & h_4 \end{bmatrix} \quad (2.73)$$

$$B_{u(IESL)}^V(z) = \begin{bmatrix} 0 & 0 & 0 & 0 & 0 & 0 \\ 0 & 0 & h_3 & 0 & 0 & h_4 \\ 0 & 0 & 0 & 0 & 0 & 0 \\ h_{3,z} & 0 & 0 & h_{4,z} & 0 & 0 \\ 0 & 0 & 0 & 0 & 0 & 0 \\ 0 & h_3 & 0 & 0 & h_4 & 0 \end{bmatrix} \quad (2.74)$$

$$B_{u(IESL)}^W(z) = \begin{bmatrix} 0 & 0 & 0 & 0 & 0 & 0 & 0 & 0 & 0 \\ 0 & 0 & 0 & 0 & 0 & 0 & 0 & 0 & 0 \\ h_{2,z} & 0 & 0 & h_{3,z} & 0 & 0 & h_{4,z} & 0 & 0 \\ 0 & 0 & h_2 & 0 & 0 & h_3 & 0 & 0 & h_4 \\ 0 & h_2 & 0 & 0 & h_3 & 0 & 0 & h_4 & 0 \\ 0 & 0 & 0 & 0 & 0 & 0 & 0 & 0 & 0 \end{bmatrix} \quad (2.75)$$

$$\varepsilon_{uxy}^{IESL} = \left[\varepsilon_{uxy}^{U(IESL)} \quad \varepsilon_{uxy}^{V(IESL)} \quad \varepsilon_{uxy}^{W(IESL)} \right]^T \quad (2.76)$$

$$\varepsilon_{uxy}^{U(IESL)} = \left[U'_1 \quad U'_{1,x} \quad U'_{1,y} \quad U'_2 \quad U'_{2,x} \quad U'_{2,y} \right]^T \quad (2.77)$$

$$\varepsilon_{uxy}^{V(IESL)} = \left[V'_1 \quad V'_{1,x} \quad V'_{1,y} \quad V'_2 \quad V'_{2,x} \quad V'_{2,y} \right]^T \quad (2.78)$$

$$\varepsilon_{uxy}^{W(IESL)} = \left[W_2 \quad W_{2,x} \quad W_{2,y} \quad W'_1 \quad W'_{1,x} \quad W'_{1,y} \quad W'_2 \quad W'_{2,x} \quad W'_{2,y} \right]^T \quad (2.79)$$

the finite element representation of the vector ε_{uxy}^{IESL} is

$$\varepsilon_{uxy}^{e(IESL)} = B_{u(IESL)}^e(x, y) u_{u(IESL)}^e \quad (2.80)$$

$$B_{u(IESL)}^j(x, y) = \text{diag} \begin{pmatrix} B_{u(IESL)}^{j(U'_1)} \\ B_{u(IESL)}^{j(U'_2)} \\ B_{u(IESL)}^{j(V'_1)} \\ B_{u(IESL)}^{j(V'_2)} \\ B_{u(IESL)}^{j(W_2)} \\ B_{u(IESL)}^{j(W'_1)} \\ B_{u(IESL)}^{j(W'_2)} \end{pmatrix} \quad (2.81)$$

$$B_{u(IESL)}^{j(\kappa)}(x, y) = \begin{bmatrix} l_\kappa & l_{\kappa,x} & l_{\kappa,y} \end{bmatrix}^T \quad (2.82)$$

$$u_{u(IESL)}^e = \begin{bmatrix} U_1^j & U_2^j & V_1^j & V_2^j & W_2^j & W_1^j & W_2^j \end{bmatrix}^T \quad (2.83)$$

C. Electrical Field

In this section, a brief description of the electrical field for piezoelectric materials will be given according to Tiersten [40]. The electromagnetic field can be described using Maxwell equations

$$\nabla \times H = \frac{1}{c} \frac{\partial D}{\partial t} + \frac{4\pi}{c} J \quad (2.84)$$

$$\nabla \times E = -\frac{1}{c} \frac{\partial B}{\partial t} \quad (2.85)$$

where H is the magnetic field intensity, D is the electric displacement vector, E is the electric field intensity, and B is the magnetic flux vector. These vector fields are related by the following equations:

$$D = E + 4\pi P \quad (2.86)$$

$$B = H + 4\pi M \quad (2.87)$$

where P and M are the polarization and magnetization vector, respectively. The auxiliary equations of Eq. 2.86 and 2.87

$$\nabla \cdot B = 0 \quad (2.88)$$

$$\nabla \cdot D = 4\pi \varrho_e \quad (2.89)$$

in Eq. 2.89, ϱ_e makes that the equation of the conservation of electric charge

$$\frac{\partial \varrho_e}{\partial t} + \nabla \cdot J = 0 \quad (2.90)$$

satisfy; Eq. 2.85 can be reformulated in terms of the vector and scalar potential A and φ

$$\begin{aligned} B &= \nabla \times A \\ \nabla \times \left(E + \frac{1}{c} \dot{A} \right) &= 0 \\ E + \frac{1}{c} \dot{A} &= -\nabla \varphi \end{aligned} \quad (2.91)$$

In the case of piezoelectric, we will consider polarizable (but not magnetizable) dielectrics only. As a consequence, we may set

$$\varrho_e = 0 \quad ; \quad J = M = 0 \quad (2.92)$$

Then Eqs. 2.17 becomes

$$\begin{aligned} H &= B \\ \nabla \times H &= \frac{1}{c} \frac{\partial D}{\partial t} \\ H &= \nabla \times A \\ E &= -\nabla \varphi - \frac{1}{c} \dot{A} \\ \nabla \cdot D &= 0 \end{aligned} \quad (2.94)$$

the assumption made for piezoelectric materials is

$$\left| \frac{1}{c} \dot{A}_i \right| \ll |\varphi_i| \quad (2.95)$$

and if we polarize the material in just one direction and with constant value, we obtain

$$E = -\nabla\phi \Rightarrow \nabla \cdot \nabla\phi = 0 \quad (2.96)$$

This assumption is valid when the electromagnetic and the elastic waves are uncoupled.

In smart materials the piezoelectric configurations are very diverse; therefore geometrical flexibility of the discretization becomes an important issue if a numerical analysis is to be carried out. For this reason, the electrical field is going to be approximated using a layerwise representation as it was proposed in reference [12]

$$u_\phi(x, y, z, t) = \phi^{LWT}(x, y, z, t) = \sum_{I=1}^N \Phi^I(z) \phi_I(x, y, t) \quad (2.97)$$

whose matrix representation

$$u_\phi^{LWT} = N_{\phi(LWT)}(z) u_{\phi(xy)}^{LWT} \quad (2.98)$$

where

$$N_{\phi(LWT)}(z) = \begin{bmatrix} N_{\phi(LWT)}^1(z) & \cdot & \cdot & N_{\phi(LWT)}^I(z) & \cdot & \cdot & N_{\phi(LWT)}^N(z) \end{bmatrix} \quad (2.99)$$

$$u_{\phi(xy)}^{LWT} = \begin{bmatrix} u_{\phi(xy)}^{(LWT)1} & \cdot & \cdot & u_{\phi(xy)}^{(LWT)I} & \cdot & \cdot & u_{\phi(xy)}^{(LWT)N} \end{bmatrix}^T \quad (2.100)$$

$$N_{\phi(LWT)}^I(z) = \begin{bmatrix} \Phi^I \end{bmatrix} \quad ; \quad u_{\phi(xy)}^{(LWT)I} = \begin{bmatrix} \phi_I \end{bmatrix} \quad (2.101)$$

Then, the finite element representation of $u_{\phi(xy)}^{LWT}$

$$u_{\phi(xy)}^{e(LWT)} = N_{\phi(LWT)}^e(x, y) u_{\phi(LWT)}^e \quad (2.102)$$

where

$$N_{\phi(LWT)}^e(x, y) = \text{diag} \left[N_{\phi(LWT)}^{e(1)}(x, y) \quad \dots \quad N_{\phi(LWT)}^{e(2)}(x, y) \quad \dots \quad N_{\phi(LWT)}^{e(N)}(x, y) \right] \quad (2.103)$$

$$u_{\phi(xy)}^e(x, y) = \left[u_{\phi(xy)}^{e(1)}(x, y) \quad \dots \quad u_{\phi(xy)}^{e(2)}(x, y) \quad \dots \quad u_{\phi(xy)}^{e(N)}(x, y) \right]^T \quad (2.104)$$

$$N_{\phi(LWT)}^{e(I)}(x, y) = \left[N_{\phi(LWT)}^{e(I)1} \quad \dots \quad N_{\phi(LWT)}^{e(I)j} \quad \dots \quad N_{\phi(LWT)}^{e(I)n} \right] \quad (2.105)$$

$$u_{\phi(LWT)}^{e(I)} = \left[u_{\phi(LWT)}^{e(I)1} \quad \dots \quad u_{\phi(LWT)}^{e(I)j} \quad \dots \quad u_{\phi(LWT)}^{e(I)n} \right]^T \quad (2.106)$$

$$u_{\phi(LWT)}^{e(I)j} = \left[\phi_I^j \right]; N_{\phi(LWT)}^{e(I)j} = \left[l_{\phi_I}^j \right] \quad (2.107)$$

Similarly, the electrical field intensity

$$E = \begin{bmatrix} E_x \\ E_y \\ E_z \end{bmatrix} = - \begin{bmatrix} \phi_{,x} \\ \phi_{,y} \\ \phi_{,z} \end{bmatrix} \quad (2.108)$$

can be approached

$$E_x = - \sum_{I=1}^{N\phi} \phi_{I,x} \Phi^I(z) \quad E_y = - \sum_{I=1}^{N\phi} \phi_{I,y} \Phi^I(z) \quad E_z = - \sum_{I=1}^{N\phi} \phi_{I,z} \Phi^I(z) \quad (2.109)$$

$$E^{LWT} = B_{\phi(LWT)}(z) E_{\phi(xy)}^{LWT} \quad (2.110)$$

$$B_{\phi(LWT)}(z) = \left[B_{\phi(LWT)}^1(z) \quad \dots \quad B_{\phi(LWT)}^I(z) \quad \dots \quad B_{\phi(LWT)}^N(z) \right] \quad (2.111)$$

$$E_{\phi(xy)}^{LWT} = \left[E_{\phi(xy)}^{(LWT)1} \quad \dots \quad E_{\phi(xy)}^{(LWT)I} \quad \dots \quad E_{\phi(xy)}^{(LWT)N} \right]^T \quad (2.112)$$

$$B_{\phi(LWT)}^I(z) = \begin{bmatrix} 0 & \Phi^I & 0 \\ 0 & 0 & \Phi^I \\ \Phi_{,z}^I & 0 & 0 \end{bmatrix} ; \quad E_{\phi(xy)}^{(LWT)I} = \begin{bmatrix} \phi_I & \phi_{I,x} & \phi_{I,y} \end{bmatrix}^T \quad (2.113)$$

Then, the finite element representation of $E_{\phi(xy)}^{e(LWT)}$

$$E_{\phi(xy)}^{e(LWT)} = B_{\phi(LWT)}^e(x, y) E_{\phi(LWT)}^e \quad (2.114)$$

where

$$B_{\phi(LWT)}^e(x, y) = \begin{bmatrix} B_{\phi(LWT)}^{e(1)}(x, y) & \cdot & \cdot & B_{\phi(LWT)}^{e(I)}(x, y) & \cdot & \cdot & B_{\phi(LWT)}^{e(N)}(x, y) \end{bmatrix} \quad (2.115)$$

$$E_{\phi(LWT)}^e(x, y) = \begin{bmatrix} E_{\phi(LWT)}^{e(1)}(x, y) & \cdot & \cdot & E_{\phi(LWT)}^{e(I)}(x, y) & \cdot & \cdot & E_{\phi(LWT)}^{e(N)}(x, y) \end{bmatrix} \quad (2.116)$$

with

$$B_{\phi(xy)}^{e(I)}(x, y) = \begin{bmatrix} B_{\phi(LWT)}^{e(I)1} & \cdot & \cdot & B_{\phi(LWT)}^{e(I)j} & \cdot & \cdot & B_{\phi(LWT)}^{e(I)n} \end{bmatrix} \quad (2.117)$$

$$E_{\phi(LWT)}^{e(I)} = \begin{bmatrix} E_{\phi(LWT)}^{e(I)1} & \cdot & \cdot & E_{\phi(LWT)}^{e(I)j} & \cdot & \cdot & E_{\phi(LWT)}^{e(I)n} \end{bmatrix}^T \quad (2.118)$$

$$B_{\phi(LWT)}^{e(I)j} = \begin{bmatrix} l_{\phi_I}^j & l_{\phi_I,x}^j & l_{\phi_I,y}^j \end{bmatrix}^T ; \quad E_{\phi(LWT)}^{e(I)j} = \begin{bmatrix} \phi_I^j \end{bmatrix} \quad (2.119)$$

D. Thermal Field

The thermal analysis is an inherently three dimensional problem. Unlike the elastic and electrical fields, when thermal effects are present in a structure, simplifications are only possible for a very specific cases such as for imposed sinusoidal thermal fields [33], or when the heat conductivity coefficient in the z direction is constant [34]. These simplifications allow us to tailor the problem using a kind of equivalent single layer theory for the thermal field. In general, a numerical analysis

of the this field demands a strategy with fully 3-D capabilities. Hence, a layerwise representation is proposed in this work and it can be expressed as

$$T = u_\theta = \sum_{I=1}^N \Phi^I(z) T_I \quad (2.120)$$

whose matrix representation

$$u_\theta^{LWT} = N_{\theta(LWT)}(z) u_{\theta(xy)}^{LWT} \quad (2.121)$$

where

$$N_{\theta(LWT)}(z) = \begin{bmatrix} N_{\theta(LWT)}^1(z) & \cdot & \cdot & N_{\theta(LWT)}^I(z) & \cdot & \cdot & N_{\theta(LWT)}^I(z) & \cdot & \cdot & N_{\theta(LWT)}^I(z) \end{bmatrix} \quad (2.122)$$

$$u_{\theta(xy)}^{LWT} = \begin{bmatrix} u_{\theta(xy)}^{(LWT)1} & \cdot & \cdot & u_{\theta(xy)}^{(LWT)I} & \cdot & \cdot & u_{\theta(xy)}^{(LWT)N} \end{bmatrix}^T \quad (2.123)$$

and

$$N_{\theta(LWT)}^I(z) = \begin{bmatrix} \Phi^I(z) \end{bmatrix} ; \quad u_{\theta(xy)}^{(LWT)I} = \begin{bmatrix} T_I \end{bmatrix} \quad (2.124)$$

The finite element representation of $u_{\theta(xy)}^{LWT}$

$$u_{\theta(xy)}^{e(LWT)} = N_{\theta(LWT)}^e(x, y) u_{\theta(LWT)}^e \quad (2.125)$$

where

$$N_{\theta(LWT)}^e(x, y) = \text{diag} \begin{bmatrix} N_{\theta(LWT)}^{e(1)}(x, y) & \cdot & \cdot & N_{\theta(LWT)}^{e(I)}(x, y) & \cdot & \cdot & N_{\theta(LWT)}^{e(N)}(x, y) \end{bmatrix} \quad (2.126)$$

$$u_{\theta(LWT)}^e(x, y) = \begin{bmatrix} u_{\theta(LWT)}^{e(1)}(x, y) & \cdot & \cdot & u_{\theta(LWT)}^{e(I)}(x, y) & \cdot & \cdot & u_{\theta(LWT)}^{e(N)}(x, y) \end{bmatrix}^T \quad (2.127)$$

with

$$N_{\theta(LWT)}^{e(I)}(x, y) = \begin{bmatrix} N_{\theta(LWT)}^{e(I)1}(x, y) & \cdot & \cdot & N_{\theta(LWT)}^{e(I)j}(x, y) & \cdot & \cdot & N_{\theta(LWT)}^{e(I)n}(x, y) \end{bmatrix} \quad (2.128)$$

$$u_{\theta(LWT)}^{e(I)}(x, y) = \left[u_{\theta(LWT)}^{e(I)1}(x, y) \quad \cdot \quad \cdot \quad u_{\theta(LWT)}^{e(I)j}(x, y) \quad \cdot \quad \cdot \quad u_{\theta(LWT)}^{e(I)n}(x, y) \right] \quad (2.129)$$

and

$$N_{\theta(LWT)}^{e(I)j}(x, y) = \left[l_{T_I}^j \right] \quad ; \quad u_{\theta(LWT)}^{e(I)j}(x, y) = \left[T_I \right] \quad (2.130)$$

The derivatives of the temperature with respect to its Cartesian coordinates

$$T_{,x} = \sum_{I=1}^N \Phi^I(z) T_{I,x} \quad T_{,y} = \sum_{I=1}^N \Phi^I(z) T_{I,y} \quad T_{,z} = \sum_{I=1}^N \Phi_{,z}^I(z) T_I \quad (2.131)$$

whose matrix representation is

$$\Theta^{LWT} = B_{\theta(LWT)}(z) \Theta_{\theta(xy)}^{LWT} \quad (2.132)$$

and

$$B_{\theta(LWT)}(z) = \left[B_{\theta(LWT)}^1(z) \quad \cdot \quad \cdot \quad B_{\theta(LWT)}^I(z) \quad \cdot \quad \cdot \quad B_{\theta(LWT)}^N(z) \right] \quad (2.133)$$

$$\Theta_{\theta(xy)}^{LWT} = \left[\Theta_{\theta(xy)}^{(LWT)1} \quad \cdot \quad \cdot \quad \Theta_{\theta(xy)}^{(LWT)I} \quad \cdot \quad \cdot \quad \Theta_{\theta(xy)}^{(LWT)N} \right]^T \quad (2.134)$$

with

$$B_{\theta(LWT)}^I(x, y) = \begin{bmatrix} \Phi^I(z) & 0 & 0 \\ 0 & \Phi^I(z) & 0 \\ 0 & 0 & \Phi_{,z}^I(z) \end{bmatrix} \quad ; \quad \Theta_{\theta(xy)}^{LWT} = \left[T_{,x}^I \quad T_{,y}^I \quad T^I \right]^T \quad (2.135)$$

The finite element representation of $\Theta_{\theta(xy)}^{LWT}$

$$\Theta_{\theta(xy)}^{e(LWT)} = B_{\theta(LWT)}^e \Theta_{\theta(LWT)}^e \quad (2.136)$$

where

$$B_{\theta(LWT)}^e = \text{diag} \left[B_{\theta(LWT)}^{e(1)} \quad \cdot \quad \cdot \quad B_{\theta(LWT)}^{e(I)} \quad \cdot \quad \cdot \quad B_{\theta(LWT)}^{e(N)} \right] \quad (2.137)$$

$$\Theta_{\theta(LWT)}^e = \text{diag} \left[\Theta_{\theta(LWT)}^{e(1)} \quad \cdot \quad \cdot \quad \Theta_{\theta(LWT)}^{e(I)} \quad \cdot \quad \cdot \quad \Theta_{\theta(LWT)}^{e(N)} \right] \quad (2.138)$$

with

$$B_{\theta(LWT)}^{e(I)} = \begin{bmatrix} B_{\theta(LWT)}^{e(I)1} & \cdot & \cdot & B_{\theta(LWT)}^{e(I)j} & \cdot & \cdot & B_{\theta(LWT)}^{e(I)j} \end{bmatrix} \quad (2.139)$$

$$\Theta_{\theta(LWT)}^{e(I)} = \begin{bmatrix} \Theta_{\theta(LWT)}^{e(I)1} & \cdot & \cdot & \Theta_{\theta(LWT)}^{e(I)j} & \cdot & \cdot & \Theta_{\theta(LWT)}^{e(I)n} \end{bmatrix} \quad (2.140)$$

and

$$B_{\theta(LWT)}^{e(I)j} = \begin{bmatrix} l_{,x}^j & l_{,y}^j & l^j \end{bmatrix}^T ; \quad \Theta_{\phi(LWT)}^{e(I)j} = \begin{bmatrix} T_I^j \end{bmatrix} \quad (2.141)$$

As we mentioned before, the thermal field can be simplified under certain conditions.

For instance, in [33] we can see a plate with the following boundary conditions

$$\begin{aligned} -T_{,z} + h_1 T &= h_1 T^- \quad ; \quad T^- = T(x, y, 0) \\ T_{,z} + h_2 T &= h_2 T^+ \quad ; \quad T^+ = T(x, y, h) \\ T(0, y, z) &= 0 \quad ; \quad T(x, 0, z) = 0 \\ T(a, y, z) &= 0 \quad ; \quad T(x, b, z) = 0 \end{aligned} \quad (2.142)$$

where

$$T^{\pm} = \hat{T}^{\pm} \sin\left(\frac{\pi}{a}x\right) \sin\left(\frac{\pi}{b}y\right) \quad (2.143)$$

For a composite or FGM plate, we can divide its thickness into several layers in such a way that For a layer "k", the heat conduction equation

$$\kappa_{xx}^{(k)} T_{,xx}^{(k)} + \kappa_{yy}^{(k)} T_{,yy}^{(k)} + \kappa_{zz}^{(k)} T_{,zz}^{(k)} = 0 \quad (2.144)$$

must hold. For the boundary conditions specified above, $T^{(k)}$ can be assumed as

$$T^{\pm} = \hat{T}^{\pm} \sin\left(\frac{\pi}{a}x\right) \sin\left(\frac{\pi}{b}y\right) \quad (2.145)$$

Since the temperature and heat flux functions must be continuous in the interlaminar surface between the layer k and $k + 1$, we have the following expressions

$$\begin{aligned} T^{(k)}(z_{k+1}) &= T^{(k+1)}(z_{k+1}) & \hat{T}^{(k)}(z_{k+1}) &= \hat{T}^{(k+1)}(z_{k+1}) \\ \kappa_{zz}^{(k)} T_{,z}^{(k)}(z_{k+1}) &= \kappa_{zz}^{(k+1)} T_{,z}^{(k+1)}(z_{k+1}) & \kappa_{zz}^{(k)} \hat{T}_{,z}^{(k)}(z_{k+1}) &= \kappa_{zz}^{(k)} \hat{T}_{,z}^{(k+1)}(z_{k+1}) \end{aligned} \quad (2.146)$$

replacing Eq. 2.145 into Eq. 2.144

$$\hat{T}_{,zz}^{(k)} - \frac{\kappa_{xx}^{(k)} \left(\frac{\pi}{a}\right)^2 + \kappa_{yy}^{(k)} \left(\frac{\pi}{b}\right)^2}{\kappa_{zz}^{(k)}} \hat{T}^k = 0 \quad (2.147)$$

if we make

$$\mu_k^2 = \frac{\kappa_{xx}^{(k)} \left(\frac{\pi}{a}\right)^2 + \kappa_{yy}^{(k)} \left(\frac{\pi}{b}\right)^2}{\kappa_{zz}^{(k)}} \quad (2.148)$$

Then

$$\hat{T}_{,zz}^{(k)} - \mu_k^2 \hat{T}^{(k)} = 0 \quad (2.149)$$

Assuming that the solution has the following form

$$\hat{T}^{(k)} = Ae^{\lambda z} \quad (2.150)$$

$$\lambda^2 - \mu^2 = 0; \quad (2.151)$$

and then $\lambda = \pm\mu$, which means that the complete solution form of the equation is

$$\hat{T}^k = A^{(k)} e^{\mu_k z} + B^{(k)} e^{-\mu_k z} \quad (2.152)$$

Therefore

$$\hat{T}^k(z) = \frac{T_{k+1} \sinh[\mu_k(z - z_k)] - T_k \sinh[\mu_k(z - z_{k+1})]}{\sinh(\mu_k h_k)} \quad (2.153)$$

Using the principle of energy conservation through the layer interfaces (Eq. 2.146), we have

$$-T_{k+2} + \left[\frac{\beta^k}{\beta^{k+1}} \cosh(\mu_k h_k) + \cosh(\mu_{k+1} h_{k+1}) \right] T_{k+1} - \frac{\beta^k}{\beta^{k+1}} T_k = 0 \quad (2.154)$$

where

$$\beta^k = \frac{\kappa_{zz}^{(k)} \mu_k}{\sinh(\mu_k h_k)} \quad (2.155)$$

Using Eq. 2.154 for the bottom-most and top-most surfaces of the plate

$$-\frac{\mu_1}{\hat{h}_1 \sinh(\mu_1 h_1)} T_2 + \left[1 - \frac{\mu_1 \coth(\mu_1 h_1)}{\hat{h}_1} \right] T_1 = \hat{T}^- \quad (2.156)$$

$$\left[1 + \frac{\mu_n \coth(\mu_n h_n)}{\hat{h}_2} \right] T_{n+1} - \frac{\mu_n}{\hat{h}_2 \sinh(\mu_n h_n)} T_n = \hat{T}^+ \quad (2.157)$$

Using expressions 2.154, 2.156 and Eq. 2.157, we obtain a system of equations that after been solved can give us the temperature thickness distribution as a function of the top and bottom temperature; therefore the thermal analysis can be performed using an equivalent single layer representation and the temperature can be represented as

$$T(x, y, z) = u_{\theta}^{ESL} = h(z)\hat{T}^- + g(z)\hat{T}^+ \quad (2.158)$$

whose matrix representation is

$$u_{\theta}^{ESL} = N_{\theta(ESL)}(z)u_{\theta(xy)}^{ESL} \quad (2.159)$$

where

$$N_{\theta(LWT)}(z) = \begin{bmatrix} h(z) & g(z) \end{bmatrix}; u_{\theta(xy)}^{ESL} = \begin{bmatrix} \hat{T}^- & \hat{T}^+ \end{bmatrix}^T \quad (2.160)$$

The finite element representation of $u_{\theta(xy)}^{ESL}$

$$u_{\theta(xy)}^{e(ESL)} = N_{\theta(ESL)}^e u_{\theta(ESL)}^e; \quad (2.161)$$

with

$$N_{\theta(ESL)}^e = \left[N_{\theta(ESL)}^{e(1)} \quad \cdot \quad \cdot \quad N_{\theta(ESL)}^{e(j)} \quad \cdot \quad \cdot \quad N_{\theta(ESL)}^{e(n)} \right] \quad (2.162)$$

$$u_{\theta(ESL)}^e = \left[u_{\theta(ESL)}^{e(1)} \quad \cdot \quad \cdot \quad u_{\theta(ESL)}^{e(j)} \quad \cdot \quad \cdot \quad u_{\theta(ESL)}^{e(n)} \right] \quad (2.163)$$

$$N_{\theta(ESL)}^{e(j)} = \begin{bmatrix} l_{\hat{T}^-}^j & 0 \\ 0 & l_{\hat{T}^+}^j \end{bmatrix}; u_{\theta(ESL)}^{e(j)} = \left[\hat{T}^{-(j)} \quad \hat{T}^{+(j)} \right]^T \quad (2.164)$$

The derivative of the temperature with respect to its Cartesian coordinates is

$$\Theta^{ESL} = \left[T_{,x} \quad T_{,y} \quad T_{,z} \right] \quad (2.165)$$

whose matrix representation is

$$\Theta^{ESL} = B_{\theta(ESL)}(z)\Theta_{\theta(xy)}^{ESL} \quad (2.166)$$

where

$$B_{\theta(ESL)}(z) = \begin{bmatrix} 0 & g(z) & 0 & 0 & h(z) & 0 \\ 0 & 0 & g(z) & 0 & 0 & h(z) \\ g_{,z}(z) & 0 & 0 & h_{,z}(z) & 0 & 0 \end{bmatrix} \quad (2.167)$$

$$\Theta_{\theta(xy)}^{ESL} = \left[\hat{T}^- \quad \hat{T}_{,x}^- \quad \hat{T}_{,y}^- \quad \hat{T}^+ \quad \hat{T}_{,x}^+ \quad \hat{T}_{,y}^+ \right]^T \quad (2.168)$$

The finite element representation of $\Theta_{\theta(xy)}^{ESL}$

$$\Theta_{\theta(xy)}^{e(ESL)} = B_{\theta(ESL)}^e(x, y)\Theta_{\theta(ESL)}^e \quad (2.169)$$

where

$$B_{\theta(ESL)}^e(x, y) = \left[B_{\theta(ESL)}^{e(1)}(x, y) \quad \cdot \quad \cdot \quad B_{\theta(ESL)}^{e(j)}(x, y) \quad \cdot \quad \cdot \quad B_{\theta(ESL)}^{e(n)}(x, y) \right] \quad (2.170)$$

$$\Theta_{\theta(ESL)}^e = \left[\Theta_{\theta(ESL)}^{e(1)}(x, y) \quad \cdot \quad \cdot \quad \Theta_{\theta(ESL)}^{e(j)}(x, y) \quad \cdot \quad \cdot \quad \Theta_{\theta(ESL)}^{e(n)}(x, y) \right] \quad (2.171)$$

and

$$B_{\theta(ESL)}^{e(j)}(x, y) = \begin{bmatrix} l_{\hat{T}^-}^j & 0 \\ l_{\hat{T}^-,x}^j & 0 \\ l_{\hat{T}^-,y}^j & 0 \\ 0 & l_{\hat{T}^+}^j \\ 0 & l_{\hat{T}^+,x}^j \\ 0 & l_{\hat{T}^+,y}^j \end{bmatrix}; \Theta_{\theta(ESL)}^e = \begin{bmatrix} \hat{T}^{-(j)} \\ \hat{T}^{+(j)} \end{bmatrix} \quad (2.172)$$

E. Fundamental Laws of Continuum Mechanics

In this section, a brief description of fundamental laws of continuum mechanics will be provided according to Malvern [41].

1. Conservation of Mass

The total mass m at time t of a continuous medium of density ρ , inside an arbitrary volume V which is fixed in the space, and bounded by surface S , Fig. 4 is

$$m = \int_V \rho(x, y, z, t) dV \quad (2.173)$$

If there is no creation or destruction of mass inside V , then the rate of increase of the total mass in the volume V must be equal to the rate of inflow of mass through the surface. According to this, we obtain

$$\frac{dm}{dt} = \int_V \left[\frac{d\rho}{dt} + \rho \nabla \cdot v \right] dV \quad (2.174)$$

The Eq. 2.174 is known as continuity equation

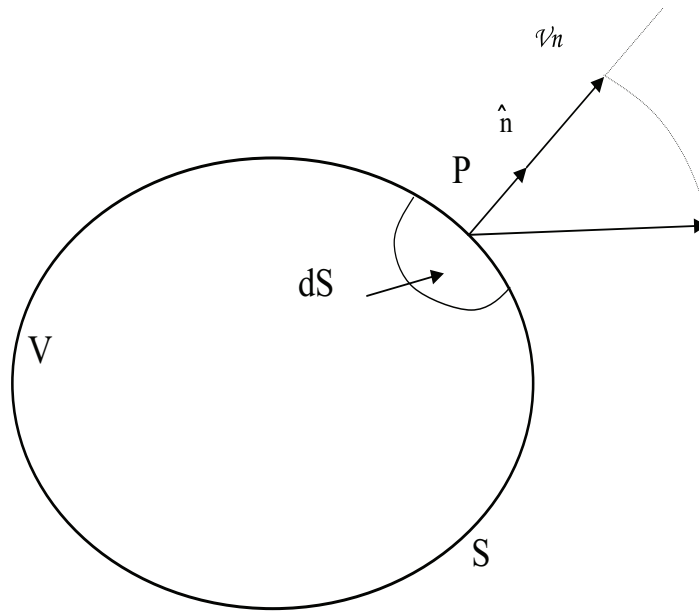


Fig. 4. Fixed volume V , bounded by the surface S

2. Linear Momentum Principle

This principle states that the rate of change of the total momentum of a given mass that occupies a volume V bounded by surface S is equal to the summation of external surface forces t per unit area and the body forces b per unit mass, Fig. 5.

$$\int_S t dS + \int_V \rho b dV = \frac{d}{dt} \int_V \rho v dV \quad (2.175)$$

If we substitute for each Cartesian term of t , the expression $t_i = \sigma_{ji} n_j$, being n the normal vector to the surface S , transform the surface integral by using the divergence theorem, and after some manipulations, we have the equation of motion

$$\sigma_{ji,j} + \rho b_i = \rho \dot{v}_i; \nabla \cdot \sigma + \rho b = \rho \frac{dv}{dt} \quad (2.176)$$

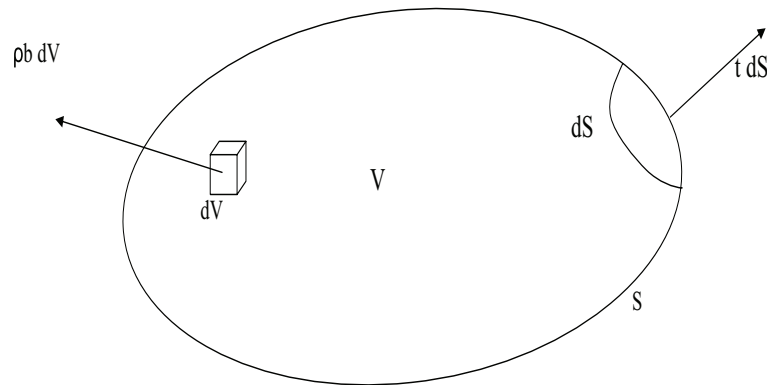


Fig. 5. Linear momentum balance

3. Angular Momentum Principle

In absence of distributed couples the rate of change of the angular momentum for a continuum medium of mass m is equal to the vector sum of the moment caused by external forces acting on medium.

$$\int_S (r \times t) dS + \int_V (r \times \rho b) dV = \frac{d}{dt} \int_V (r \times \rho v) dV \quad (2.177)$$

or in indicial notation

$$\int_S \epsilon_{ijk} x_j t_k^{\hat{n}} dS + \int_V \epsilon_{ijk} x_j \rho b_k dV = \frac{d}{dt} \int_V \epsilon_{ijk} x_j \rho v_k dV \quad (2.178)$$

The main consequence of this principle is the symmetry of the stress tensor $\sigma_{ij} = \sigma_{ji}$

4. First Law of Thermodynamics

This law states that the time rate of change of the total energy of the system is equal to the summation of the power and heat input into the system

$$\dot{E}_{total} = P_{input} + Q_{input} \quad (2.179)$$

The heat input Q_{input} is comprised of the heat conduction through the surface S , and the internal heat source, then

$$Q_{input} = - \int_S q \dot{n} dS + \int_V \rho r dV \quad (2.180)$$

Since we are analyzing piezoelectric materials, the power input P_{input} can be divided in two parts. The first one related to the mechanical power (P_{mec}) is the rate at which the external surface t and body b forces do work. The second part is the work generated by the electrical field (P_{ele}). Then, we have the following equations

$$P_{input} = P_{mec} + P_{ele} \quad (2.181)$$

$$P_{mec} = \int_S t \cdot v dS + \int_V \rho b \cdot v dV \quad (2.182)$$

$$P_{ele} = - \int_S \varphi \dot{D} \cdot n dS \quad (2.183)$$

Using the relation $t = \sigma \cdot n$ and transforming the surfaces integral by using the divergence theorem

$$Q_{input} = \int_V [-\nabla \cdot q + \rho r] dV \quad (2.184)$$

and

$$P_{input} = \int_V [\nabla \cdot (\sigma \cdot v) + \rho b \cdot v + \nabla \cdot (\varphi \dot{D})] dV \quad (2.185)$$

Therefore, using equation of motion and the relations for the electrical field into the previous expression, we have the energy equation

$$\rho \frac{du}{dt} = \sigma_{ij} \dot{\epsilon}_{ij} + \dot{D}_j E_j + \rho r - \frac{\partial q_j}{\partial x_j} \quad (2.186)$$

5. Second Law of Thermodynamics

This law states that when a system evolves from one state to other, the rate of entropy increase in the system is greater or equal that the entropy input rate. The equality holds if and only if the process is reversible. The equation that describes the previous statement is the Clausius-Duhem inequality

$$\frac{ds}{dt} - \frac{r}{\theta} + \frac{1}{\rho\theta}q_{i,i} - \frac{q_i}{\rho\theta^2}\theta_{,i} \geq 0 \quad (2.187)$$

Moreover, for reversible process, the conditions

$$\frac{ds}{dt} - \frac{r}{\theta} + \frac{1}{\rho\theta}q_{i,i} = 0 \quad (2.188)$$

$$-\frac{q_i}{\rho\theta^2}\theta_{,i} = 0 \quad (2.189)$$

must be satisfied

F. Constitutive Equation

As it was defined in [40] the electric enthalpy h is

$$h = U - E_i D_i \quad (2.190)$$

where U is the internal energy function. Then, the free enthalpy or Gibbs function Ψ is

$$\Psi = U - E_i D_i - s\theta \quad (2.191)$$

$$\dot{\Psi} = \dot{U} - E_i \dot{D}_i - \dot{E}_i D_i - \dot{s}\theta - s\dot{\theta} \quad (2.192)$$

After using the energy equation and the Classius-Duhem inequality for reversible process in Eq. 2.192

$$\dot{\Psi} = \sigma_{ij}\dot{\epsilon}_{ij} - D_i \dot{E}_i - s\dot{\theta} \quad (2.193)$$

or

$$\dot{\Psi} = \sigma : \varepsilon - D\dot{E} - s\dot{\theta} \quad (2.194)$$

$$\Psi = \Psi(\varepsilon_{ij}, E_i, \theta) \quad (2.195)$$

it is also true that

$$\dot{\Psi} = \frac{\partial \Psi}{\partial \varepsilon_{ij}} \dot{\varepsilon} + \frac{\partial \Psi}{\partial E_i} \dot{E}_i + \frac{\partial \Psi}{\partial \theta} \dot{\theta} \quad (2.196)$$

$$\left(\frac{\partial \Psi}{\partial \varepsilon_{ij}} - \sigma_{ij} \right) \dot{\varepsilon}_{ij} + \left(\frac{\partial \Psi}{\partial E_i} + D_i \right) \dot{E}_i + \left(\frac{\partial \Psi}{\partial \theta} + \eta \right) \dot{\theta} = 0 \quad (2.197)$$

$$\frac{\partial \Psi}{\partial \varepsilon_{ij}} = \sigma_{ij}, \quad \frac{\partial \Psi}{\partial E_i} = -D_i, \quad \frac{\partial \Psi}{\partial \theta} = -\eta \quad (2.198)$$

If we define Ψ as an extension of Helmholtz potential [42]

$$\begin{aligned} \Psi(\varepsilon_{ij}, E_i, \theta) = & \frac{1}{2} Q_{ijkl} \varepsilon_{ij} \varepsilon_{kl} - e_{ijk} E_i \varepsilon_{jk} - \frac{1}{2} \epsilon_{ij} E_i E_j \\ & - \lambda_{ij} \theta \varepsilon_{ij} - \beta_i E_i \theta - cT \log\left(\frac{T}{T_0}\right) \end{aligned} \quad (2.199)$$

Then, from Eq. 2.198

$$\begin{aligned} \sigma &= Q\varepsilon - eE - \lambda\theta \\ D &= e^T \varepsilon + \epsilon E + \beta\theta \\ \eta &= \lambda^T \varepsilon + \beta^T E + c \left[\log\left(\frac{T}{T_0}\right) + T_0 \right] \end{aligned} \quad (2.200)$$

where T_0 is the reference temperature. For small thermal changes about T_0 , we can make the first order approximation for the pure thermal term in the augmented Helmholtz potential as

$$c \left[\log\left(\frac{T}{T_0}\right) + T_0 \right] = \frac{1}{2} \frac{\rho c}{T_0} \theta^2 \quad (2.201)$$

where $\theta = T - T_0$. As a result, the constitutive equation for η is

$$\eta = \lambda^T \varepsilon + \beta^T E + c\theta \quad (2.202)$$

G. Fully Coupled Finite Element Formulation

The dynamic version of the principle of virtual work is

$$0 = \int_0^T (\delta U + \delta V - \delta K) dt \quad (2.203)$$

where δU is the virtual strain energy, δV is the virtual work done by the applied forces over the structure, and δK the virtual kinetic energy. For structures that contains piezoelectric materials, elastic and electrical field are present; therefore, the principle of virtual work for these materials can be expressed as

$$\int_V (\rho \ddot{u}_i \delta u_i + \sigma_{ij} \delta \varepsilon_{ij} - D_i \delta E_i) dV = \int_S (q_{u_i} \delta u_i + q_\phi \delta \phi) dS \quad (2.204)$$

The coupled heat transfer equation is

$$T \dot{\eta} + q_{i,i} = \gamma \quad (2.205)$$

where the relation between q_i and T is provided by the Fourier's heat conduction law

$$q_i = -\kappa_{ij} T_{,j} \quad (2.206)$$

Then, applying a variational principle

$$\int_V T \dot{\eta} \delta T dV + \int_V q_{i,i} \delta T dV = \int_V \gamma \delta T dV \quad (2.207)$$

and integrating by parts

$$\int_V T \dot{\eta} \delta T dV + \int_S q_i \hat{n}_i \delta T dS - \int_V q_i \delta T_{,i} dV = \int_V \gamma \delta T dV \quad (2.208)$$

Eq.(2.204) can be split as

$$\begin{aligned} \int_V (\rho \ddot{u}_i \delta u_i + \sigma_{ij} \delta \varepsilon_{ij}) dV &= \int_S q_{u_i} \delta u_i dS \\ - \int_V D_i \delta E_i dV &= \int_S q_\phi \delta \phi dS \end{aligned} \quad (2.209)$$

Replacing Eq. (2.206) in Eq. (2.205)

$$\int_V T \dot{\eta} \delta T dV + \int_V \kappa_{ij} T_{,j} \delta T_{,i} dV = \int_V \gamma \delta T dV - \int_S q_i \hat{n}_i \delta T dS \quad (2.210)$$

Writing the previous equations in a vector form

$$\begin{aligned} \int_V [\delta u_u^T \rho \ddot{u}_u + \delta \varepsilon^T \sigma] dV &= \int_S \delta u_u^T q_u dS \\ - \int_V \delta E^T D dV &= \int_S \delta \phi q_\phi dS \\ \int_V T \dot{\eta} \delta T dV + \int_V \delta \Theta K \Theta dV &= \int_V \gamma \delta T dV - \int_S q_\theta \hat{n} \delta T dS \end{aligned} \quad (2.211)$$

In the sequel, we are going to show the finite element formulation of each of the integral terms that comprises the equations in (2.211)

1. Equation Terms

a. $\int_V \delta u_u^T \rho \ddot{u}_u dV$

As it was shown in the previous sections, the finite element representation of the displacement field at the element level can be written as

$$u_u = \begin{bmatrix} N_{u(ESL)}^e & N_{u(LWT)}^e \end{bmatrix} \begin{bmatrix} u_{u(ESL)}^e \\ u_{u(LWT)}^e \end{bmatrix} \quad (2.212)$$

where any $N_{u(i)}^e$ can be expressed as the product of two matrices, one a function of the z and the other one a function of x and y

$$N_{u(i)}^e = N_{u(i)}^e(z) N_{u(i)}^e(x, y) \quad (2.213)$$

and, with the objective of simplification, i can take the values of 1 or 2 whether it is representing the ESL or the LWT representation, respectively. Therefore, we obtain

$$\int_V \delta u_u^T \rho \ddot{u}_u dV = \sum_e^{\#elem} \{\delta u_u^e\}^T [M_{uu}^e] \{\ddot{u}_u^e\} \quad (2.214)$$

with

$$M_{uu}^e = \int_{V^e} \begin{bmatrix} N_{u(1)}^{eT}(x, y) \bar{\rho}_{11} N_{u(1)}^e(x, y) & N_{u(1)}^{eT}(x, y) \bar{\rho}_{12} N_{u(2)}^e(x, y) \\ N_{u(2)}^{eT}(x, y) \bar{\rho}_{21} N_{u(1)}^e(x, y) & N_{u(2)}^{eT}(x, y) \bar{\rho}_{22} N_{u(2)}^e(x, y) \end{bmatrix} dV^e \quad (2.215)$$

and

$$\bar{\rho}_{ij} = \int_z N_{u(i)}^{eT}(z) \rho N_{u(j)}^e(z) dz \quad (2.216)$$

b. $\int_V \delta \varepsilon^T \sigma dV$

Using the constitutive equation (2.200) related to the stress vector σ

$$\begin{aligned} \sigma &= Q\varepsilon - eE - \lambda\theta \\ \theta &= T - T_0 \end{aligned} \quad (2.217)$$

the finite element representation of the strain ε , electrical potential E and thermal field θ at the element level can be written as

$$\varepsilon = \begin{bmatrix} B_{u(ESL)}^e & B_{u(LWT)}^e \end{bmatrix} \begin{bmatrix} u_{u(ESL)}^e \\ u_{u(LWT)}^e \end{bmatrix}; E = - \begin{bmatrix} B_{\phi(LWT)}^e \end{bmatrix} \begin{bmatrix} u_{\phi(LWT)}^e \end{bmatrix} \quad (2.218)$$

$$\theta = N_{\theta(ESL)} u_{\theta}^e - T_0 \quad (2.219)$$

$$\int_{V^e} \delta \varepsilon^T \sigma dV^e = \{\delta u_u^e\}^T \left[[K_{uu}^e] u_u^e - [K_{u\phi}^e] u_{\phi}^e - [K_{u\theta}^e] u_{\theta}^e + F_{u\theta}^e \right] \quad (2.220)$$

where

$$[K_{uu}^e] = \begin{bmatrix} K_{uu(11)}^e & K_{uu(12)}^e \\ K_{uu(21)}^e & K_{uu(22)}^e \end{bmatrix} \quad (2.221)$$

with

$$K_{uu(ij)}^e = \int_{S^e} \left[B_{u(i)}^{eT}(x, y) \bar{Q}_{ij} B_{u(j)}^e(x, y) \right] dS^e; \bar{Q}_{ij} = \int_z B_{u(i)}^{eT}(z) Q B_{u(j)}^e(z) dz \quad (2.222)$$

and

$$[K_{u\phi}^e] = \begin{bmatrix} K_{u\phi(12)}^e \\ K_{u\phi(22)}^e \end{bmatrix} \quad (2.223)$$

with

$$K_{u\phi(i2)}^e = \int_{S^e} \left[B_{u(i)}^{eT}(x, y) \bar{e}_{ij} \left[-B_{\phi(2)}^e(x, y) \right] \right] dS^e \quad (2.224)$$

$$\bar{e}_{i2} = \int_z B_{u(i)}^{eT}(z) e B_{\phi(2)}^e(z) dz \quad (2.225)$$

and

$$[K_{u\theta}^e] = \begin{bmatrix} K_{u\theta(11)}^e \\ K_{u\theta(21)}^e \end{bmatrix} \quad (2.226)$$

with

$$K_{u\theta(i1)}^e = \int_{S^e} \left[B_{u(i)}^{eT}(x, y) \bar{\lambda}_{i1} N_{\theta(1)}^e(x, y) \right] dS^e; \bar{\lambda}_{i1} = \int_z B_{u(i)}^{eT}(z) \lambda N_{\theta(1)}^e(z) dz \quad (2.227)$$

and

$$F_{u\theta}^e = \begin{bmatrix} F_{u\theta(1)}^e \\ F_{u\theta(2)}^e \end{bmatrix} \quad (2.228)$$

with

$$F_{u\theta(i)}^e = \int_S \left[B_{u(i)}^{eT}(x, y) \tilde{\lambda}_i \right] T_0 dS; \tilde{\lambda}_i = \int_z B_{u(i)}^{eT}(z) \lambda dz \quad (2.229)$$

c. $\int_S \delta u^T \bar{q}_u$

We define z_0 as the z coordinate where the force is supposed to be applied. In case of ESL z_0 will be the z coordinate of the midplane; however for LWT, it can usually be the top or the bottom of the plate. Then, at the element level we have

$$\int_{S^e} \delta u_u^T \bar{q}_u dS^e = \{\delta u_u^e\}^T F_u^e = \quad (2.230)$$

$$\{\delta u_u^e\}^T \int_S \begin{bmatrix} N_{u(1)}^{eT}(x, y) N_{u(1)}^{eT}(z_0) \\ N_{u(2)}^{eT}(x, y) N_{u(2)}^{eT}(z_0) \end{bmatrix} \text{diag} \begin{pmatrix} f_1(x, y) \\ f_2(x, y) \\ f_3(x, y) \end{pmatrix} dS \begin{Bmatrix} q_1 T F_{q_1} \\ q_2 T F_{q_2} \\ q_3 T F_{q_3} \end{Bmatrix} \quad (2.231)$$

where $f_i(x, y)$ and $T F_{q_i}$ are the functions that describe how the force q_i is applied over the plane and evolves with time, respectively. Therefore the expression

$$\int_V [\rho \ddot{u}_i \delta u_i + \sigma_{ij} \varepsilon_{ij}] dV = \int_S q_{u_i} \delta u_i dS \quad (2.232)$$

can be expressed as

$$[M_{uu}^e] \{\ddot{u}_u^e\} + [K_{uu}^e] \{u_u^e\} - [K_{u\phi}^e] \{u_\phi^e\} - [K_{u\theta}^e] \{u_\theta^e\} = \{F_u^e\} - \{F_{u\theta}^e\} \quad (2.233)$$

d. $-\int_V \delta E^T D dV$

Using the constitutive equation (2.200) related to the electrical displacement D

$$D = e^T \varepsilon + \epsilon E + \beta \theta \quad (2.234)$$

Then

$$-\int_{V^e} \delta E^T D dV^e = -\{\delta u_\phi^e\}^T \left[[K_{\phi u}^e] u_u^e - [K_{\phi\phi}^e] u_\phi^e - [K_{\phi\theta}^e] u_\theta^e - F_{\phi\theta}^e \right] \quad (2.235)$$

where

$$[K_{\phi u}^e] = \begin{bmatrix} K_{\phi u(21)}^e & K_{\phi u(22)}^e \end{bmatrix} \quad (2.236)$$

and

$$K_{u\phi(2i)}^e = \int_{V^e} \left[[-B_{\phi(2)}^{eT}(x, y)] \bar{e}_{2i}^T B_{u(i)}^e(x, y) \right] dV^e \quad (2.237)$$

$$\bar{e}_{2i}^T = \int_z B_{\phi(2)}^{eT}(z) e B_{u(i)}^e(z) dz \quad (2.238)$$

where

$$\left[K_{\phi\phi}^e \right] = \left[K_{\phi\phi(22)}^e \right] \quad (2.239)$$

and

$$K_{\phi\phi(22)}^e = \int_{V^e} \left[[-B_{\phi(2)}^{eT}(x, y)] \bar{e}_{22} [-B_{\phi(2)}^{eT}(x, y)] \right] dV^e \quad (2.240)$$

$$\bar{e}_{22} = \int_z B_{\phi(2)}^{eT}(z) \epsilon B_{\phi(2)}^e(z) dz \quad (2.241)$$

where

$$\left[K_{\phi\theta}^e \right] = \left[K_{\phi\theta(21)}^e \right] \quad (2.242)$$

and

$$K_{\phi\theta(21)}^e = \int_{V^e} \left[B_{\phi(2)}^{eT}(x, y) \bar{\beta}_{21} N_{\theta(1)}^e(x, y) \right] dV^e; \bar{\beta}_{21} = \int_z B_{\phi(2)}^{eT}(z) \beta N_{\theta(1)}^e(z) dz \quad (2.243)$$

where

$$F_{\phi\theta}^e = \left[F_{\phi\theta(1)}^e \right] \quad (2.244)$$

and

$$F_{\phi\theta(i)}^e = \int_{S^e} \left[[-B_{\phi(2)}^{eT}(x, y)] \tilde{\beta}_2 \right] T_0 dS^e; \tilde{\beta}_2 = \int_z B_{\phi(2)}^{eT}(z) \beta dz \quad (2.245)$$

e. $\int_S \delta\phi q_\phi dS$

In the case of smart materials, voltages are normally imposed or calculated from other variables or from a control strategy, and electrical flux input is rarely applied.

Hence, the term F_ϕ can be set to zero.

$$\int_{S^e} \delta\phi q_\phi dS^e = \delta\phi F_\phi^e = 0 \quad (2.246)$$

Therefore the expression

$$-\int_{V^e} \delta E^T D dV^e = \int_{S^e} \delta\phi q_\phi dS^e \quad (2.247)$$

can be written as

$$-\left[K_{\phi u}^e \right] \{u_u^e\} - \left[K_{\phi\phi}^e \right] \{u_\phi^e\} - \left[K_{\phi\theta}^e \right] \{u_\theta^e\} = \{F_\phi^e\} - \{F_{\phi\theta}^e\} \quad (2.248)$$

f. $\int_V T \dot{\eta} \delta T dV$

Using the constitutive equation (2.200) related to the entropy η

$$\dot{\eta} = \lambda^T \dot{\varepsilon} + \beta^T \dot{E} + c \frac{\dot{T}}{T} \quad (2.249)$$

Then

$$\int_{V^e} \delta u_\theta^{eT} T \dot{\eta} dV^e = \{\delta u_\theta^e\}^T \left[[C_{\theta u}^e] \dot{u}_u^e + [C_{\theta\phi}^e] \dot{u}_\phi^e + [C_{\theta\theta}^e] \dot{u}_\theta^e \right] \quad (2.250)$$

The finite element representation of the time rate for the strain $\dot{\varepsilon}$, electric potential \dot{E} and thermal field $\dot{\theta}$ at element level can be written as

$$\dot{\varepsilon} = \begin{bmatrix} B_{u(ESL)}^{eT} & B_{u(LWT)}^{eT} \end{bmatrix} \begin{bmatrix} \dot{u}_{u(ESL)}^e \\ \dot{u}_{u(LWT)}^e \end{bmatrix}; \dot{E} = - \begin{bmatrix} B_{\phi(LWT)}^e \end{bmatrix} \begin{bmatrix} \dot{u}_{\phi(LWT)}^e \end{bmatrix} \quad (2.251)$$

$$\dot{\theta} = N_{\theta(ESL)} \dot{u}_\theta^e \quad (2.252)$$

where

$$\begin{bmatrix} C_{\theta u}^e \end{bmatrix} = \begin{bmatrix} C_{\theta u(11)}^e & C_{\theta u(12)}^e \end{bmatrix} \quad (2.253)$$

and

$$C_{\theta u(1i)} = \int_{V^e} N_{\theta(1)}^{eT}(x, y) \bar{\lambda}_{1i}^T(x, y) B_{u(i)}^e(x, y) dV^e \quad (2.254)$$

$$\bar{\lambda}_{1i}^T(x, y) = \int_z N_{\theta(1)}^T(z) [T\lambda^T] B_{u(i)}(z) dz \quad (2.255)$$

where

$$\left[C_{\theta\phi}^e \right] = \left[C_{\theta\phi(12)}^e \right] \quad (2.256)$$

and

$$C_{\theta\phi(12)} = \int_{V^e} N_{\theta(1)}^{eT}(x, y) \bar{\beta}_{12}^T(x, y) B_{\phi(2)}^e(x, y) dV^e \quad (2.257)$$

$$\bar{\beta}_{12}^T(x, y) = \int_z N_{\theta(1)}^T(z) [T\beta^T] B_{\phi(2)}(z) dz \quad (2.258)$$

where

$$\left[C_{\theta\theta}^e \right] = \left[C_{\theta\theta(11)}^e \right] \quad (2.259)$$

and

$$C_{\theta\theta(11)} = \int_{V^e} N_{\theta(1)}^{eT}(x, y) \bar{c}_{11}(x, y) N_{\theta(1)}^e(x, y) dV^e \quad (2.260)$$

$$\bar{c}_{11}(x, y) = \int_z N_{\theta(1)}^T(z) c N_{\theta(1)}^T(z) dz \quad (2.261)$$

g. $\int_V \delta\Theta^T K\Theta dV$

$$\int_{V^e} \delta\Theta^T K\Theta dV^e = \{\delta u_{\theta}^e\}^T [K_{\theta\theta}^e] \{u_{\theta}^e\} \quad (2.262)$$

The finite element representation of the temperature gradient Θ is

$$\Theta = B_{\theta(1)} u_{\theta}^e \quad (2.263)$$

where

$$[K_{\theta\theta}^e] = [K_{\theta\theta(11)}^e] \quad (2.264)$$

$$[K_{\theta\theta(11)}^e] = \int_{V^e} B_{\theta(1)}^{eT} \bar{K}_{11}^e B_{\theta(1)}^e dV^e; \bar{K}_{11}^e = \int_z B_{\theta(1)}^T(z) K B_{\theta(1)}(z) dz \quad (2.265)$$

$$\text{h. } - \int_S \{\delta u_\theta^e\}^T \bar{q}_\theta \cdot \hat{n} dS$$

$$F_\theta^e = \int_{S^e} \{\delta u_\theta^e\}^T \bar{q}_\theta \cdot \hat{n} dS^e \quad (2.266)$$

Therefore, the equation

$$\int_{V^e} T \dot{\eta} \delta T dV^e + \int_{V^e} \delta \Theta K \Theta dV^e = - \int_{S^e} \{\delta u_\theta^e\}^T \bar{q}_\theta \cdot \hat{n} dS^e \quad (2.267)$$

can be written as

$$\begin{bmatrix} C_{\theta u}^e \end{bmatrix} \{\dot{u}_u^e\} + \begin{bmatrix} C_{\theta \phi}^e \end{bmatrix} \{\dot{u}_\phi^e\} + \begin{bmatrix} C_{\theta \theta}^e \end{bmatrix} \{\dot{u}_\theta^e\} + \begin{bmatrix} K_{\theta\theta}^e \end{bmatrix} \{u_\theta^e\} = -F_\theta^e \quad (2.268)$$

Finally, using Eq. (2.233), Eq. (2.248) and Eq. (2.268) and splitting the piezoelectric effect into a sensor and actuator effects, we have

$$\begin{bmatrix} [M_{uu}^e] & 0 & 0 & 0 \\ 0 & 0 & 0 & 0 \\ 0 & 0 & 0 & 0 \\ 0 & 0 & 0 & 0 \end{bmatrix} \begin{Bmatrix} \ddot{u}_u^e \\ \ddot{u}_{\phi_s}^e \\ \ddot{u}_{\phi_a}^e \\ \ddot{u}_\theta^e \end{Bmatrix} + \begin{bmatrix} [C_{uu}^e] & 0 & 0 & 0 \\ 0 & 0 & 0 & 0 \\ 0 & 0 & 0 & 0 \\ [C_{\theta u}^e] & [C_{\theta \phi_s}^e] & [C_{\theta \phi_a}^e] & [C_{\theta\theta}^e] \end{bmatrix} \begin{Bmatrix} \dot{u}_u^e \\ \dot{u}_{\phi_s}^e \\ \dot{u}_{\phi_a}^e \\ \dot{u}_\theta^e \end{Bmatrix} +$$

$$\begin{bmatrix} [K_{uu}^e] & [K_{u\phi_s}^e] & [K_{u\phi_a}^e] & [K_{u\theta}^e] \\ [K_{\phi_s u}^e] & [K_{\phi_s \phi_s}^e] & 0 & [K_{\phi_s \theta}^e] \\ [K_{\phi_a u}^e] & 0 & [K_{\phi_a \phi_a}^e] & [K_{\phi_a \theta}^e] \\ 0 & 0 & 0 & [K_{\theta\theta}^e] \end{bmatrix} \begin{Bmatrix} u_u^e \\ u_{\phi_s}^e \\ u_{\phi_a}^e \\ u_\theta^e \end{Bmatrix} = \begin{Bmatrix} F_u^e \\ F_{\phi_s}^e \\ F_{\phi_a}^e \\ F_\theta^e \end{Bmatrix} - \begin{Bmatrix} F_{u\theta}^e \\ F_{\phi_s \theta}^e \\ F_{\phi_a \theta}^e \\ 0 \end{Bmatrix}$$

(2.269)

which is the finite element formulation of a fully coupled elastic, electrical and thermal dynamical system, which is normally present in smart materials.

CHAPTER III

STATIC ANALYSIS

In the previous chapter, we developed the general formulation for a dynamical system with mechanical, thermal and electrical fields. In this chapter, we will focus our attention on the static part of the equation 2.78. Then,

$$\begin{bmatrix} [K_{uu}^e] & [K_{u\phi_s}^e] & [K_{u\phi_a}^e] & [K_{u\theta}^e] \\ [K_{\phi_s u}^e] & [K_{\phi_s \phi_s}^e] & 0 & [K_{\phi_s \theta}^e] \\ [K_{\phi_a u}^e] & 0 & [K_{\phi_a \phi_a}^e] & [K_{\phi_a \theta}^e] \\ 0 & 0 & 0 & [K_{\theta\theta}^e] \end{bmatrix} \begin{Bmatrix} u_u^e \\ u_{\phi_s}^e \\ u_{\phi_a}^e \\ u_{\theta}^e \end{Bmatrix} = \begin{Bmatrix} F_u^e \\ F_{\phi_s}^e \\ F_{\phi_a}^e \\ F_{\theta}^e \end{Bmatrix} - \begin{Bmatrix} F_{u\theta}^e \\ F_{\phi_s \theta}^e \\ F_{\phi_a \theta}^e \\ 0 \end{Bmatrix} \quad (3.1)$$

Since TSDT is the most accurate theory and has shown superiority over CLPT and FSDT (see Reddy [29]), the IESL theory developed in Chapter I is used for TSDT. Therefore, in the sequel, the improved third-order shear deformation theory (ITSDT) represents the IESL version of the TSDT.

The ITSDT is applied to composite and FGM plates in order to study its performance in thermoelastic problems, then, comparisons with the LWT and TSDT models are made. In the case of the electrical field, we add a piezoelectric layer to the FGM plate and we use not only the ITSDT model but also ITSDT + LWT, which is the multiple assumed displacement field version for ITSDT.

A. Symmetric Composite Laminates

The first case to be analyzed is a simply supported S (SS1 in [29, 39]) cross-ply square laminate under sinusoidally distributed transverse load. The laminate is comprised of 4 plies (0/90/90/0) of equal thickness. As a comparison, we use the 3D elasticity solution developed in [43] and [44]. The material properties used here are

typical of the graphite-epoxy material with properties

$$E_1 = 25E_2, G_{12} = G_{13} = 0.5E_2, G_{23} = 0.2E_2, \nu_{12} = 0.25 \quad (3.2)$$

Using the symmetry of the problem, a quarter plate with a mesh of 4×4 elements is considered as the computational domain. In the case of LWT the thickness is discretized using 4 layers. Accordingly, the corresponding sinusoidal load

$$q(x, y) = q_0 \cos\left(\frac{\pi x}{a}\right) \cos\left(\frac{\pi y}{b}\right) \quad (3.3)$$

Table I. Comparison of several formulations with the analytical solution proposed by Pagano

b/h	Theory	Element	\bar{w}	$\bar{\sigma}_{xx}$	$\bar{\sigma}_{yy}$	$\bar{\sigma}_{xy}$	$\bar{\sigma}_{xz}$	$\bar{\sigma}_{yz}$
	ESL		0.7370	0.5590	0.4010	0.0276	0.3010	0.1960
	LWT	4×4Q9	0.7342	0.5524	0.3982	0.0273	0.2988	0.1826
10	ITSdT	4×4C4	0.7179	0.5554	0.3881	0.0271	0.4957	0.1586
	TSDT	4×4C4	0.7146	0.5412	0.3861	0.0266	0.4915	0.1520
	ESL		0.5128	0.5430	0.3080	0.0230	0.3280	0.1560
	LWT	4×4Q9	0.5120	0.5384	0.3063	0.0229	0.3252	0.1446
20	ITSdT	4×4C4	0.5074	0.5396	0.3032	0.0228	0.5329	0.1271
	TSDT	4×4C4	0.5060	0.5354	0.3022	0.0227	0.5260	0.1226
	ESL		0.4347	0.5390	0.2710	0.0214	0.3390	0.1390
	LWT	4×4Q9	0.4329	0.5317	0.2669	0.0211	0.3370	0.1307
100	ITSdT	4×4C4	0.4344	0.5352	0.2690	0.0212	0.5476	0.1144
	TSDT	4×4C4	0.4343	0.5350	0.2690	0.0212	0.5396	0.1109

Moreover, we are going to use the following nondimensionalized quantities in the

analysis

$$\begin{aligned}
\bar{w} &= w_0(0, 0) \frac{E_2 h^3}{b^4 q_0} \quad , \quad \bar{\sigma}_{xx} = \sigma_{xx}(0, 0, \frac{h}{2}) \frac{h^2}{b^2 q_0} \\
\bar{\sigma}_{yy} &= \sigma_{yy}(0, 0, \frac{h}{4}) \frac{h^2}{b^2 q_0} \quad , \quad \bar{\sigma}_{xy} = \sigma_{xy}(\frac{a}{2}, \frac{a}{2}, -\frac{h}{2}) \frac{h^2}{b^2 q_0} \\
\bar{\sigma}_{xz} &= \sigma_{xz}(\frac{a}{2}, 0, 0) \frac{h}{b q_0} \quad , \quad \bar{\sigma}_{yz} = \sigma_{yz}(0, \frac{b}{2}, 0) \frac{h}{b q_0}
\end{aligned} \tag{3.4}$$

where a , b and h are the length, width and thickness of the plate. The origin of the coordinate is taken in the center point of the thickness of the bottom left corner. In other words, $0 \leq x \leq a/2$, $0 \leq y \leq b/2$ and $-h/2 \leq z \leq h/2$. Additionally, the stresses that results from the Finite Element Analysis were evaluated at the reduced Gauss points. In our analysis, three kinds of elements are employed. Firstly, a 9 node LWT element with quadratic Lagrange interpolation in the plane and a quadratic Lagrange interpolation function over the thickness for each layer is used. Secondly, a 4 node TSDT element is used with Hermite and Lagrangian interpolation functions. Finally, a 4 node ITSDT with similar interpolation functions as in TSDT (see Chapter I).

Observing the numerical results from Table I, LWT shows acceptable agreement with the 3-D elasticity model for different values of span-thickness ratios. ITSDT shows little improvement with respect of TSDT and that can be clearly noticed when b/h is 10. Another important aspect is that ITSDT does not experience shear locking effect as we can see when $b/h = 100$.

Since little improvement of ITSDT is observed when we need to analyze thick plates. Figures 6 to 11 show the behavior of this theory in comparison to LWT and TSDT for a very thick plate $b/h = 4$. Likewise the case when $b/h = 10$, ITSDT results are very similar to the ones obtained by TSDT; however there are some differences that are worthy to point out. First, the ITSDT predicts a vertical displacements

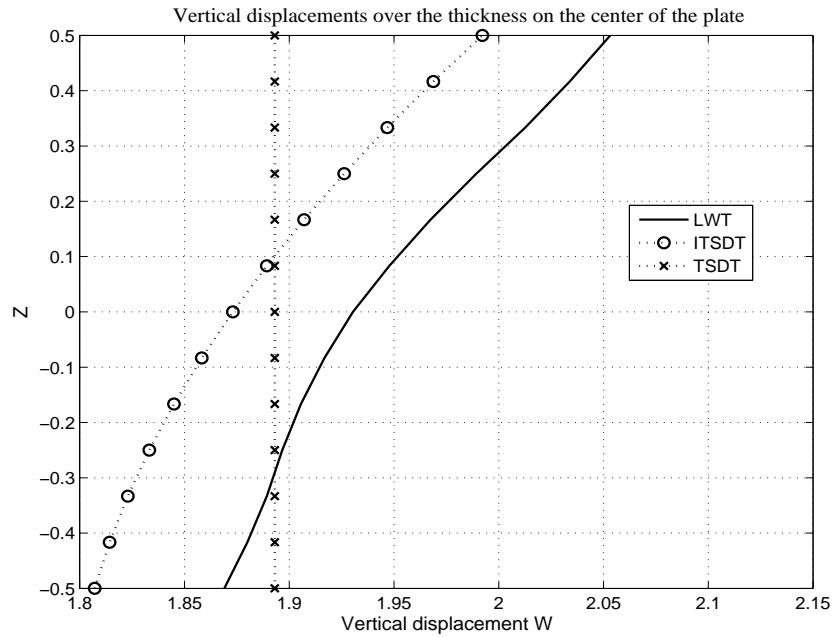


Fig. 6. \bar{w} through thickness for a composite plate under mechanical load

profile over the thickness similar to that predicted by LWT (see Fig. 6). Secondly, the profile of the vertical displacement along the plate length are better described by ITSDT when compared with TSDT (see Fig. 11).

B. Composite Plate Laminates with Different Boundary Conditions

Using the same mechanical load and material properties, we can study how ITSDT behaves for different laminate, low span to thickness ratios and different boundary conditions. In this case, the plate is simply supported in two opposite sides and the other two sides can be either simply supported (S), clamped (C) or free edges (F). When all the edges are simple supported the computational domain is a quarter plate with a mesh of 8×8 elements ; however for other cases a half plate model is considered with a mesh of 12×6 elements. LWT will be employed as a reference to study the performance of ITSDT. Moreover, the two stack plies are going to be

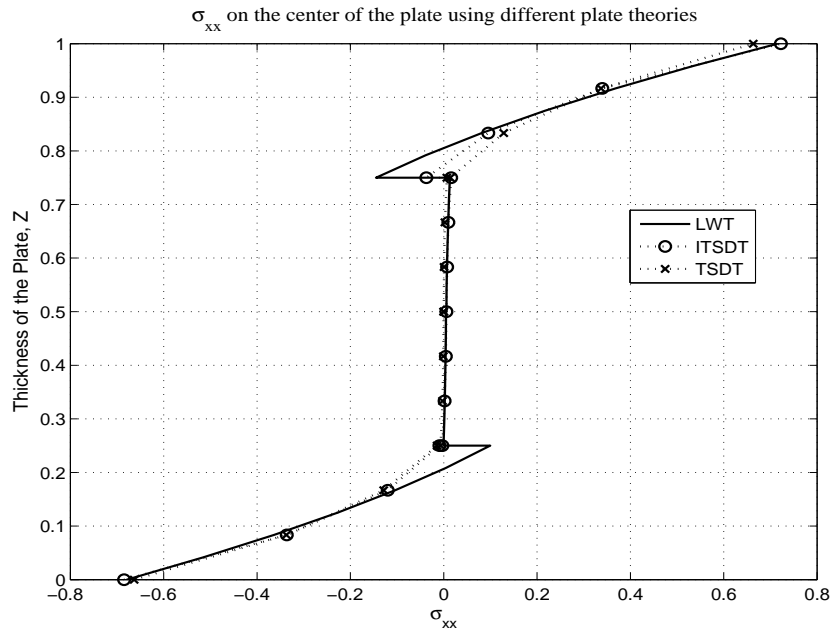


Fig. 7. $\bar{\sigma}_{xx}$ through thickness for a composite plate under mechanical load

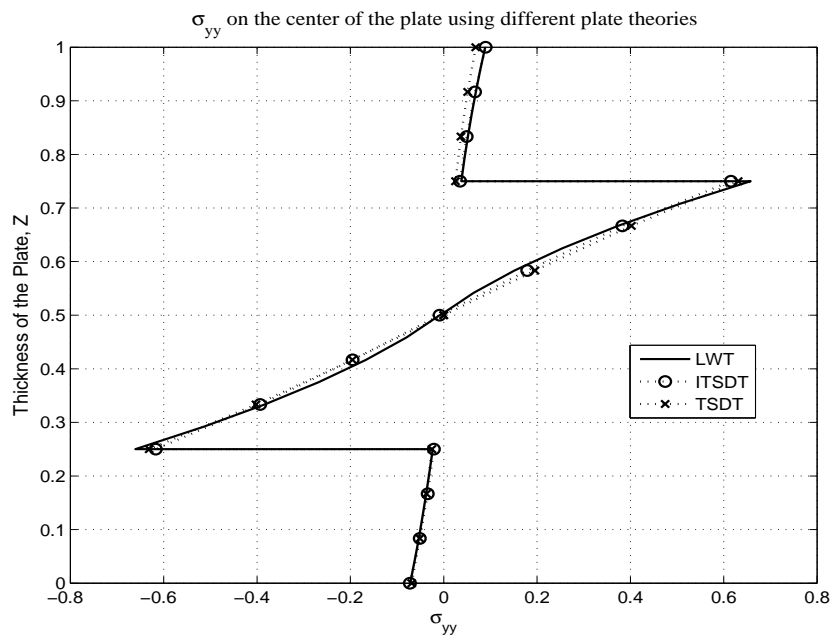


Fig. 8. $\bar{\sigma}_{yy}$ through thickness for a composite plate under mechanical load

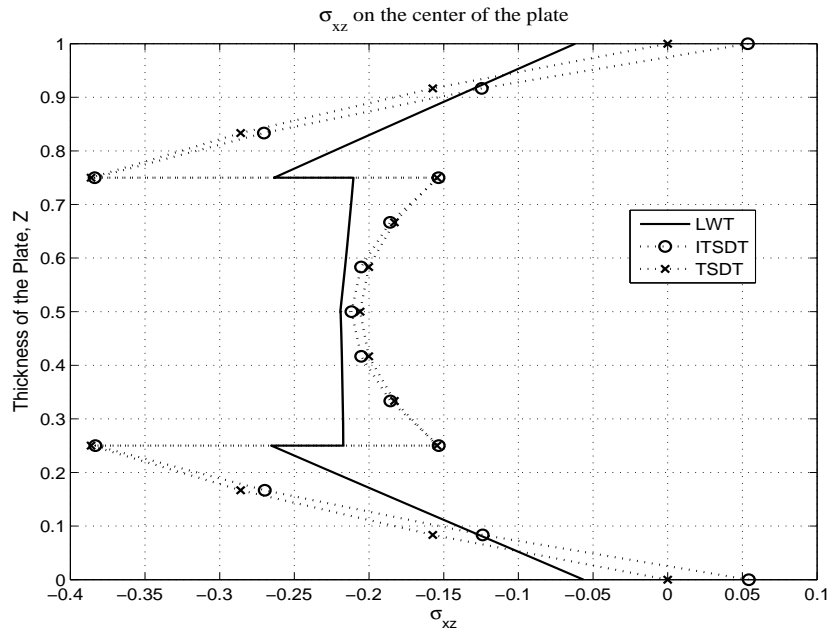


Fig. 9. $\bar{\sigma}_{xz}$ through thickness for a composite plate under mechanical load

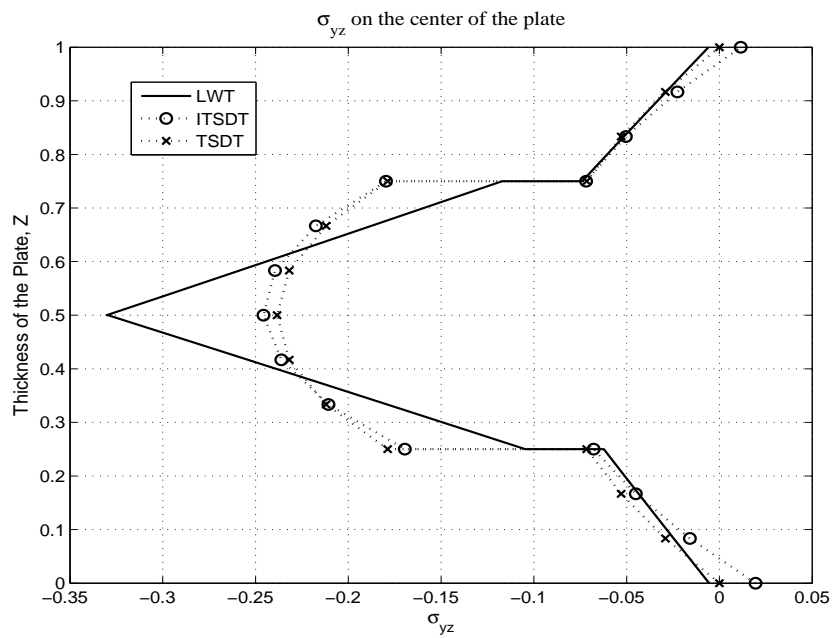


Fig. 10. $\bar{\sigma}_{yz}$ through thickness for a composite plate under mechanical load

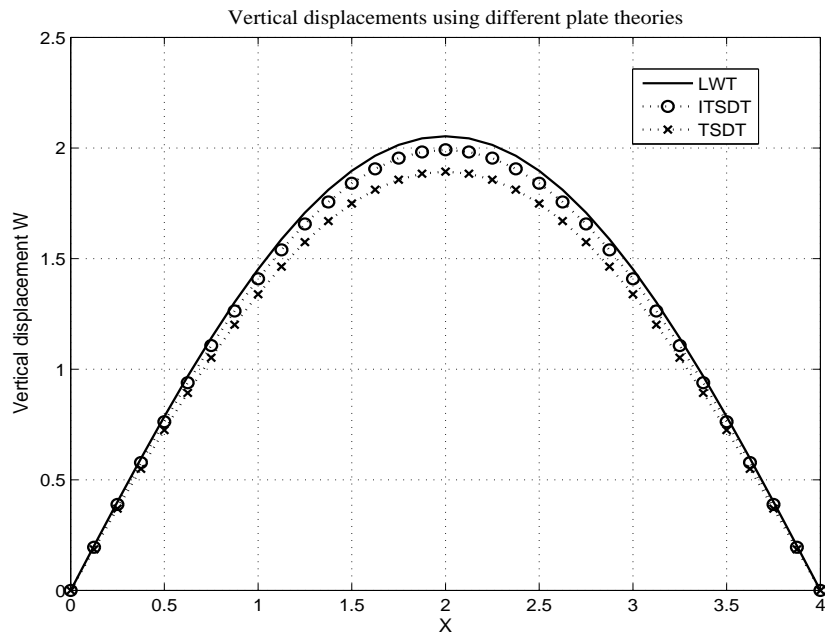


Fig. 11. \bar{w} through thickness for a composite plate under mechanical load $(0/90)_1$, 2 layers and $(0/90)_5$, 10 layers.

In Tables II and III, we can see that for boundary conditions different from SS the ITSDT provides results that are in good agreement with LWT, specially for the vertical displacements. In this case the improvement can be noticed when the number of layers and the span to thickness ratio are small. In other words, ITSDT performs better when the plate is thick and has few material properties changes (less inhomogeneous).

Table II. w and σ_{xx} of cross-ply square plates with various boundary conditions

	# Lay	b/h	Theory	SS	SC	CC	FF	FS	FC
\bar{w}	2	5	LWT	1.6614	1.8012	1.1636	2.6620	2.6424	1.7926
			ITSDDT	1.6781	1.7996	1.1467	2.6842	2.6648	1.7910
			TSDT	1.6647	1.7253	1.0689	2.6174	2.5940	1.7184
\bar{w}	2	10	LWT	1.2146	1.2026	0.6313	2.0018	1.9778	1.1961
			ITSDDT	1.2172	1.1948	0.6189	2.0017	1.9780	1.1884
			TSDT	1.2141	1.1802	0.6048	1.9854	1.9607	1.1742
\bar{w}	10	5	LWT	1.2890	1.4368	1.0759	1.8915	1.8851	1.4324
			ITSDDT	1.1319	1.2364	0.9005	1.6636	1.6569	1.2320
			TSDT	1.1292	1.2115	0.8677	1.6509	1.6434	1.2075
\bar{w}	10	10	LWT	0.6575	0.6677	0.4287	0.9774	0.9680	0.6641
			ITSDDT	0.6171	0.6109	0.3746	0.9187	0.9091	0.6074
			TSDT	0.6159	0.6069	0.3698	0.9154	0.9054	0.6035
$\bar{\sigma}_{xx}$	2	5	LWT	7.2889	2.9223	4.0652	2.4318	2.1013	2.5709
			ITSDDT	7.4836	3.0880	4.3487	2.5240	2.2128	2.7957
			TSDT	8.3562	4.1084	5.6534	3.1268	2.7870	3.7661
$\bar{\sigma}_{xx}$	2	10	LWT	7.2036	3.1900	4.4988	2.4366	2.0798	2.9110
			ITSDDT	7.2443	3.1792	4.5595	2.4452	2.1047	2.9927
			TSDT	7.4426	3.4592	4.9198	2.5880	2.2442	3.2506
$\bar{\sigma}_{xx}$	10	5	LWT	5.9627	2.4353	3.3424	2.1716	1.9830	2.1729
			ITSDDT	5.7861	2.3837	3.2786	2.0692	1.8731	2.0624
			TSDT	6.3279	3.0031	4.0442	2.4615	2.2479	2.5944
$\bar{\sigma}_{xx}$	10	10	LWT	5.2804	2.0989	2.9969	1.8686	1.6045	1.8882
			ITSDDT	5.2310	2.1191	3.0258	1.8405	1.5696	1.8727
			TSDT	5.3385	2.2589	3.2095	1.9128	1.6375	1.9924

Table III. σ_{yz} and σ_{xy} of cross-ply square plates with various boundary conditions

	# Lay	b/h	Theory	SS	SC	CC	FF	FS	FC
$\bar{\sigma}_{yz}$	2	5	LWT	2.9223	2.9397	2.0637	4.2892	4.2469	3.0359
			ITSDT	2.8596	2.8045	1.9798	4.1134	4.0726	2.8974
			TSDT	3.1484	2.9859	2.0611	4.4467	4.3893	3.0933
$\bar{\sigma}_{yz}$	2	10	LWT	2.9767	2.6517	1.6204	4.3293	4.2559	2.7705
			ITSDT	2.9107	2.5230	1.5880	4.1286	4.0580	2.6364
			TSDT	3.1844	2.7466	1.6974	4.4783	4.3948	2.8689
$\bar{\sigma}_{yz}$	10	5	LWT	2.2936	2.4671	1.9054	3.2688	3.2538	2.5335
			ITSDT	3.3929	3.5687	2.6859	4.8426	4.8164	3.6736
			TSDT	3.3559	3.4619	2.5604	4.7728	4.7433	3.5716
$\bar{\sigma}_{yz}$	10	10	LWT	2.3545	2.2580	1.5341	3.3335	3.2919	2.3425
			ITSDT	3.4621	3.2290	2.1091	4.9017	4.8348	3.3604
			TSDT	3.4021	3.1524	2.0471	4.8042	4.7360	3.2829
$\bar{\sigma}_{xy}$	2	5	LWT	0.5475	0.3381	0.2692	0.0285	0.0309	-0.0201
			ITSDT	0.5591	0.2155	0.1639	0.0434	0.0476	-0.0444
			TSDT	0.5570	0.1548	0.1164	0.0682	0.0735	-0.0420
$\bar{\sigma}_{xy}$	2	10	LWT	0.5305	0.1811	0.1384	0.0467	0.0481	-0.0385
			ITSDT	0.5327	0.1258	0.0920	0.0724	0.0743	-0.0652
			TSDT	0.5316	0.1086	0.0792	0.0837	0.0858	-0.0691
$\bar{\sigma}_{xy}$	10	5	LWT	0.2898	0.1636	0.1412	0.0206	0.0251	-0.0059
			ITSDT	0.2767	0.0555	0.0448	0.0261	0.0342	-0.0226
			TSDT	0.2758	0.0363	0.0274	0.0353	0.0440	-0.0187
$\bar{\sigma}_{xy}$	10	10	LWT	0.2374	0.0897	0.0751	0.0250	0.0286	-0.0168
			ITSDT	0.2340	0.0424	0.0335	0.0373	0.0425	-0.0311
			TSDT	0.2324	0.0386	0.0297	0.0384	0.0435	-0.0308

C. Functionally Graded Plates (FGM)

In the previous section, the numerical performance of ITSDT to analyze typical composite material plates was studied. The inhomogeneity of the material is represented by a function that is piece-wise continuous along the thickness. Unlike the classical composite materials, the FGMs are inhomogeneous composites in which material properties change continuously according to a specific function that depends on the spatial coordinates. For this reason, FGMs can be considered as spatial composites. Since this work is related to plates, the function that governs how the material varies will be dependent of the z coordinate only, meanwhile homogeneity over the plane is implicitly assumed. In this section, we are going to study two cases. In the first case, the elastic and thermal field for a FGM plate are going to be explored using several finite element theories, as it was done in the previous section. In the second case, a piezoelectric layer is going to be added to the bottom part of the FGM plate; therefore a thermal, elastic and electric analysis can be carried out.

1. FGM Plate

Here only the FGM part of the plate in [33] will be employed. Similarly to this work, we consider a composite plate comprised of a matrix phase denoted by 1 and a particulate phase denoted by 2. The composite contains spherical particles, which act as reinforcement, randomly distributed in the plane of the plate. As a consequence, the locally effective bulk modulus K , the shear modulus G are given by the Mori-Tanaka formulas (Appendix A). The expressions for the effective heat conductivity κ and the thermal expansion coefficient α can be found in Appendix A, too. For our case, nickel-based alloy, Monel (70Ni-30Cu), represents the matrix phase and Zirconia

the particulate one. Their material properties are

$$\begin{aligned}
 K_1 &= 227.24 \times 10^9 N/m^2, & K_2 &= 125.83 \times 10^9 N/m^2 \\
 G_1 &= 65.55 \times 10^9 N/m^2, & G_2 &= 58.077 \times 10^9 N/m^2 \\
 \alpha_1 &= 15.00 \times 10^{-6}/K, & \alpha_2 &= 10.00 \times 10^{-6}/K \\
 \kappa_1 &= 25.00 W/mK, & \kappa_2 &= 2.09 W/mK
 \end{aligned} \tag{3.5}$$

The volume fraction function of the particulate phase V_2 is

$$V_2 = \left(\frac{z}{h}\right)^n \tag{3.6}$$

In order to generate numerical results to be compared with ITSDT and the other finite element theories, the matrix transfer formulation in combination with asymptotic expansion presented in [33] (Asymt) was implemented and applied to this problem. For the finite element analysis, a quarter plate is selected as the computational domain with a mesh of 4×4 elements. The nonzero applied loads are

$$\begin{bmatrix} \hat{q}^+ & \hat{T}^+ \end{bmatrix} = \begin{bmatrix} \hat{q}_0^+ & \hat{T}_0^+ \end{bmatrix} \cos\left(\frac{\pi x}{a}\right) \cos\left(\frac{\pi y}{b}\right) \tag{3.7}$$

and the plate is simple supported and the temperature in its bottom part and edges is equal to zero. Moreover, the peak of the physical quantities are nondimensionalized by

$$\begin{aligned}
 \begin{bmatrix} \bar{u} & \bar{w} \end{bmatrix} &= \begin{bmatrix} \bar{u}_0(a, 0) & \bar{w}(0, 0) \end{bmatrix} \frac{1}{Pa} \\
 \begin{bmatrix} \bar{\sigma}_{xx} & \bar{\sigma}_{xy} & \bar{\sigma}_{xz} & \bar{\sigma}_{zz} \end{bmatrix} &= \begin{bmatrix} \bar{\sigma}_{xx}(0, 0, z) & \bar{\sigma}_{xy}(a, b, z) & \bar{\sigma}_{xz}(a, 0, z) & \bar{\sigma}_{zz}(0, 0, z) \end{bmatrix} \frac{1}{Pc^*}
 \end{aligned} \tag{3.8}$$

Table IV. \bar{u} and \bar{w} for a FGM plate under a sinusoidal mechanical load

	b/h	Theory	$z = 0$	$z = 0.10$	$z = 0.55$	$z = 1$
\bar{u}	4	Asymt	-0.0464	-0.0357	0.0036	0.0467
		LWT	-0.0464	-0.0357	0.0036	0.0467
		ITSDT	-0.0463	-0.0356	0.0036	0.0465
		TSDT	-0.0416	-0.0311	0.0053	0.0446
	10	Asymt	-0.2821	-0.2227	0.0352	0.2953
		LWT	-0.2826	-0.2229	0.0352	0.2958
		ITSDT	-0.2819	-0.2225	0.0353	0.2952
		TSDT	-0.2475	-0.1941	0.0350	0.2665
50	Asymt	-7.0084	-5.5627	0.9337	7.4121	
	LWT	-7.0391	-5.5839	0.9369	7.4454	
	ITSDT	-7.0053	-5.5596	0.9367	7.4154	
	TSDT	-6.1291	-4.8521	0.8834	6.6042	
\bar{w}	4	Asymt	0.1443	0.1467	0.1522	0.1521
		LWT	0.1442	0.1466	0.1521	0.1520
		ITSDT	0.1442	0.1466	0.1524	0.1522
		TSDT	0.1421	0.1421	0.1421	0.1421
	10	Asymt	1.9093	1.9152	1.9253	1.9126
		LWT	1.9080	1.9138	1.9240	1.9113
		ITSDT	1.9093	1.9153	1.9256	1.9127
		TSDT	1.7190	1.7190	1.7190	1.7190
50	Asymt	230.1858	230.2149	230.2625	230.1873	
	LWT	229.0032	229.0313	229.0771	229.0052	
	ITSDT	230.1849	230.2151	230.2628	230.1870	
	TSDT	203.3351	203.3351	203.3351	203.3351	

Table V. $\bar{\sigma}_{xx}$ and $\bar{\sigma}_{xy}$ for a FGM plate under a mechanical sinusoidal load

	b/h	Theory	$z = 0$	$z = 0.10$	$z = 0.55$	$z = 1$
$\bar{\sigma}_{xx}$	4	Asymt	-3.3160	-2.5356	0.4480	3.0261
		LWT	-3.3083	-2.5130	0.4433	3.0053
		ITSdT	-3.3461	-2.5221	0.4346	3.0369
		TSDT	-3.6993	-2.7671	0.4240	3.0077
	10	Asymt	-20.1785	-15.8909	2.5802	17.5444
		LWT	-19.9982	-15.7511	2.5543	17.3528
		ITSdT	-20.0257	-15.7892	2.5339	17.3880
		TSDT	-21.9654	-17.1980	2.7978	17.9215
50	Asymt	-501.3377	-397.1274	63.1239	433.1855	
	LWT	-491.0855	-389.2815	61.7737	423.8000	
	ITSdT	-495.9296	-394.5071	62.1434	428.1819	
	TSDT	-543.8268	-429.5075	70.6240	444.0081	
$\bar{\sigma}_{xy}$	4	Asymt	1.9092	1.4676	-0.1435	-1.7035
		LWT	1.8966	1.4589	-0.1419	-1.6902
		ITSdT	1.9002	1.4612	-0.1433	-1.6935
		TSDT	1.7131	1.2837	-0.2067	-1.6244
	10	Asymt	11.6179	9.1627	-1.3994	-10.7763
		LWT	11.5313	9.0951	-1.3872	-10.6937
		ITSdT	11.5468	9.1077	-1.3783	-10.6989
		TSDT	10.1431	7.9537	-1.3607	-9.6530
50	Asymt	288.6490	228.8283	-37.0743	-270.5195	
	LWT	285.2624	226.1397	-36.6048	-267.3381	
	ITSdT	286.7806	227.3817	-36.4581	-268.4743	
	TSDT	250.9844	198.5238	-34.3347	-239.0282	

where $P = \alpha^* \hat{T}_0^+$, with $\alpha^* = 10^{-6}$ 1/K for the applied thermal load \hat{T}^+ and $P = \hat{q}_0^+ / c^*$, with $c^* = 10^{10}$ N/m² for the applied mechanical load \hat{q}^+ .

a. Mechanical Load

Tables IV, V and VI show the results of the non-dimensionalized quantities given by Eq. 3.8, obtained for the FGM plate under the sinusoidal mechanical load specified in Eq. 3.7. For LWT, we employed a 9 node Lagrangian element and for TSDT and ITSDT a 4 node element with Hermite and Lagrangian interpolation functions, as specified in the previous chapter. As we can observe in Table IV and V, ITSDT provides results that are in good agreement with LWT and the asymptotic approach used in [33] (Asysmt). This fact represents an important improvement with respect to TSDT, specially for displacements and the in-plane stresses.

It is important to point out that in the case where b/h is equal to 10 (thick plate) or 50 (thin plate) the difference between the solution obtained with TSDT and the one obtained with LWT or Asymt is greater than 10%. Unlike the composite laminates, where the Poisson's effect is very small over the thickness, in the case of FGM the isotropy of the material causes the displacement field to vary freely in the z direction. Accordingly, the ITSDT which is proposed in this work has the advantage of describing this mode of deformation and, therefore, better results can be obtained.

Even though in-plane stresses are accurately calculated using ITSDT, the numerical approximation of the out of plane stresses does not present the same behavior. As we can observe in Table VI, values of σ_{yz} do not experience any significant improvement with respect to TSDT and values of σ_{zz} are poorly computed using ITSDT.

Table VI. $\bar{\sigma}_{yz}$ and $\bar{\sigma}_{zz}$ for a FGM plate under a sinusoidal mechanical load

	b/h	Theory	$z = 0$	$z = 0.10$	$z = 0.55$	$z = 1$
$\bar{\sigma}_{yz}$	4	Asymt	-0.0059	-0.3669	-0.9344	0.0000
		LWT	-0.0441	-0.3441	-0.9290	-0.0430
		ITSdT	-0.0108	-0.3589	-0.9187	-0.0234
		TSDT	-0.0025	-0.3535	-0.9234	-0.0022
	10	Asymt	-0.0143	-0.9057	-2.3535	0.0000
		LWT	-0.0960	-0.8521	-2.3400	-0.0906
		ITSdT	-0.0038	-0.8887	-2.3129	-0.0233
		TSDT	-0.0062	-0.8875	-2.3187	-0.0056
	50	Asymt	-0.0709	-4.5128	-11.7847	0.0000
		LWT	-0.3373	-4.1819	-11.7795	-0.3252
		ITSdT	0.0080	-4.4304	-11.5799	-0.0913
		TSDT	-0.0309	-4.4413	-11.6030	-0.0281
$\bar{\sigma}_{zz}$	4	Asymt	0.0000	0.0310	0.5866	1.0000
		LWT	-0.0447	0.0509	0.5814	1.0091
		ITSdT	-0.1459	0.0205	0.5560	1.1115
		TSDT	0.0000	0.0000	0.0000	0.0000
	10	Asymt	0.0000	0.0304	0.5887	1.0000
		LWT	-0.0156	0.0564	0.5789	0.9055
		ITSdT	0.0619	0.0336	0.5864	0.9112
		TSDT	0.0000	0.0000	0.0000	0.0000
	50	Asymt	0.0000	0.0303	0.5888	1.0000
		LWT	2.3464	1.5803	0.2311	-3.0687
		ITSdT	5.9971	0.4328	1.4017	-4.8561
		TSDT	0.0000	0.0000	0.0000	0.0000

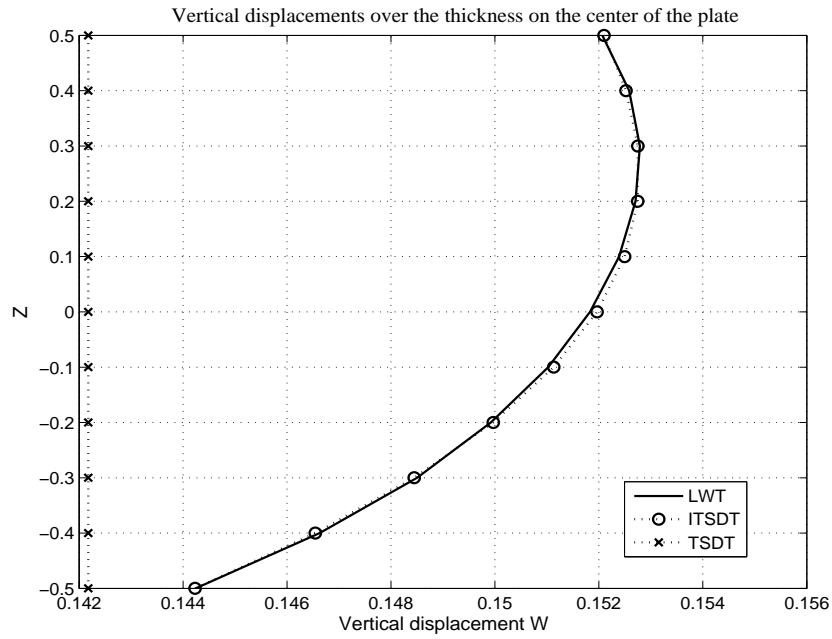


Fig. 12. \bar{w} through thickness for a FGM plate under mechanical load

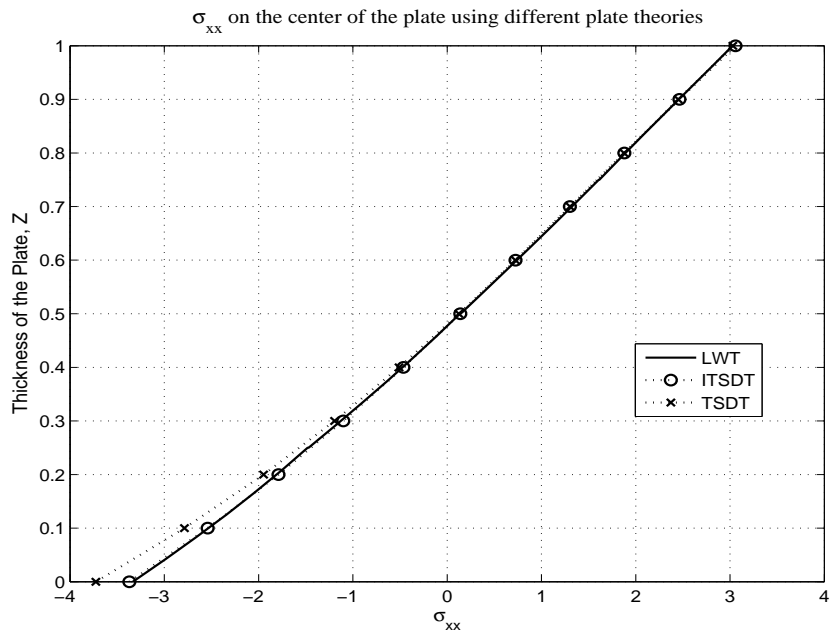


Fig. 13. $\bar{\sigma}_{xx}$ through thickness for a FGM plate under mechanical load

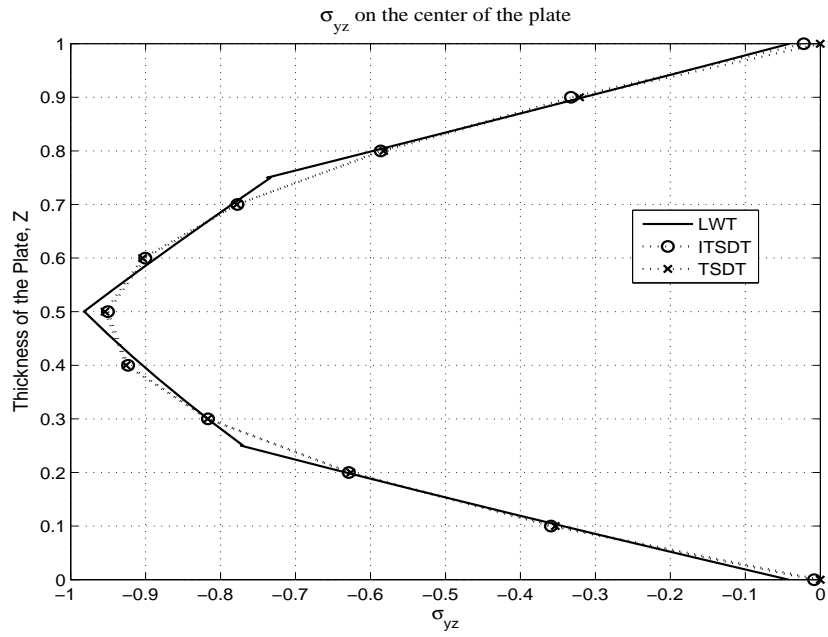


Fig. 14. $\bar{\sigma}_{yz}$ through thickness for a FGM plate under mechanical load

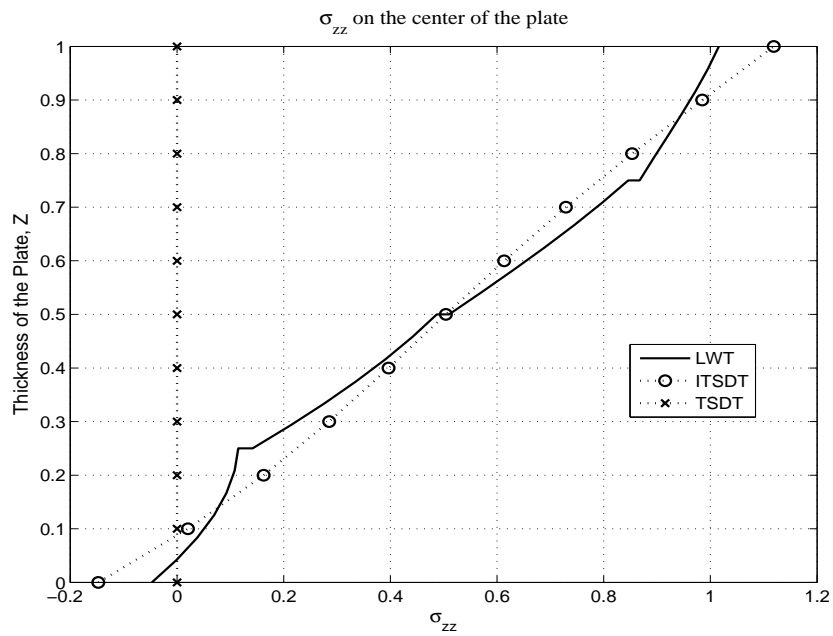


Fig. 15. $\bar{\sigma}_{zz}$ through thickness for a FGM plate under mechanical load

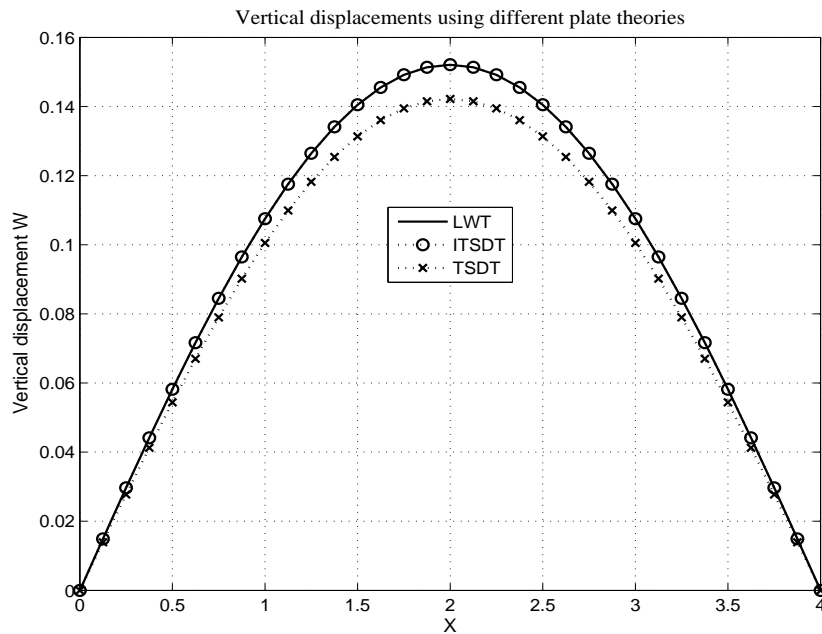


Fig. 16. Central deflection along FGM plate length under mechanical load

A graphical comparison between LWT, ITSDT and TSDT is shown in Figures 12 to 16 for the case where $b/h = 4$. Here it is important to point out that for vertical displacements in FGM plates the ITSDT represents a substantial improvement with respect to TSDT. For instance, by examining Fig. 16, we can easily observe that the ITSDT accurately predicts the profile of the FGM plate along its length under an applied sinusoidal mechanical load.

b. Thermal Load

Tables VII, VIII and IX show the results of the non-dimensionalized quantities (Eq. 3.8) obtained for the FGM plate under the thermal load specified in Eq. 3.7. In this case, all the FEM elements to be compared are going to be 9 node elements. In the case of LWT, displacement and thermal variables in all the nodes are presented. Therefore, quadratic Lagrange interpolation functions can be used for the elastic and

thermal field. In addition to this, the thickness coordinate is discretized using four layers with quadratic interpolation functions. In the case of TSDT and ITSDT only 4 nodes (the one on the corners) contain elastic variables; meanwhile, the thermal field is presented in all the 9 nodes. Consequently, quadratic Lagrange interpolation functions are used to approximate the thermal field. An important remark is that the equivalent single layer theory for the temperature described in the previous chapter was employed. In this case, ITSDT gives good results for the vertical displacement \bar{w} only, and for \bar{u} the results are better than provided by TSDT; however this results are not as good when a mechanical load is applied. For this reason, the results of the non-dimensional stresses presents the same problem. It is important to point out that for a refined mesh (8×8 elements) the approximations are better, which means that in the case of thermal field a better discretization in the plane domain is required to take into account all the deformation mechanisms produced by this field.

Figures 17 to 21 represent comparisons of the non-dimensionalized values given in Eq. 3.8 in the case where $b/h = 4$. Fig. 21 clearly shows that TSDT underpredicts the variation of the vertical displacement along the plate length. Conversely, ITSDT provides results that are in a very good agreement with LWT.

Table VII. \bar{u} and \bar{w} for a FGM plate under a sinusoidal thermal field

	b/h	Theory	$z = 0$	$z = 0.10$	$z = 0.55$	$z = 1$
\bar{u}	4	Asymt	-0.0826	0.0579	0.7213	1.5819
		LWT	-0.0832	0.0577	0.7226	1.5827
		ITSdT	-0.0736	0.0685	0.7333	1.5992
		TSDT	-0.1242	0.0482	0.8218	1.5936
	10	Asymt	-0.0856	0.0783	0.8221	1.5986
		LWT	-0.0870	0.0780	0.8222	1.6002
		ITSdT	-0.0740	0.0901	0.8344	1.6120
		TSDT	-0.0803	0.0974	0.8969	1.6940
	50	Asymt	-0.0861	0.0828	0.8431	1.6025
		LWT	-0.0896	0.0804	0.8435	1.6063
		ITSdT	-0.0740	0.0949	0.8554	1.6150
		TSDT	-0.0709	0.1079	0.9127	1.7149
\bar{w}	4	Asymt	1.7996	1.8122	2.0730	2.8706
		LWT	1.8010	1.8135	2.0765	2.8692
		ITSdT	1.8029	1.8235	2.0746	2.9018
		TSDT	2.1929	2.1929	2.1929	2.1929
	10	Asymt	5.2223	5.2281	5.3500	5.6905
		LWT	5.2195	5.2252	5.3478	5.6858
		ITSdT	5.2176	5.2262	5.3462	5.6985
		TSDT	5.6500	5.6500	5.6500	5.6500
	50	Asymt	26.8826	26.8838	26.9089	26.9779
		LWT	26.7424	26.7434	26.7684	26.8372
		ITSdT	26.8509	26.8526	26.8775	26.9489
		TSDT	28.4229	28.4229	28.4229	28.4229

Table VIII. $\bar{\sigma}_{xx}$ and $\bar{\sigma}_{xy}$ for a FGM plate under a sinusoidal thermal field

	b/h	Theory	$z = 0$	$z = 0.10$	$z = 0.55$	$z = 1$
$\bar{\sigma}_{xx}$	4	Asymt	-5.9945	-8.0400	-21.8798	-92.8964
		LWT	-6.0075	-7.9532	-21.8060	-98.2330
		ITSdT	-3.0586	-8.2351	-22.8373	-102.9315
		TSDT	-13.1914	-12.9434	-20.8879	-108.3721
	10	Asymt	-6.2290	-9.1183	-25.6057	-91.9860
		LWT	-6.0789	-8.9640	-25.4924	-96.6905
		ITSdT	-3.8157	-9.4432	-26.6411	-100.9413
		TSDT	-9.5341	-11.9193	-27.3909	-101.8455
50	Asymt	-6.2662	-9.3405	-26.4026	-91.7765	
	LWT	-5.4771	-8.6616	-26.3668	-96.8538	
	ITSdT	-3.9772	-9.6895	-27.4601	-100.5130	
	TSDT	-8.7431	-11.6983	-28.7703	-100.4870	
$\bar{\sigma}_{xy}$	4	Asymt	3.4017	-2.3809	-28.6435	-57.7352
		LWT	3.3827	-2.3584	-28.4413	-57.3277
		ITSdT	3.9075	-1.9011	-27.9890	-56.8496
		TSDT	6.0700	-0.9676	-31.3734	-56.8001
	10	Asymt	3.5263	-3.2212	-32.6431	-58.3462
		LWT	3.4814	-3.2138	-32.4088	-57.9187
		ITSdT	4.0370	-2.6630	-31.8457	-57.3956
		TSDT	4.3742	-2.8810	-34.2322	-60.3420
50	Asymt	3.5455	-3.4068	-33.4797	-58.4857	
	LWT	3.3570	-3.5120	-33.2207	-57.9241	
	ITSdT	4.0626	-2.8336	-32.6495	-57.5245	
	TSDT	4.0075	-3.2922	-34.8330	-61.0792	

Table IX. $\bar{\sigma}_{yz}$ and $\bar{\sigma}_{zz}$ for a FGM plate under a sinusoidal thermal field

	b/h	Theory	$z = 0$	$z = 0.10$	$z = 0.55$	$z = 1$
$\bar{\sigma}_{yz}$	4	Asymt	0.0105	0.5982	0.1115	0.0000
		LWT	-0.3127	-0.4622	-0.1297	0.2385
		ITSDDT	0.4569	-0.4974	-0.0759	1.3002
		TSDT	-0.0004	-0.0593	-0.1549	-0.0004
	10	Asymt	-0.0044	0.2492	0.0318	0.0000
		LWT	-0.1330	-0.1837	-0.0395	0.1019
		ITSDDT	0.0821	-0.2222	-0.0222	0.5741
		TSDT	-0.0001	-0.0197	-0.0513	-0.0001
	50	Asymt	0.0009	0.0501	0.0058	0.0000
		LWT	-0.0115	-0.0284	-0.0147	0.0336
		ITSDDT	0.0122	-0.0453	-0.0041	0.1169
		TSDT	-0.0000	-0.0038	-0.0098	-0.0000
$\bar{\sigma}_{zz}$	4	Asymt	0.0000	0.0523	0.5658	0.0000
		LWT	-0.2033	0.1604	0.4037	-19.3543
		ITSDDT	10.3987	1.5912	0.1162	-32.3557
		TSDT	0.0000	0.0000	0.0000	0.0000
	10	Asymt	0.0000	0.0087	0.0925	0.0000
		LWT	-0.0667	0.0899	-0.0379	-17.0183
		ITSDDT	8.8328	1.3794	-0.3428	-28.3272
		TSDT	0.0000	0.0000	0.0000	0.0000
	50	Asymt	0.0000	0.0004	0.0037	0.0000
		LWT	0.1418	0.2336	-0.1481	-16.6697
		ITSDDT	8.4886	1.3354	-0.4328	-27.5219
		TSDT	0.0000	0.0000	0.0000	0.0000

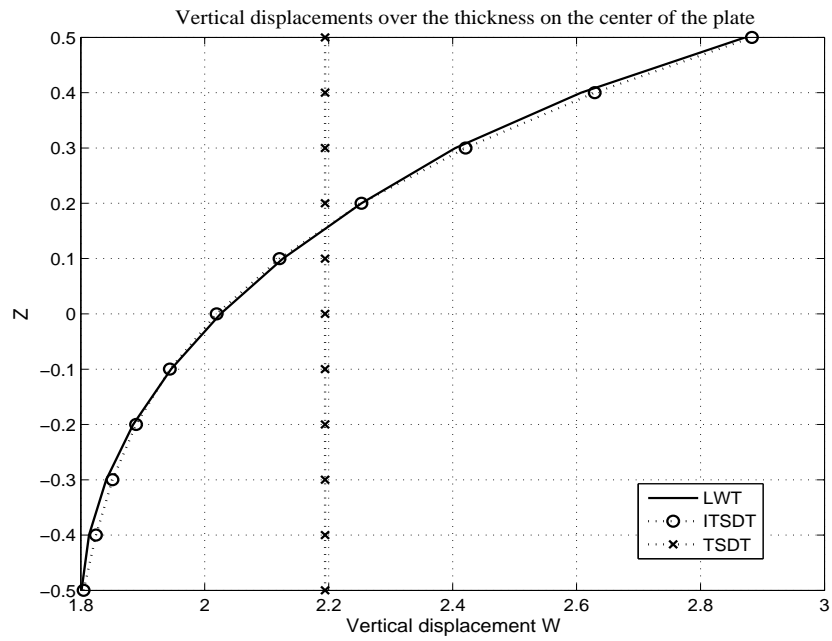


Fig. 17. \bar{w} through thickness for a FGM plate under thermal load

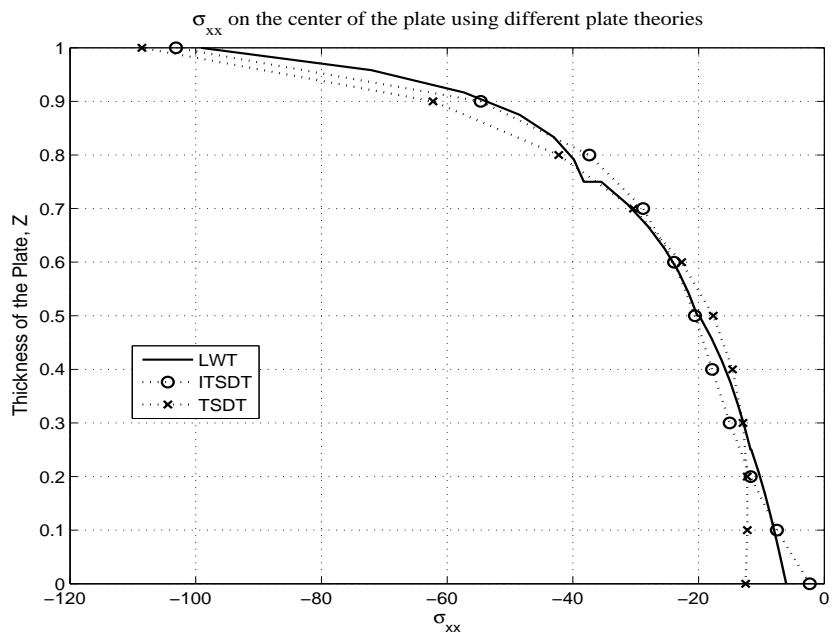


Fig. 18. $\bar{\sigma}_{xx}$ through thickness for a FGM plate under thermal load

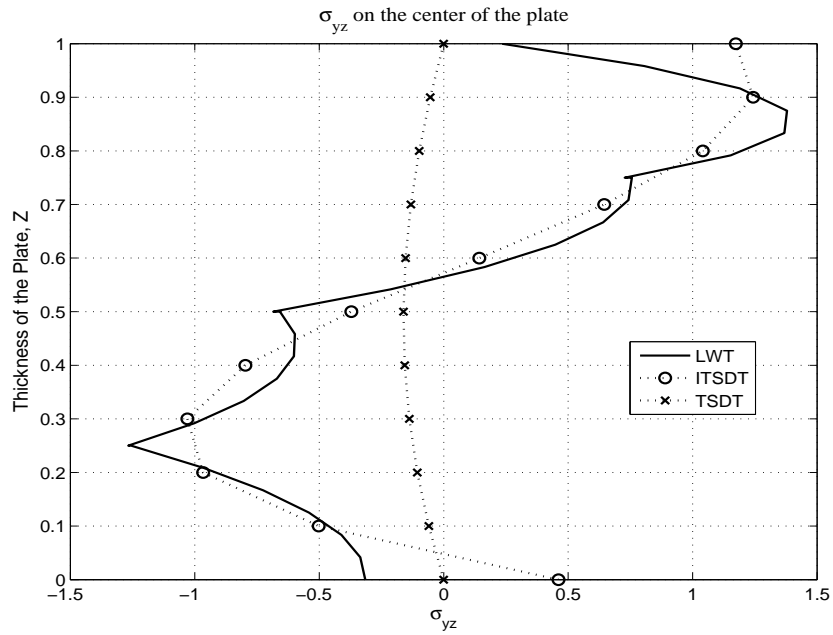


Fig. 19. $\bar{\sigma}_{yz}$ through thickness for a FGM plate under thermal load

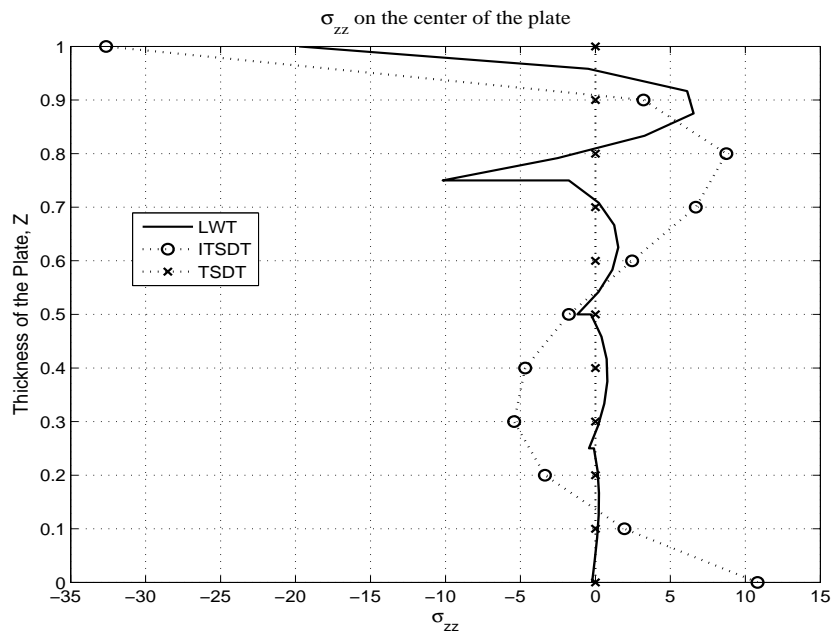


Fig. 20. $\bar{\sigma}_{zz}$ through thickness for a FGM plate under thermal load

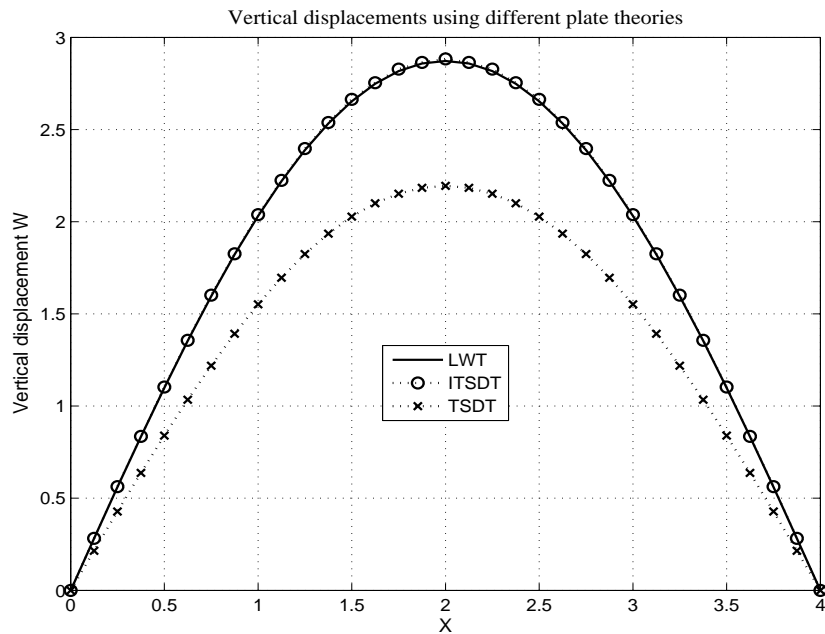


Fig. 21. Central deflection along the FGM plate length under thermal load

2. Smart FGM Plate

In this section, we are going to analyze the benchmark proposed in [33] that consists of an FGM plate with a piezoelectric layer mounted in its bottom surface. Here 90% of the thickness corresponds to the FGM and the 10% to the piezoelectric. The applied mechanical and thermal loads are the same as in the case of pure FGM plate; however due to the presence of the piezoelectric layer, a case where an electrical field is also imposed over the structure needs to be included in the analysis. Then, considering again the quarter plate as the computational domain

$$V^- = \hat{V}^- \cos\left(\frac{\pi x}{a}\right) \cos\left(\frac{\pi y}{b}\right) \quad (3.9)$$

where V^- is the voltage applied to the bottom part of the piezoelectric layer. Moreover, the voltage between the metal surface of the FGM and the piezoelectric is zero. Therefore, the same nondimensionalization applies but in the case of an applied voltage $P = \hat{V}^- (e^*/ac^*)$ where $e^* = 10 \text{ C/m}^2$.

a. Mechanical Load

Tables X, XI and XII show the results using of the smart plate under a sinusoidal mechanical load, specified in Eq. 3.7. As it can be observed the ITSDT provides numerical results that are in good agreement with the ones provided by the LWT and Asymt in the case of displacements and σ_{xy} . For σ_{xx} the results are not as good as we expected, but they are better than the ones provided by TSDT.

The previous observations can be easily confirmed in Figures 22 to 25. Moreover, if we want to make a comparison about the global behavior between ITSDT and LWT, we should notice that Fig 26 clearly shows that for a smart FGM plate, ITSDT represents a good alternative to LWT.

Table X. \bar{u} and \bar{w} for a FGM plate under a sinusoidal mechanical load

b/h	Theory	$z = 0$	$z = 0.10^-$	$z = 0.10^+$	$z = 0.55$	$z = 1$	
\bar{u}	4	Asymt	-0.0582	-0.0466	-0.0463	0.0017	0.0521
		LWT	-0.0583	-0.0466	-0.0463	0.0018	0.0521
		ITSdT	-0.0581	-0.0457	-0.0455	0.0018	0.0517
		TSDT	-0.0516	-0.0394	-0.0392	0.0043	0.0476
	10	Asymt	-0.3551	-0.2871	-0.2855	0.0221	0.3296
		LWT	-0.3557	-0.2874	-0.2858	0.0221	0.3302
		ITSdT	-0.3531	-0.2846	-0.2830	0.0227	0.3289
		TSDT	-0.3010	-0.2406	-0.2392	0.0262	0.2904
50	Asymt	-8.8257	-7.1536	-7.1129	0.5982	8.2722	
	LWT	-8.8629	-7.1811	-7.1414	0.6010	8.3105	
	ITSdT	-8.7701	-7.1037	-7.0644	0.6164	8.2615	
	TSDT	-7.4239	-5.9894	-5.9556	0.6524	7.2281	
4	Asymt	0.1642	0.1689	0.1690	0.1758	0.1752	
	LWT	0.1641	0.1688	0.1689	0.1757	0.1751	
	ITSdT	0.1639	0.1674	0.1675	0.1752	0.1744	
	TSDT	0.1588	0.1588	0.1588	0.1588	0.1588	
\bar{w}	10	Asymt	2.2476	2.2591	2.2593	2.2732	2.2594
		LWT	2.2459	2.2575	2.2577	2.2719	2.2580
		ITSdT	2.2391	2.2482	2.2484	2.2641	2.2498
		TSDT	1.9671	1.9671	1.9671	1.9671	1.9671
50	Asymt	273.0874	273.1445	273.1453	273.2124	273.1322	
	LWT	271.6263	271.6814	271.6823	271.7478	271.6706	
	ITSdT	271.9821	272.0282	272.0292	272.1044	272.0215	
	TSDT	234.0888	234.0888	234.0888	234.0888	234.0888	

Table XI. $\bar{\sigma}_{xx}$ and $\bar{\sigma}_{xy}$ for a FGM plate under a sinusoidal mechanical load

b/h	Theory	$z = 0$	$z = 0.10^-$	$z = 0.10^+$	$z = 0.55$	$z = 1$	
$\bar{\sigma}_{xx}$	4	Asymt	-1.7730	-1.3089	-3.3053	0.3123	3.3436
		LWT	-1.7075	-1.3582	-3.3038	0.3136	3.3191
		ITSdT	-1.9811	-1.5540	-3.0849	0.2674	3.3748
		TSDT	-2.4775	-1.8972	-3.4935	0.3439	3.2014
	10	Asymt	-10.7825	-8.1427	-20.4145	1.6974	19.5563
		LWT	-10.3641	-8.3784	-20.2511	1.7003	19.3215
		ITSdT	-11.6796	-9.5971	-19.0977	1.4648	19.5786
		TSDT	-14.4239	-11.5450	-21.2787	2.0965	19.4955
50	Asymt	-267.8764	-203.2225	-508.8082	40.9274	483.5281	
	LWT	-254.1364	-206.0629	-498.4310	40.4350	472.2888	
	ITSdT	-288.4157	-239.1834	-476.1835	35.3327	483.2222	
	TSDT	-355.7228	-287.1892	-529.4160	52.1706	485.0286	
$\bar{\sigma}_{xy}$	4	Asymt	0.8265	0.6613	1.9064	-0.0693	-1.9017
		LWT	0.8212	0.6565	1.8939	-0.0701	-1.8860
		ITSdT	0.8232	0.6487	1.8708	-0.0681	-1.8779
		TSDT	0.7330	0.5615	1.6180	-0.1649	-1.7282
	10	Asymt	5.0401	4.0759	11.7571	-0.8819	-12.0324
		LWT	5.0022	4.0446	11.6697	-0.8757	-11.9397
		ITSdT	4.9900	4.0250	11.6127	-0.8718	-11.8983
		TSDT	4.2565	3.4070	9.8277	-1.0052	-10.5000
50	Asymt	125.2830	101.5479	292.9534	-23.9041	-301.9500	
	LWT	123.7726	100.3203	289.4638	-23.5985	-298.3409	
	ITSdT	123.8836	100.3996	289.6907	-23.6363	-298.6252	
	TSDT	104.9205	84.7067	244.3836	-25.0122	-261.1148	

Table XII. $\bar{\sigma}_{yz}$ and $\bar{\sigma}_{zz}$ for a FGM plate under a sinusoidal mechanical load

	b/h	Theory	$z = 0$	$z = 0.10^-$	$z = 0.10^+$	$z = 0.55$	$z = 1$
$\bar{\sigma}_{yz}$	4	Asymt	-0.0051	-0.1791	-0.1883	-0.9961	0.0000
		LWT	-0.0054	-0.1787	-0.2482	-0.9600	-0.0704
		ITSdT	0.0388	-0.0865	-0.2767	-0.9651	-0.0690
		TSDT	0.0652	-0.0591	-0.1918	-0.9603	-0.1700
	10	Asymt	-0.0124	-0.4403	-0.4631	-2.5087	0.0000
		LWT	-0.0114	-0.4397	-0.5989	-2.4194	-0.1539
		ITSdT	0.1083	-0.2103	-0.6739	-2.4299	-0.1386
		TSDT	0.1636	-0.1485	-0.4815	-2.4115	-0.4269
	50	Asymt	-0.0618	-2.1926	-2.3059	-12.5609	0.0000
		LWT	-0.0047	-2.1822	-2.8771	-12.1747	-0.6257
		ITSdT	0.5541	-1.0443	-3.3466	-12.1656	-0.6673
		TSDT	0.8188	-0.7430	-2.4096	-12.0672	-2.1362
$\bar{\sigma}_{zz}$	4	Asymt	0.0000	0.0151	0.0157	0.5516	1.0000
		LWT	-0.0052	0.0083	-0.0430	0.5517	1.0096
		ITSdT	-0.4702	-0.3587	0.4269	0.4301	1.2503
		TSDT	0.0000	0.0000	0.0000	0.0000	0.0000
	10	Asymt	0.0000	-0.0148	-0.0154	-0.5531	-1.0000
		LWT	0.0123	0.0191	-0.0234	0.5934	0.8327
		ITSdT	-2.2577	-2.1225	2.8865	-0.0580	1.8142
		TSDT	0.0000	0.0000	0.0000	0.0000	0.0000
	50	Asymt	0.0000	0.0147	0.0154	0.5531	1.0000
		LWT	1.8348	1.4469	2.2559	1.5495	-5.3799
		ITSdT	-53.2568	-52.4687	73.1037	-14.0228	17.8514
		TSDT	0.0000	0.0000	0.0000	0.0000	0.0000

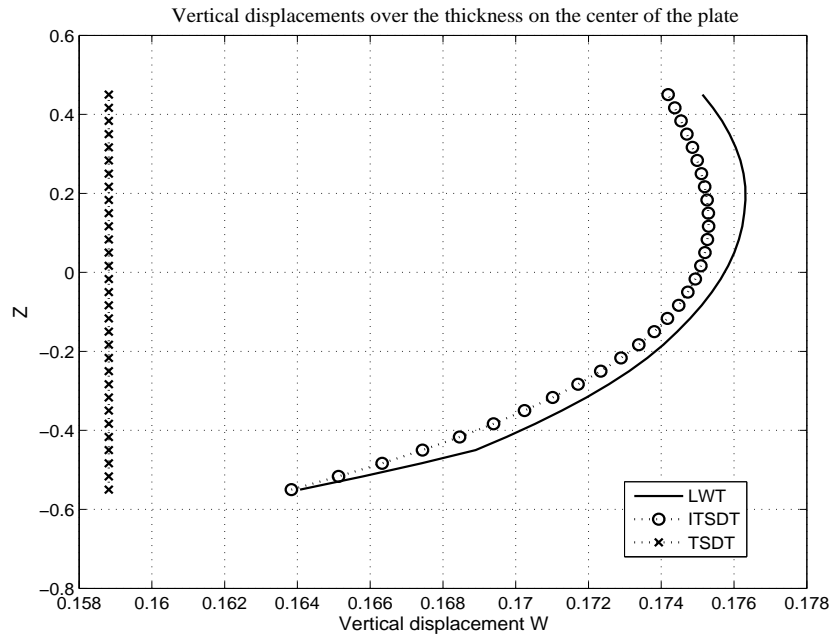


Fig. 22. \bar{w} through thickness for a smart FGM plate under mechanical load

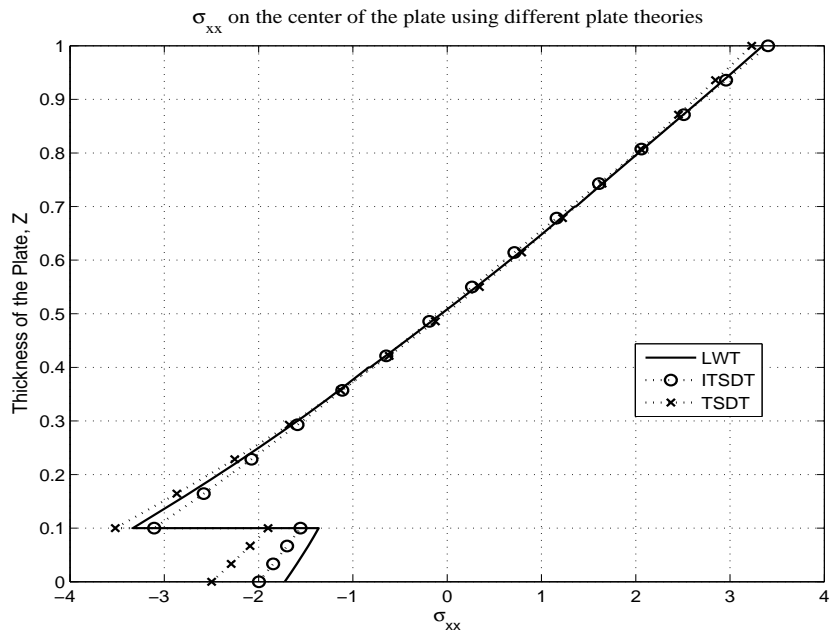


Fig. 23. $\bar{\sigma}_{xx}$ through thickness for a smart FGM plate under mechanical load

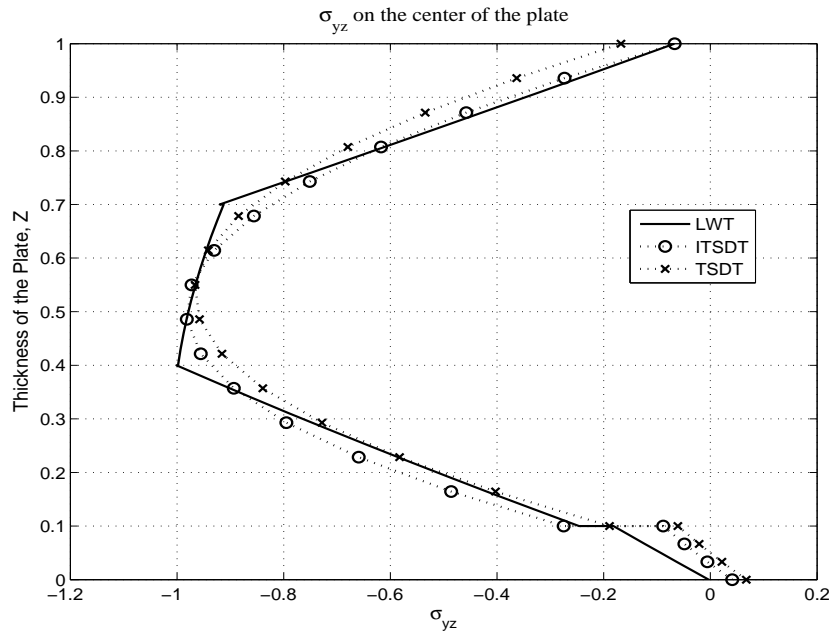


Fig. 24. $\bar{\sigma}_{yz}$ through thickness for a smart FGM plate under mechanical load

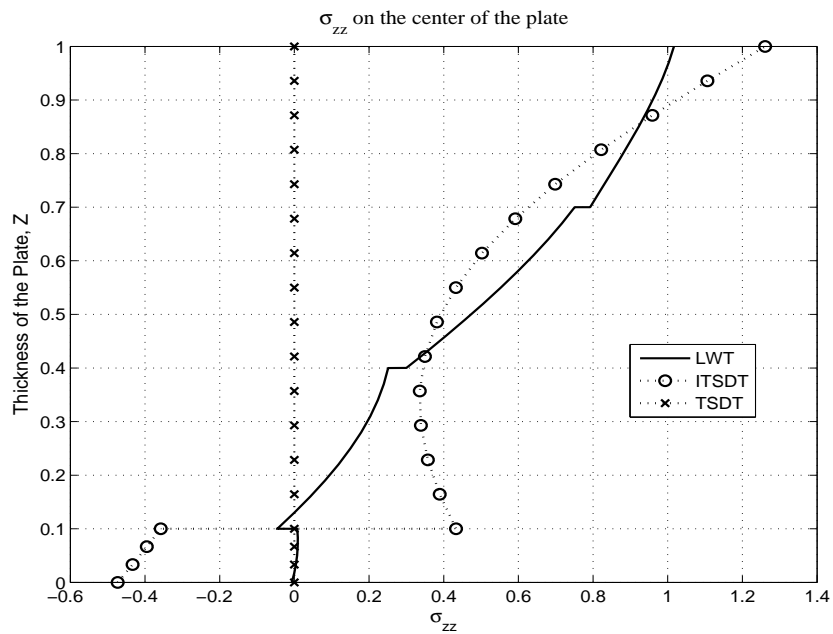


Fig. 25. $\bar{\sigma}_{zz}$ through thickness for a smart FGM plate under mechanical load

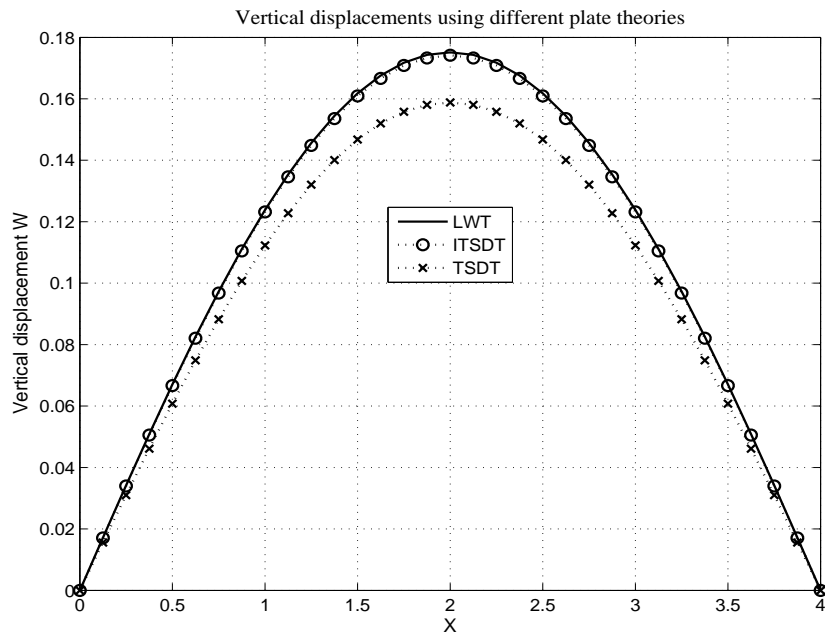


Fig. 26. Central deflection along the smart FGM plate length under mechanical load

b. Thermal Load

Tables XIII to XVIII show the results of the non-dimensionalized quantities (Eq. 3.8) obtained for the smart FGM plate under the sinusoidal thermal load (Eq. 3.7). Here in all the elements the electrical field is included in the 9 nodes using quadratic Lagrangian interpolation for the layerwise electrical model presented in Chapter I. Here we assume one mathematical layer with a quadratic Lagrangian interpolation function for the piezoelectric layer.

Table XIII. \bar{u} for a FGM plate under a sinusoidal thermal field

b/h	Theory	$z = 0$	$z = 0.10^-$	$z = 0.10^+$	$z = 0.55$	$z = 1$
4	Asymt	0.5315	0.6163	0.6182	1.0600	1.7655
	LWT	0.5315	0.6159	0.6179	1.0603	1.7660
	RITSDT	0.5480	0.6318	0.6338	1.0773	1.7912
	ITSDT	0.5073	0.6000	0.6022	1.0714	1.8108
	TSDT	0.4807	0.6094	0.6124	1.2002	1.7852
\bar{u} 10	Asymt	0.8731	0.9664	0.9687	1.4108	1.9051
	LWT	0.8725	0.9660	0.9682	1.4108	1.9060
	RITSDT	0.8945	0.9877	0.9899	1.4336	1.9309
	ITSDT	0.8455	0.9460	0.9484	1.4245	1.9537
	TSDT	0.9212	1.0313	1.0339	1.5403	2.0443
50	Asymt	0.9682	1.0632	1.0655	1.5046	1.9439
	LWT	0.9661	1.0617	1.0639	1.5047	1.9459
	RITSDT	0.9906	1.0859	1.0882	1.5289	1.9699
	ITSDT	0.9391	1.0418	1.0442	1.5188	1.9935
	TSDT	1.0425	1.1471	1.1496	1.6322	2.1125

As we can observe, the ITSDT proposed in this work does not give as good results as it did in the previous cases. This means that ITSDT does not have the capability to represent all the deformation modes presented on the smart FGM plate when a thermal load is applied. In order to obtain better numerical approximation,

Table XIV. \bar{w} for a FGM plate under a sinusoidal thermal field

b/h	Theory	$z = 0$	$z = 0.10^-$	$z = 0.10^+$	$z = 0.55$	$z = 1$
4	Asymt	0.9784	0.9380	0.9408	1.5866	2.5383
	LWT	0.9829	0.9423	0.9431	1.5883	2.5375
	RITSDT	0.9755	0.9343	0.9353	1.5911	2.5755
	ITSDT	0.9847	1.0537	1.0556	1.6555	2.6526
	TSDT	1.6691	1.6691	1.6691	1.6691	1.6691
\bar{w} 10	Asymt	2.9618	2.9354	2.9371	3.3129	3.7651
	LWT	2.9623	2.9356	2.9361	3.3109	3.7618
	RITSDT	2.9405	2.9139	2.9145	3.2991	3.7661
	ITSDT	3.1312	3.1682	3.1692	3.5223	3.9966
	TSDT	3.5594	3.5594	3.5594	3.5594	3.5594
50	Asymt	15.4949	15.4891	15.4895	15.5711	15.6653
	LWT	15.4088	15.4028	15.4028	15.4839	15.5780
	RITSDT	15.3815	15.3756	15.3757	15.4593	15.5567
	ITSDT	16.5727	16.5806	16.5809	16.6577	16.7566
	TSDT	16.8913	16.8913	16.8913	16.8913	16.8913

we improve the ITSDT using the multiple assumed displacement field. In other words, ITSDT plus LWT are going to be used together and as a matter of simplification, we will call this combination RITSDT. For our case, two mathematical layers are going to define the LWT representation. The first one includes only the piezoelectric layer

and the second one the FGM. This strategy represents a very simple improvement to ITSDT model. As a consequence, we can see in Tables from XIII to XVIII, that the RITSDT produces much better results than ITSDT. It is important to point out that the performance of TSDT is poor in this case. Therefore, several physical fields are required to be analyzed, an enhancement of the ITSDT through the use of a multiple assumed displacement representation can be considered as a good alternative.

Table XV. $\bar{\sigma}_{xx}$ for a FGM plate under a sinusoidal thermal field

b/h	Theory	$z = 0$	$z = 0.10^-$	$z = 0.10^+$	$z = 0.55$	$z = 1$
4	Asymt	23.5636	6.6870	-40.4570	-42.0761	-82.0121
	LWT	23.4371	6.6777	-40.3525	-41.5123	-87.4762
	RITSDT	20.7680	7.9268	-38.6207	-43.9788	-90.4650
	ITSDT	38.5499	31.0401	-57.9065	-40.9614	-93.9901
	TSDT	25.1560	15.5195	-53.6431	-42.8874	-96.6527
$\bar{\sigma}_{xx}$ 10	Asymt	37.7171	11.2643	-57.6124	-59.8947	-74.1416
	LWT	37.4955	11.2128	-56.8820	-59.4867	-77.6610
	RITSDT	32.9166	14.1826	-56.6791	-61.9819	-80.7597
	ITSDT	58.9114	47.6475	-84.0623	-57.6041	-86.2699
	TSDT	47.7404	29.1542	-69.5235	-66.4396	-80.3779
50	Asymt	41.6410	12.5411	-62.2834	-64.7537	-71.9510
	LWT	41.5770	12.6261	-61.0617	-64.4223	-75.2473
	RITSDT	36.2870	15.9043	-61.5870	-66.8959	-78.1236
	ITSDT	64.5426	52.2434	-91.1896	-62.1431	-84.1927
	TSDT	53.9628	32.8982	-73.8904	-72.8049	-76.0998

Table XVI. $\bar{\sigma}_{xy}$ for a FGM plate under a sinusoidal thermal field

b/h	Theory	$z = 0$	$z = 0.10^-$	$z = 0.10^+$	$z = 0.55$	$z = 1$
4	Asymt	-7.5443	-8.7488	-25.4627	-42.3551	-64.4453
	LWT	-7.4949	-8.6854	-25.2825	-42.0676	-63.9894
	RITSDT	-7.2702	-8.4453	-24.5830	-41.2695	-63.0823
	ITSDT	-6.7114	-8.0072	-23.3202	-41.0431	-63.7829
	TSDT	-6.2555	-8.0577	-23.5014	-45.9863	-63.0837
$\bar{\sigma}_{xy}$ 10	Asymt	-12.3945	-13.7188	-39.8957	-56.3744	-69.5407
	LWT	-12.3153	-13.6281	-39.6306	-55.9806	-69.0404
	RITSDT	-11.9918	-13.2937	-38.6592	-54.9269	-67.9629
	ITSDT	-11.3078	-12.7119	-36.9783	-54.5758	-68.7981
	TSDT	-12.3179	-13.8553	-40.3046	-59.0158	-72.0105
50	Asymt	-13.7432	-15.0923	-43.8842	-60.1237	-70.9556
	LWT	-13.6856	-15.0182	-43.6648	-59.6964	-70.3707
	RITSDT	-13.3014	-14.6316	-42.5430	-58.5792	-69.3234
	ITSDT	-12.5796	-14.0135	-40.7568	-58.1918	-70.1922
	TSDT	-13.9886	-15.4478	-44.9199	-62.5366	-74.3568

Table XVII. $\bar{\sigma}_{yz}$ for a FGM plate under a sinusoidal thermal field

b/h	Theory	$z = 0$	$z = 0.10^-$	$z = 0.10^+$	$z = 0.55$	$z = 1$
4	Asymt	0.0611	1.8244	1.7979	-0.8831	0.0000
	LWT	0.0502	1.8173	1.4963	-0.6810	0.0445
	RITSDT	0.6681	1.1361	2.2972	-0.7462	0.7311
	ITSDT	1.5336	0.9500	2.8887	-1.2882	2.0048
	TSDT	0.0356	-0.0224	-0.0888	-0.4445	-0.0787
$\bar{\sigma}_{yz}$ 10	Asymt	0.0394	1.1792	1.1667	-0.4858	0.0000
	LWT	0.0462	1.1844	1.0584	-0.4088	-0.0253
	RITSDT	0.3807	0.7853	1.2900	-0.3976	0.2552
	ITSDT	0.8039	0.5797	1.7722	-0.7458	1.0503
	TSDT	0.0238	-0.0151	-0.0596	-0.2984	-0.0528
50	Asymt	0.0087	0.2608	0.2582	-0.1045	0.0000
	LWT	0.0139	0.2631	0.2434	-0.0928	-0.0012
	RITSDT	0.0827	0.1755	0.2793	-0.0851	0.0485
	ITSDT	0.1716	0.1272	0.3893	-0.1620	0.2233
	TSDT	0.0053	-0.0034	-0.0133	-0.0664	-0.0118

Table XVIII. $\bar{\sigma}_{zz}$ for a FGM plate under a sinusoidal thermal field

b/h	Theory	$z = 0$	$z = 0.10^-$	$z = 0.10^+$	$z = 0.55$	$z = 1$
4	Asymt	-0.0002	-0.1634	-0.1697	-0.1666	-0.0004
	LWT	0.0691	-0.0895	-0.6744	0.5545	-19.4763
	RITSDT	-5.0001	4.1314	7.1908	-2.5995	-24.4099
	ITSDT	25.8594	46.7911	-39.1529	7.0664	-39.9322
	TSDT	0.0000	0.0000	0.0000	0.0000	0.0000
$\bar{\sigma}_{zz}$ 10	Asymt	-0.0001	-0.0422	-0.0439	-0.0908	-0.0001
	LWT	0.0366	-0.0117	0.6767	-0.1341	-12.8232
	RITSDT	-9.2093	8.5501	5.3130	-2.1380	-16.9366
	ITSDT	35.4588	70.0983	-61.0740	11.9986	-39.7650
	TSDT	0.0000	0.0000	0.0000	0.0000	0.0000
50	Asymt	0.0000	-0.0019	-0.0019	-0.0044	0.0000
	LWT	0.1004	0.0760	1.1669	-0.2787	-11.1993
	RITSDT	-10.3488	9.7440	4.8633	-1.9657	-15.0973
	ITSDT	38.1283	76.5251	-67.0596	13.4122	-39.9601
	TSDT	0.0000	0.0000	0.0000	0.0000	0.0000

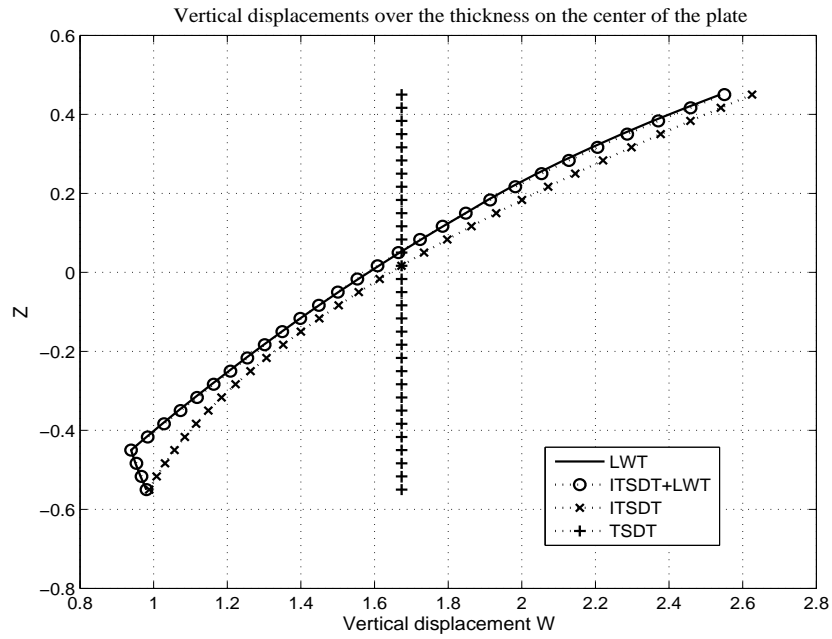


Fig. 27. \bar{w} through thickness for a smart FGM plate under thermal load

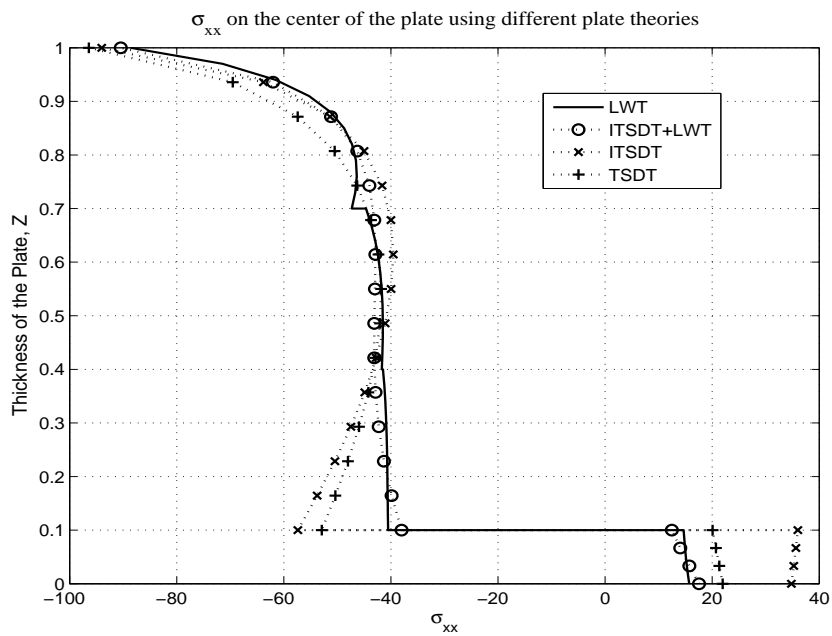


Fig. 28. $\bar{\sigma}_{xx}$ through thickness for a smart FGM plate under thermal load

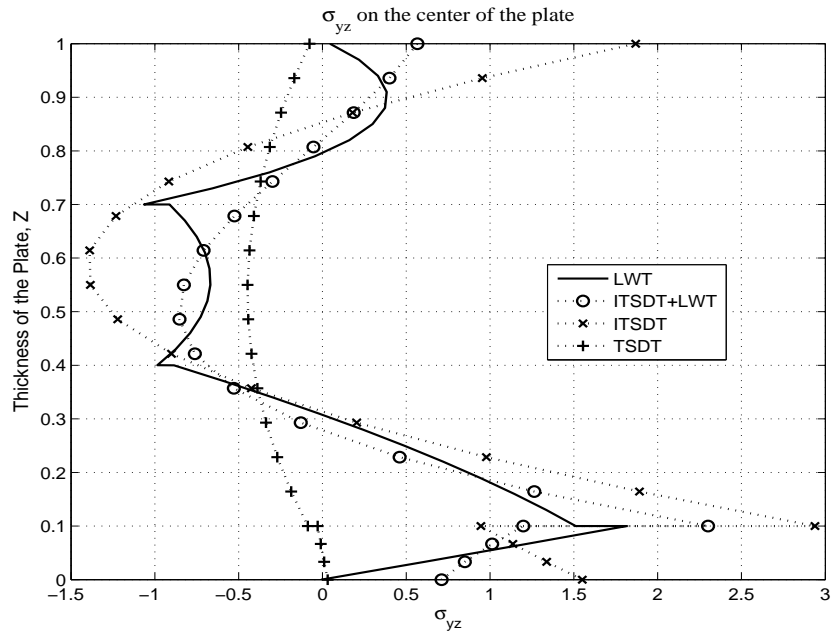


Fig. 29. $\bar{\sigma}_{yz}$ through thickness for a smart FGM plate under thermal load

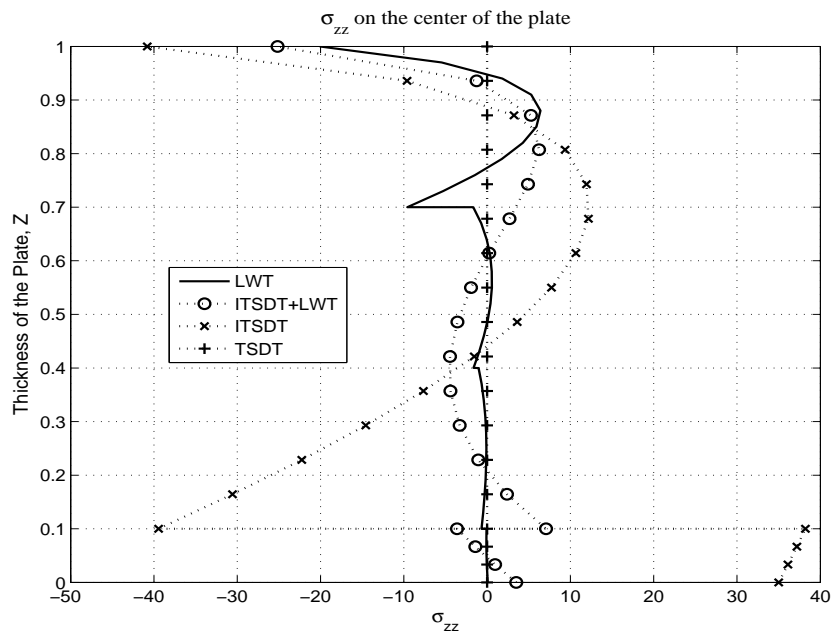


Fig. 30. $\bar{\sigma}_{zz}$ through thickness for a smart FGM plate under thermal load

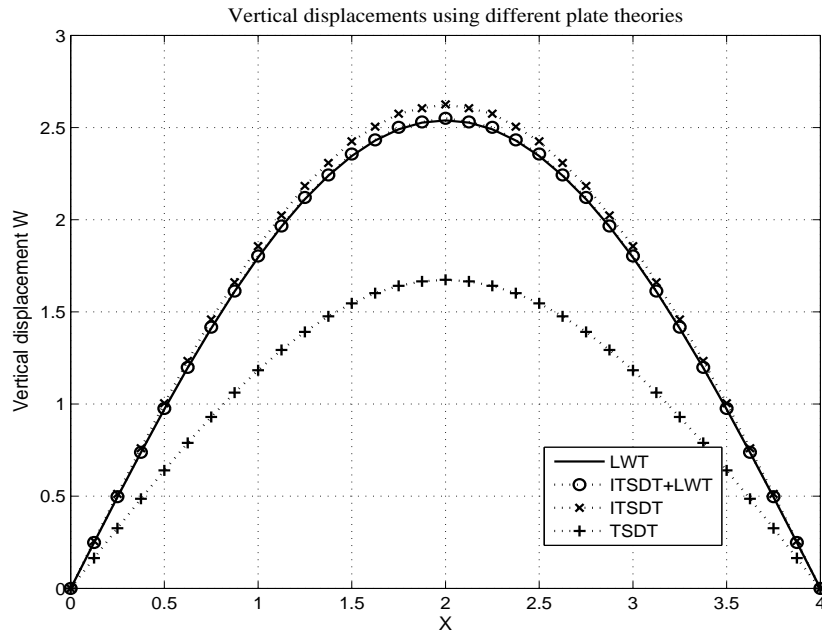


Fig. 31. Central deflection along the smart FGM plate length under thermal load

Figures 27 to 31 represent a graphical comparison among LWT, RITSDT, ITSDT and TSDT. As we can observe, for \bar{w} and $\bar{\sigma}_{xx}$, the results provided by RITSDT are close to those provided by LWT. From Fig. 31, we verify that TSDT does underpredict the values of the vertical displacements along the plate length given by LWT. Conversely, ITSDT slightly overpredicts the results, but RITSDT provides excellent results in the case of vertical displacement when a sinusoidal thermal field is imposed on the smart FGM plate.

c. Electrical Load

Tables XIX to XXIV contains the numerical values of the nondimensionalized quantities defined in Eq. 3.8 when the voltage V^- is applied to the bottom surface of the piezoelectric layer. Likewise the thermal case, RITSDT is used to describe the displacement and the stresses over the smart FGM Plate. These results are

compared with those obtained employing LWT and Asymt and we can conclude that they represent a very reasonable approximation as in the previous case where the effects caused by the thermal field were tested.

Table XIX. \bar{u} for a FGM plate under a sinusoidal electrical field

b/h	Theory	$z = 0$	$z = 0.10^-$	$z = 0.10^+$	$z = 0.55$	$z = 1$
4	Asymt	0.3178	0.2405	0.2393	0.0417	-0.1250
	LWT	0.3144	0.2416	0.2401	0.0417	-0.1249
	RITSDT	0.3179	0.2429	0.2414	0.0421	-0.1247
	ITSDT	0.2679	0.2165	0.2153	0.0347	-0.1053
	TSDT	0.1040	0.0881	0.0877	0.0186	-0.0503
\bar{u} 10	Asymt	0.6993	0.5854	0.5829	0.1212	-0.3262
	LWT	0.6998	0.5860	0.5834	0.1212	-0.3269
	RITSDT	0.7016	0.5877	0.5851	0.1231	-0.3242
	ITSDT	0.6106	0.5169	0.5147	0.1062	-0.2842
	TSDT	0.2572	0.2195	0.2186	0.0465	-0.1247
50	Asymt	3.4088	2.9123	2.9003	0.6217	-1.6430
	LWT	3.4194	2.9202	2.9084	0.6209	-1.6540
	RITSDT	3.4173	2.9210	2.9093	0.6319	-1.6319
	ITSDT	2.9961	2.5613	2.5511	0.5492	-1.4396
	TSDT	1.2833	1.0969	1.0925	0.2327	-0.6228

Table XX. \bar{w} for a FGM plate under a sinusoidal electrical field

b/h	Theory	$z = 0$	$z = 0.10^-$	$z = 0.10^+$	$z = 0.55$	$z = 1$
4	Asymt	-0.3125	-0.5069	-0.5072	-0.5367	-0.5259
	LWT	-0.3090	-0.5038	-0.5063	-0.5360	-0.5252
	RITSDT	-0.3104	-0.5094	-0.5120	-0.5422	-0.5306
	ITSDT	-0.3046	-0.3903	-0.3920	-0.4796	-0.4550
	TSDT	-0.2078	-0.2078	-0.2078	-0.2078	-0.2078
\bar{w} 10	Asymt	-3.0163	-3.2090	-3.2093	-3.2444	-3.2350
	LWT	-3.0106	-3.2034	-3.2059	-3.2414	-3.2320
	RITSDT	-3.0150	-3.2126	-3.2152	-3.2511	-3.2415
	ITSDT	-2.6812	-2.7663	-2.7680	-2.8598	-2.8373
	TSDT	-1.2303	-1.2303	-1.2303	-1.2303	-1.2303
50	Asymt	-80.3362	-80.5285	-80.5288	-80.5649	-80.5559
	LWT	-79.8921	-80.0839	-80.0864	-80.1222	-80.1143
	RITSDT	-80.3746	-80.5719	-80.5745	-80.6114	-80.6023
	ITSDT	-70.6601	-70.7451	-70.7467	-70.8393	-70.8173
	TSDT	-30.4440	-30.4440	-30.4440	-30.4440	-30.4440

Table XXI. σ_{xx} for a FGM plate under a sinusoidal electrical field

b/h	Theory	$z = 0$	$z = 0.10^-$	$z = 0.10^+$	$z = 0.55$	$z = 1$
4	Asymt	-54.8304	-57.0406	17.2404	3.1287	-7.3023
	LWT	-54.4515	-56.6094	17.2361	3.0787	-7.2286
	RITSDT	-54.0295	-56.9420	17.2012	3.0574	-7.4326
	ITSDT	-36.2229	-32.8598	-2.0938	6.0924	-11.1949
	TSDT	-23.7552	-24.3741	7.7315	1.4847	-3.4379
σ_{xx} 10	Asymt	-139.4800	-143.5705	41.7452	8.3715	-19.0525
	LWT	-138.5564	-142.5830	41.4256	8.2887	-18.7735
	RITSDT	-138.3935	-142.7755	41.2498	8.1459	-19.0613
	ITSDT	-92.5422	-83.3348	-7.0343	15.8731	-28.8865
	TSDT	-59.3474	-61.1603	19.2537	3.7188	-8.5254
50	Asymt	-699.6198	-718.7498	207.4769	42.3580	-95.9768
	LWT	-695.9785	-714.6814	203.9491	42.1427	-93.0107
	RITSDT	-695.0320	-714.2683	204.6223	41.1732	-95.7079
	ITSDT	-464.5558	-417.7721	-36.8378	79.9417	-145.2344
	TSDT	-296.6993	-306.0083	96.1998	18.6007	-42.5634

Table XXII. σ_{xy} for a FGM plate under a sinusoidal electrical field

b/h	Theory	$z = 0$	$z = 0.10^-$	$z = 0.10^+$	$z = 0.55$	$z = 1$
4	Asymt	-4.5119	-3.4145	-9.8544	-1.6679	4.5631
	LWT	-4.4565	-3.4016	-9.8038	-1.6523	4.5252
	RITSDT	-4.4203	-3.3742	-9.7300	-1.6118	4.5432
	ITSDT	-3.7282	-3.0117	-8.6920	-1.3288	3.8518
	TSDT	-1.4590	-1.2348	-3.5674	-0.7116	1.8497
σ_{xy} 10	Asymt	-9.9272	-8.3097	-24.0057	-4.8421	11.9052
	LWT	-9.8499	-8.2501	-23.8301	-4.8091	11.8071
	RITSDT	-9.8147	-8.2164	-23.7346	-4.7138	11.9030
	ITSDT	-8.5451	-7.2280	-20.8822	-4.0677	10.4386
	TSDT	-3.6050	-3.0738	-8.8820	-1.7823	4.5852
50	Asymt	-48.3883	-41.3408	-119.4505	-24.8437	59.9721
	LWT	-47.8584	-40.8964	-118.1804	-24.7128	59.0990
	RITSDT	-47.8927	-40.8928	-118.1677	-24.2033	60.0175
	ITSDT	-41.9925	-35.8592	-103.6219	-21.0376	52.9327
	TSDT	-17.9853	-15.3566	-44.3754	-8.9146	22.8892

Table XXIII. σ_{yz} for a FGM plate under a sinusoidal electrical field

	b/h	Theory	$z = 0$	$z = 0.10^-$	$z = 0.10^+$	$z = 0.55$	$z = 1$
σ_{yz}	4	Asymt	-0.0988	-4.0737	-4.0258	1.3475	0.0000
		LWT	0.1843	-3.8111	-3.7823	1.2365	0.2095
		RITSDT	-0.8771	-2.7932	-3.9134	1.2795	0.0251
		ITSDT	1.1592	-1.5695	-4.9228	1.0685	0.7393
		TSDT	3.7646	0.0583	0.0635	0.3179	0.0563
	10	Asymt	-0.1018	-4.1583	-4.1119	1.4021	0.0000
		LWT	-0.0006	-4.0268	-3.8769	1.2807	0.2109
		RITSDT	-1.0710	-2.9869	-4.0425	1.3119	0.0333
		ITSDT	1.0810	-1.6281	-5.1319	1.1126	0.7251
		TSDT	3.7710	0.0645	0.0640	0.3202	0.0567
	50	Asymt	-0.1023	-4.1740	-4.1278	1.4123	0.0000
		LWT	-0.0567	-4.0822	-3.9233	1.3070	0.1734
		RITSDT	-1.1170	-3.0327	-4.0686	1.3195	0.0342
		ITSDT	1.0627	-1.6414	-5.1790	1.1236	0.7200
		TSDT	3.7723	0.0658	0.0641	0.3207	0.0568

Table XXIV. σ_{zz} for a FGM plate under a sinusoidal electrical field

b/h	Theory	$z = 0$	$z = 0.10^-$	$z = 0.10^+$	$z = 0.55$	$z = 1$
4	Asymt	0.0004	0.3245	0.3387	0.8141	0.0008
	LWT	-0.0981	0.2089	0.6478	0.7427	0.0037
	RITSDT	0.9287	-0.5438	0.7425	0.8828	-0.4254
	ITSDT	32.2528	43.5794	-46.8140	10.8902	-16.6512
	TSDT	0.0000	0.0000	0.0000	0.0000	0.0000
σ_{zz} 10	Asymt	0.0002	0.1329	0.1388	0.3425	0.0003
	LWT	-0.0678	0.0680	0.2103	0.2648	0.2345
	RITSDT	0.3475	-0.3080	-0.0555	0.3227	0.0874
	ITSDT	79.3183	108.8708	-117.6503	25.4049	-40.4829
	TSDT	0.0000	0.0000	0.0000	0.0000	0.0000
50	Asymt	0.0000	0.0267	0.0279	0.0691	0.0001
	LWT	-0.5546	-0.4108	-0.7519	-0.1716	1.7492
	RITSDT	-0.0832	-0.5744	-2.0755	-0.1997	1.5312
	ITSDT	395.3747	544.2737	-588.8404	125.2653	-201.3328
	TSDT	0.0000	0.0000	0.0000	0.0000	0.0000

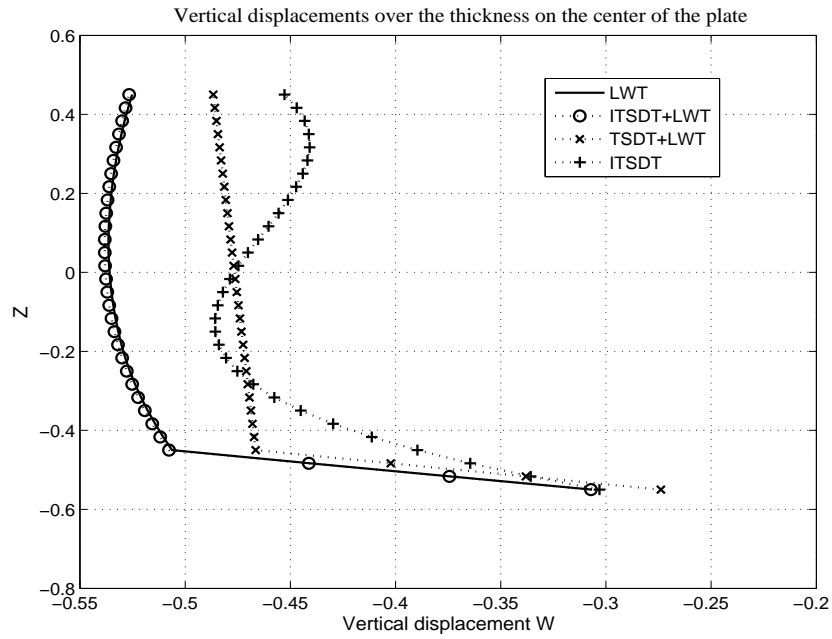


Fig. 32. \bar{w} through thickness for a smart FGM plate under an applied voltage

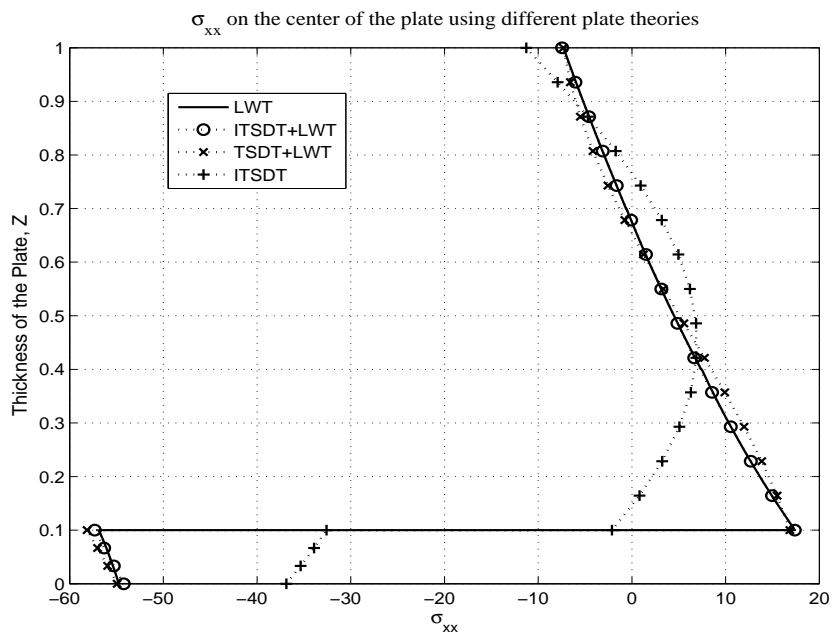


Fig. 33. $\bar{\sigma}_{xx}$ through thickness for a smart FGM plate under an applied voltage

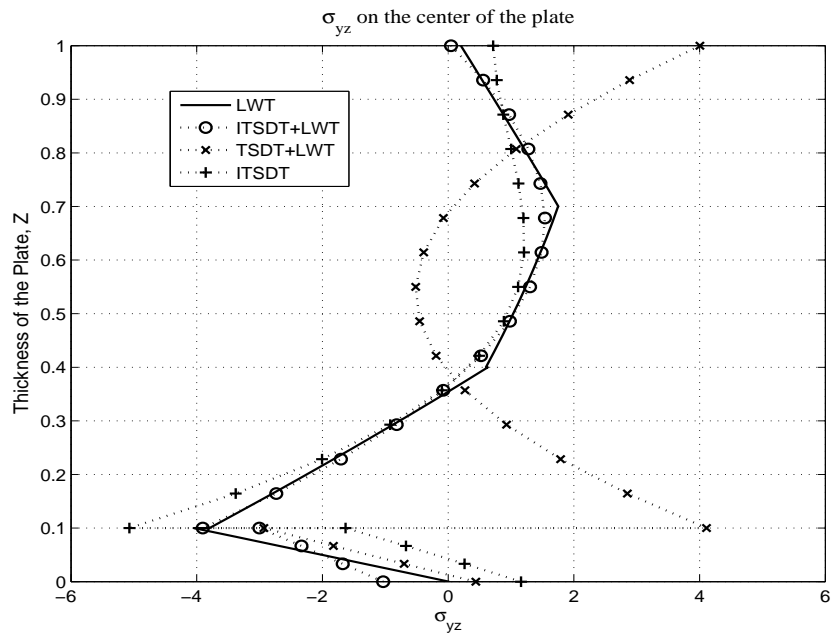


Fig. 34. $\bar{\sigma}_{yz}$ through thickness for a smart FGM plate under an applied voltage

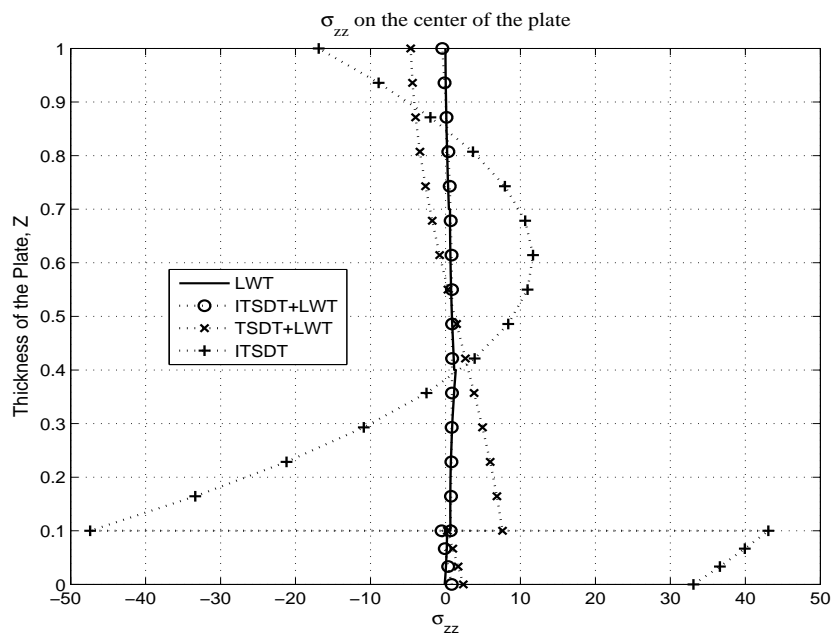


Fig. 35. $\bar{\sigma}_{zz}$ through thickness for a smart FGM plate under an applied voltage

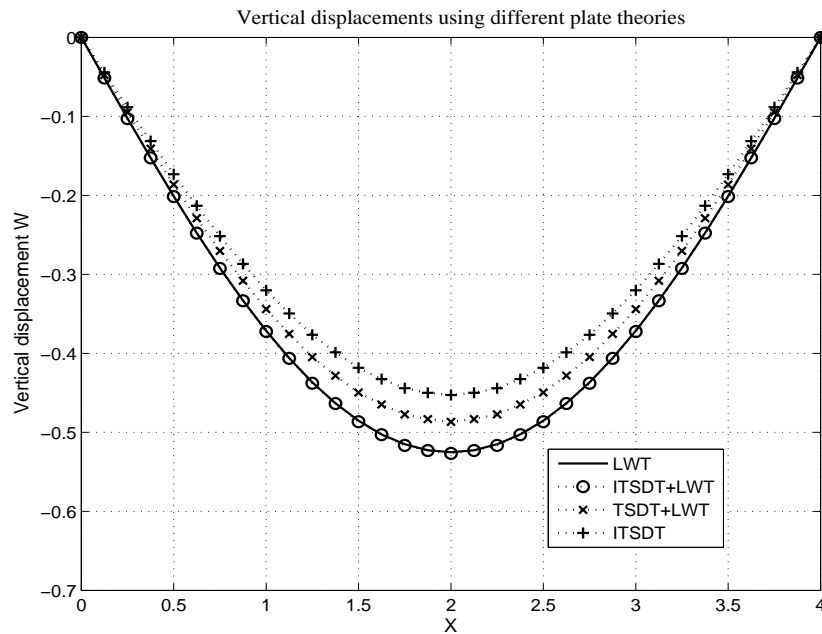


Fig. 36. Central deflection along the smart FGM plate length under an applied voltage

Figures 32 to 36 depict the graphical comparison among LWT, RITSdT, TSdT + LWT and ITSdT. It is very important to remark that in this case, we decided to present an improved version of TSdT, to study its behavior in comparison to ITSdT and RITSdT. The LWT added to TSdT has the same characteristics as the one used to generate the RITSdT. As we can observe in Fig. 32 TSdT+LWT performs better than ITSdT but does not generate values close to those produced by LWT. On the other hand, RITSdT provides very good results. The same observation can be made from Fig. 36, where the vertical displacement profile along the smart FGM plate is very well predicted using RITSdT when it is compared to LWT.

CHAPTER IV

DYNAMIC ANALYSIS

Dynamical systems, systems with physical effects that change with time, are very important in engineering applications. Among them, smart materials are good examples of dynamical systems since they undergo elastic, electrical and thermal fields that are time dependent. Hence, to appropriately describe the response of these systems, we shall employ Eq. 2.269 that allows us to carry out a fully coupled piezo-thermo-elastic analysis.

In order to make Eq. 2.269 more tractable, we will condense the electrical dofs of the piezoelectric part that acts as a sensor. Therefore, the two resultant equations are

$$\begin{aligned} M_{uu}\ddot{u}_u + C_{uu}\dot{u}_u + \bar{K}_{uu}u_u + K_{u\phi_a}\bar{u}_{\phi_a} + \bar{K}_{u\theta}u_\theta &= F_u \\ \bar{C}_{\theta u}\dot{u}_u + \bar{C}_{\theta\theta}\dot{u}_\theta + K_{\theta\theta}u_\theta &= F_\theta \end{aligned} \quad (4.1)$$

where

$$\begin{aligned} \bar{K}_{uu} &= K_{uu} - K_{u\phi_s} [K_{u\phi_s}]^{-1} K_{\phi_s u} \quad ; \quad \bar{K}_{u\theta} = K_{u\theta} - K_{u\phi_s} [K_{u\phi_s}]^{-1} K_{\phi_s \theta} \\ \bar{C}_{\theta u} &= C_{\theta u} - C_{u\phi_s} [K_{u\phi_s}]^{-1} K_{\phi_s u} \quad ; \quad \bar{C}_{\theta\theta} = C_{\theta\theta} - C_{u\phi_s} [K_{u\phi_s}]^{-1} K_{\phi_s \theta} \end{aligned} \quad (4.2)$$

and \bar{u}_{ϕ_a} is the imposed electrical field over the piezoelectric that acts as an actuator

As we can observe in Eq.4.1 the coupling between the elastic and thermal field can be found in the damping matrix. An uncoupled effect can be performed just neglecting the matrix $\bar{C}_{\theta u}$. Therefore, the heat equation can be solved independently from the elastic one.

Even though Eq.4.1 represents a quite general expression for smart materials, some particular cases becomes relevant for practical purposes. For instance, in the

absence of thermal field this equation can be simplified as

$$M_{uu}\ddot{u}_u + C_{uu}\dot{u}_u + \bar{K}_{uu}u_u = \bar{F}_u \quad (4.3)$$

where

$$\bar{F}_u = F_u - K_{u\phi_a}\bar{u}_{\phi_a} \quad (4.4)$$

which typically represents an isothermal process for a sensing-actuation structural system.

Another interesting situation that allows some simplification of the Eq.4.1 is represented by a thermal shock . In this case, a static thermal field is suddenly applied to the whole domain of the smart material. Then

$$M_{uu}\ddot{u}_u + C_{uu}\dot{u}_u + \bar{K}_{uu}u_u = \bar{F}_u - K_{u\theta}\bar{u}_\theta \quad (4.5)$$

with

$$\bar{u}_\theta = [K_{\theta\theta}]^{-1} F_\theta \quad (4.6)$$

On the other hand, since the temperature over the whole domain evolves at much slower rate than the displacements, the assumption of a dynamical thermal and static elastic field seems to be reasonable. Then Eq. 4.1 takes the form

$$\begin{aligned} \bar{K}_{uu}u_u + \bar{K}_{u\theta}u_\theta &= \bar{F}_u \\ \bar{C}_{\theta u}\dot{u}_\theta + \bar{C}_{\theta\theta}\dot{u}_\theta + K_{\theta\theta}u_\theta &= F_\theta \end{aligned} \quad (4.7)$$

If we condensed the elastic dofs, we obtain

$$\tilde{C}_{\theta\theta}\dot{u}_\theta + K_{\theta\theta}u_\theta = \tilde{F}_\theta \quad (4.8)$$

where

$$\begin{aligned}\tilde{C}_{\theta\theta} &= \bar{C}_{\theta\theta} - \bar{C}_{\theta u} [\bar{K}_{uu}]^{-1} \bar{K}_{u\theta} \\ \tilde{F}_{\theta} &= F_{\theta} - [\bar{K}_{uu}]^{-1} \bar{F}_u\end{aligned}\quad (4.9)$$

A. Applications

In this section, the FGM and Smart FGM plate used in Chapter III (n=2.0) will be employed again. However, in this case, the quasi-static assumption will be relaxed and consequently a dynamical analysis will be carried out. The mechanical, thermal and electrical loads applied to the structure are going to be the same as the ones applied in the static case. In the sequel, for all the applications, the plate will be simply supported in all its edges. Unless specified, the computational domain will be a quarter plate and the mesh will be comprised by 4×4 elements. Moreover, it is assumed Rayleigh structural damping with $\alpha = \beta = 10^{-5}$

1. FGM Plate

As it was shown in the previous chapter, ITSDT provides excellent results in the calculation of vertical displacements. Here we are going to use the same ITSDT elements as the ones used in the previous chapter to compute the mechanical field. For the thermal field, the theory used will change according to the characteristic of the problem.

a. Mechanical Load

In this part, a free vibration problem will be presented to test the performance of ITSDT to handle dynamical problems. A 4 node element with ITSDT will be employed. For the FGM plate specified above, we are going to generate our initial

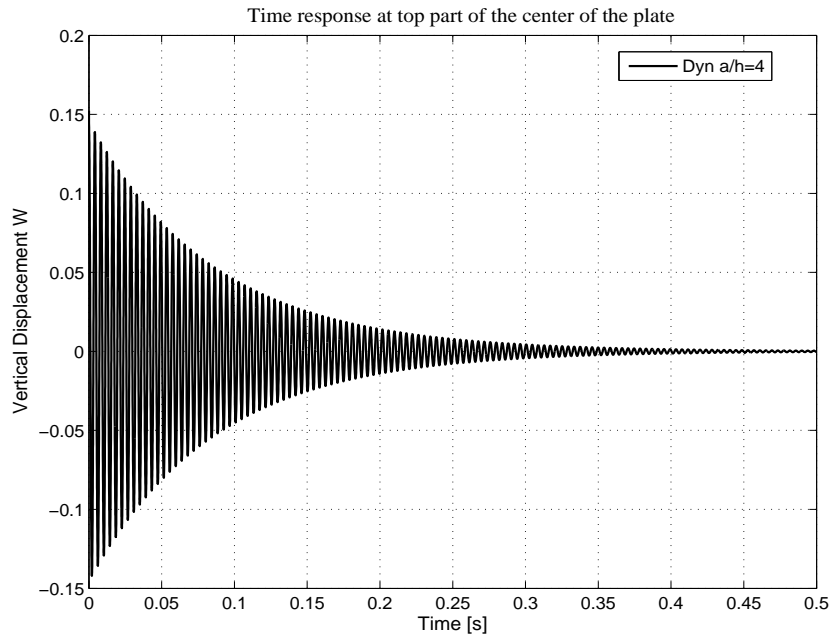


Fig. 37. Time response of the center of the FGM plate for $a/h=4$

conditions applying the mechanical load specified in Eq. 3.7. When the equilibrium is attained, we remove the force and allow the plate to oscillate freely. Figures 37, 38 and 39 show the evolution of the non-dimensionalized vertical displacement \bar{w} (given by Eq. 3.8) at the top of the plate, for the cases where the plate has span to thickness ratio (b/h) equal to 4, 10 and 50. Even though this is a very simple example, it is interesting to verify that the plate with higher ($b/h = 50$) span-thickness ratio is the more flexible structure. In other words, that plate has smaller frequencies compared to the other plates, and therefore, its period is the greatest as it can be observed in the figures.

b. Thermal Load

If the thermal field produced by the temperature profile specified in Eq. 3.7 is suddenly imposed in the whole domain of the FGM plate, we are in the case of the

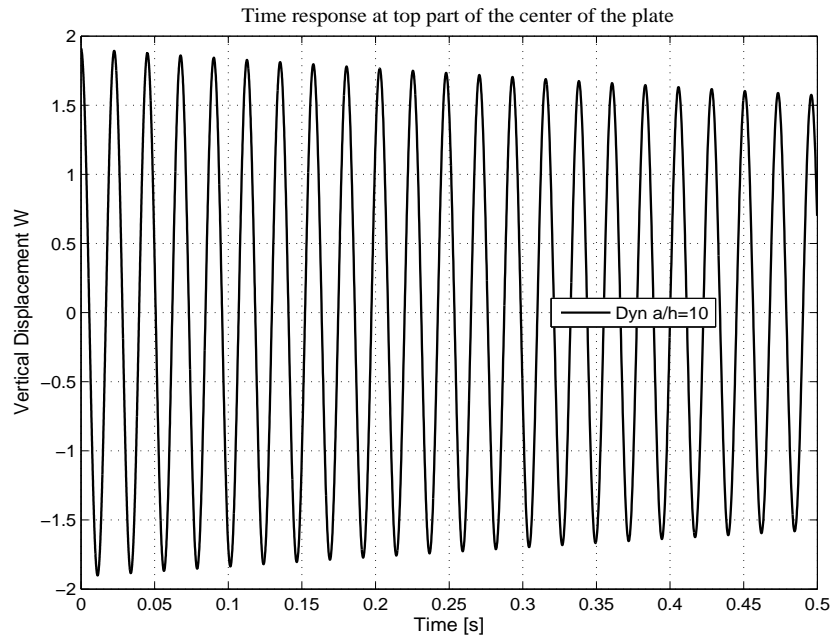


Fig. 38. Time response of the center of the FGM plate for $a/h=10$

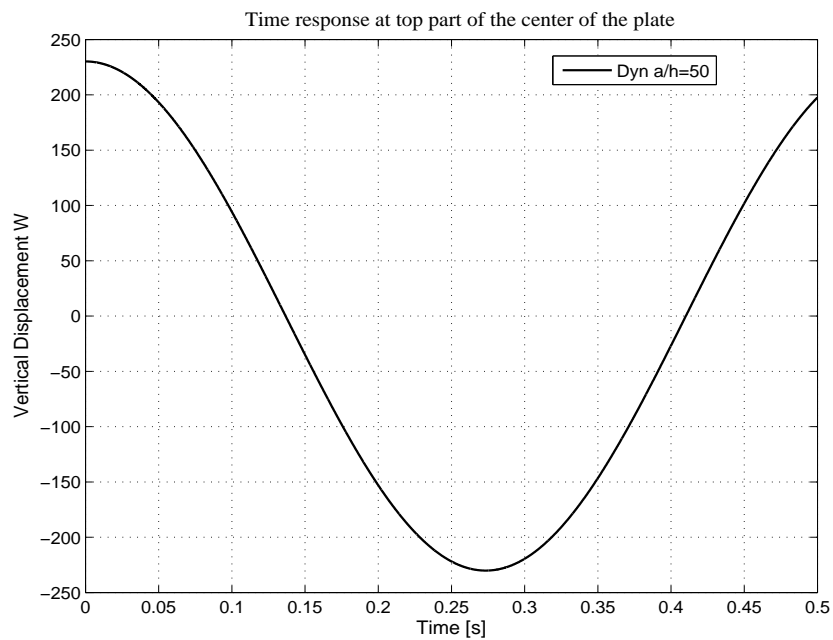


Fig. 39. Time response of the center of the FGM plate for $a/h=50$

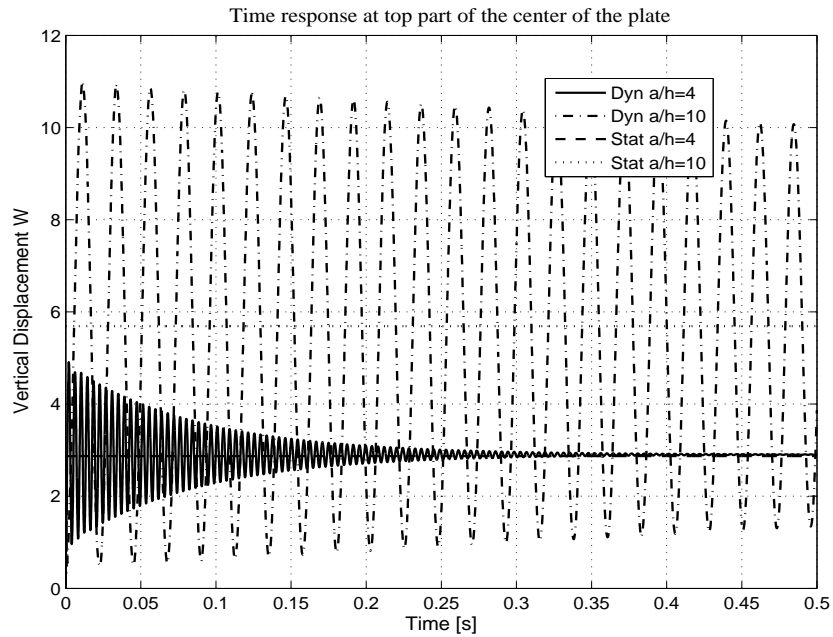


Fig. 40. Time response of the center of the FGM plate when a thermal shock is imposed thermal shock described by Eq. 4.5. Since no time temperature evolution is necessary to be calculated, the equivalent single layer for temperature will be used. As we did in Chapter III, 9 node element will be employed, where 4 of the nodes - the ones in the corners - contain mechanical dofs, and all 9 nodes contains thermal dofs. Fig. 40 depicts the time response of the structure \bar{w} (Eq. 3.8) for two different span-thickness ratio and they are compared with the static values calculated in the previous section. As we can observe, the static values represent the equilibrium point around which the structures oscillates.

On the other hand, if we consider a more realistic case, where the thermal field evolves with time until it reaches its equilibrium, the LWT model to represent temperature is more convenient. Moreover, the two cases considered above where the dynamic heat equation can be solved independently from the elastic field (uncoupled) and the one where this field can be condensed (coupled) (Eq. 4.7) deserve special

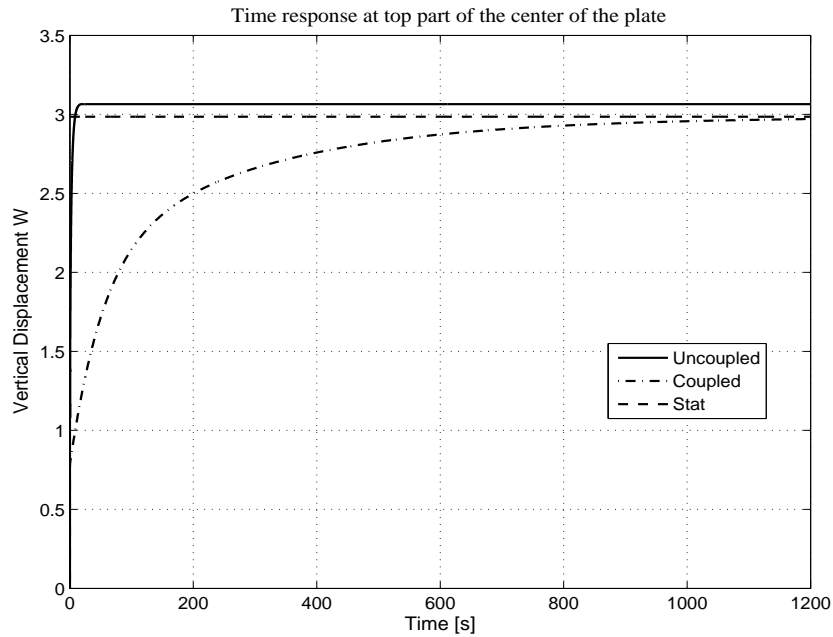


Fig. 41. Time response of the center of the FGM plate for an imposed thermal boundary condition

attention. According to this, Figures 41 and 42 represent the history of \bar{w} and the temperature increase and significantly differences can be easily observed. First, if we perform a coupled analysis, the stabilization point will be reached faster than if we use an uncoupled analysis. This makes perfect sense since the coupling between the elastic and thermal field in the heat equation is given by a damping term. This term will slow down the temperature change because the conductive heat over the structure affects both the thermal and elastic field; meanwhile, in the uncoupled analysis the thermal field is the only one affected by the heat transfer process.

An important remark is that the uncoupled analysis demands a lot of computational resources. Because of this, we have employed a very course mesh (2×2) only for this analysis. This is the reason why in Fig 41 the final vertical displacement \bar{w} obtained from the uncoupled analysis is higher than the one obtained performing the coupled analysis.

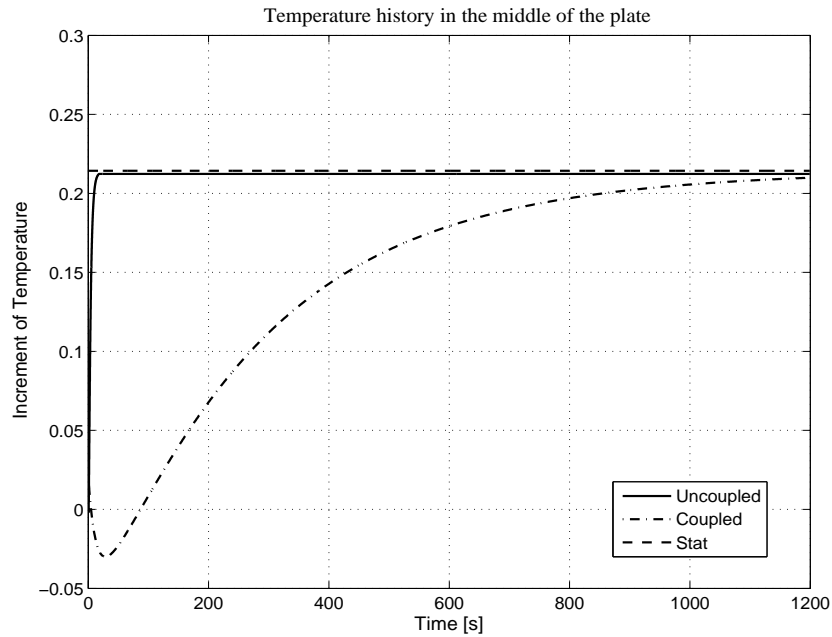


Fig. 42. Temperature increase evolution on the center point of the middle plane of the plate for an imposed thermal boundary condition

2. Smart FGM Plate

Here the elements to be used are similar to the ones used for FGM plate; however, there are two important differences. The first one is that in all the cases the electrical field is expressed using LWT representation and all the 9 nodes of the element should contain electrical variables, too. And the second difference is that for the mechanical field we are going to use RITSDT for the cases where electrical and thermal load is applied. For the mechanical load ITSDT is enough.

a. Mechanical Load

Likewise the FGM plate, the Smart FGM plate is submitted to an initial displacement and allowed to vibrate freely. Figures 43, 44 and 45 depict the time evolution of \bar{w} for the cases when the span-thickness ratio is 4, 10 and 20, respectively. As we

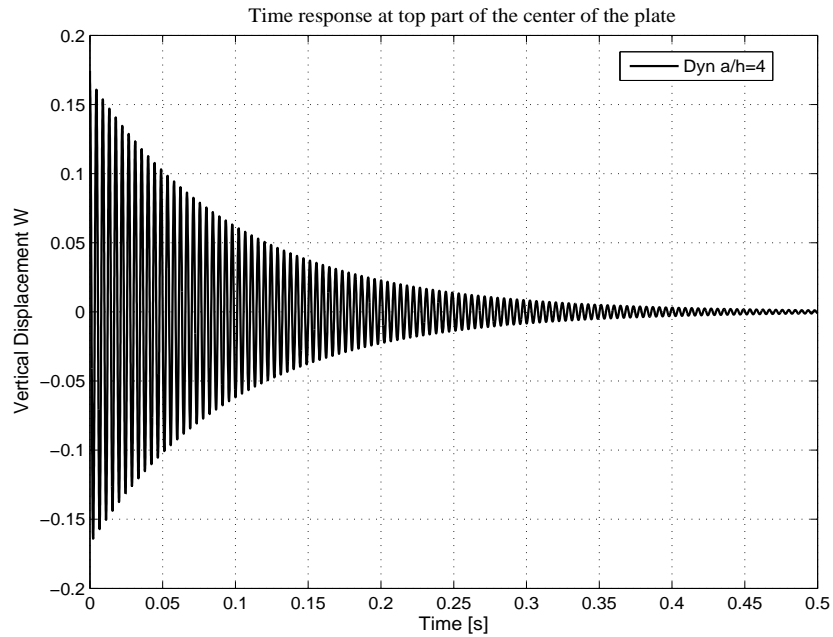


Fig. 43. Time response of the center of the smart FGM plate for $a/h=4$

can observe, the profiles obtained are pretty similar to the ones obtained in the absence of the piezoelectric layer. This fact means that the electrical field adapts to the mechanical one, reproducing its behavior proportionally. This is the main fact why piezoelectric materials can be used as a sensor. This assertion can be easily verified in Figures 46, 47 and 48 where we can notice the history voltage in the middle plane of the piezoelectric layer for different span-thickness ratios.

b. Thermal Load

Here we are going to apply a similar thermal shock as was applied in the case of FGM plate. The mechanical and electrical response of the system can be observed in Figures 49 and 50, respectively. Since under a thermal shock the smart structure behaves similarly to a mechanical impact, we can expect that the electrical field proportionally reproduces the dynamic of the smart plate as we can see in Fig. 50.

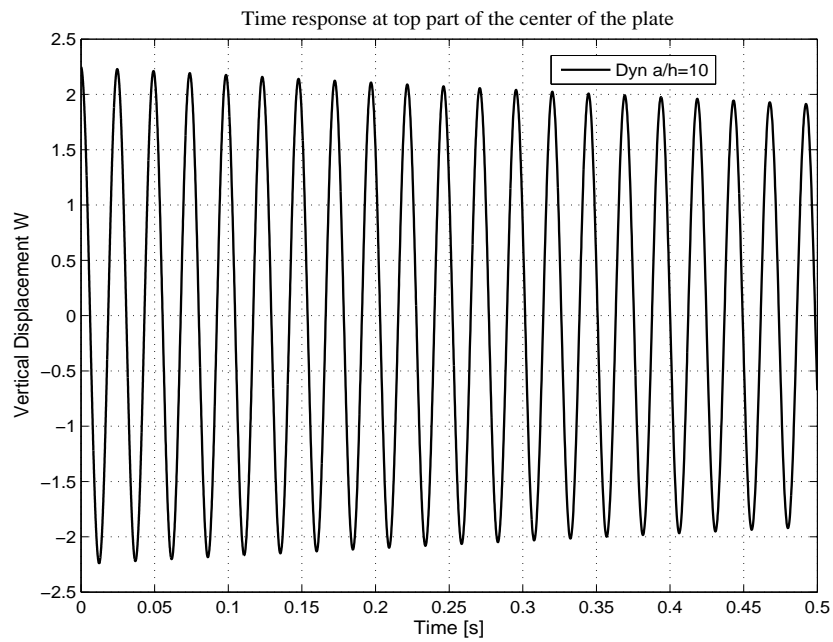


Fig. 44. Time response of the center of the smart FGM plate for $a/h=10$

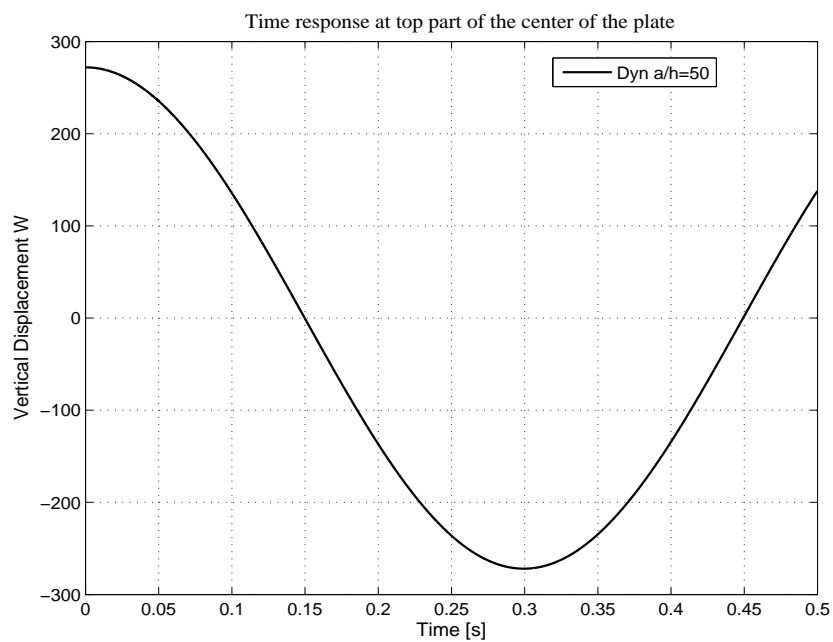


Fig. 45. Time response of the center of the smart FGM plate for $a/h=50$

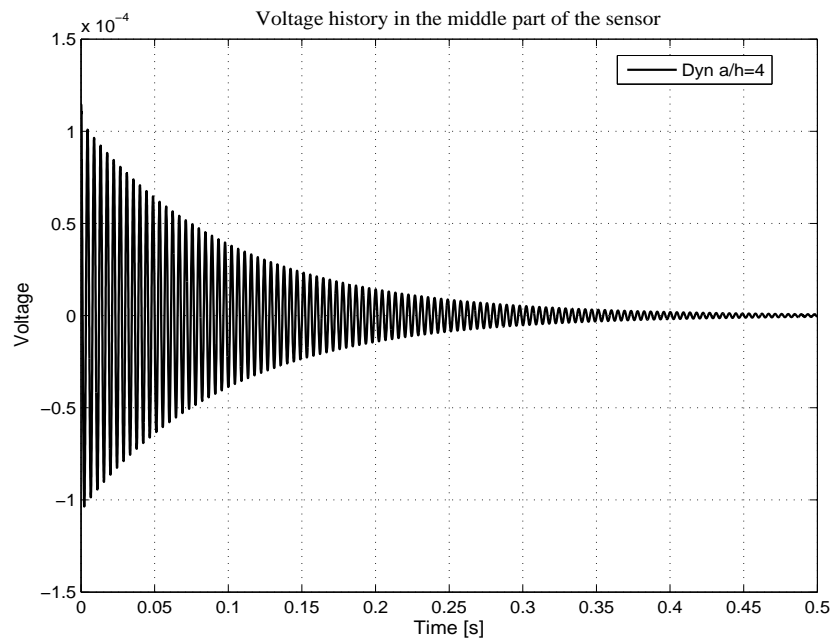


Fig. 46. Voltage evolution in the middle plane of the sensor for $a/h=4$

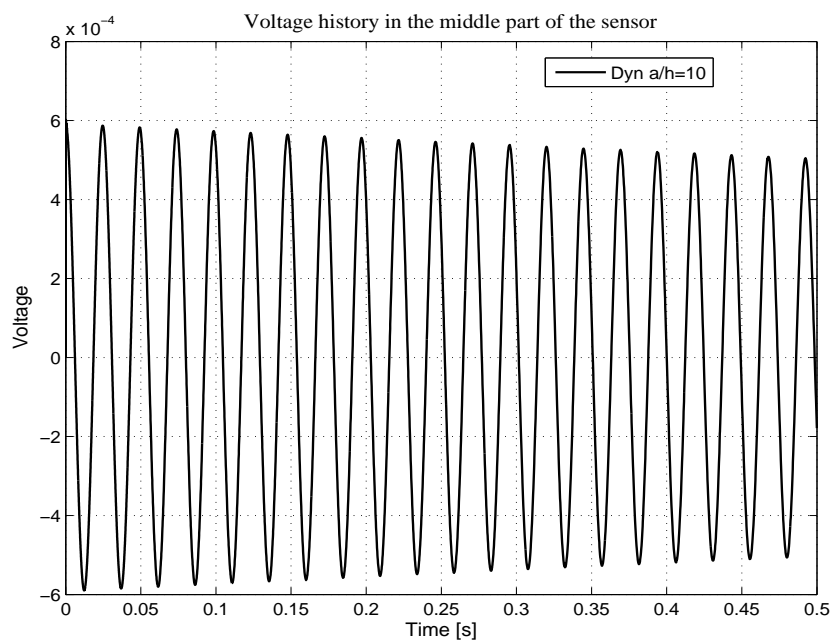


Fig. 47. Voltage evolution in the middle plane of the sensor for $a/h=10$

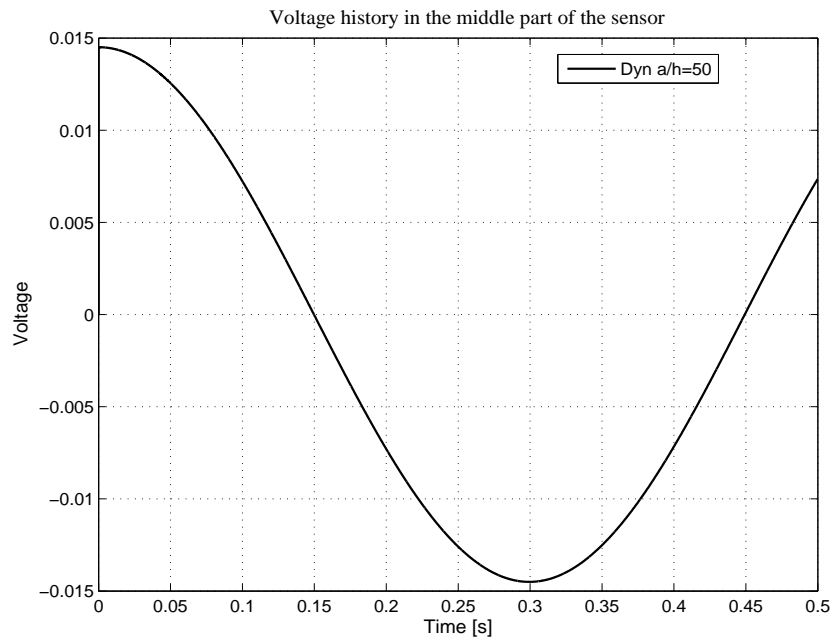


Fig. 48. Voltage evolution in the middle plane of the sensor for $a/h=50$

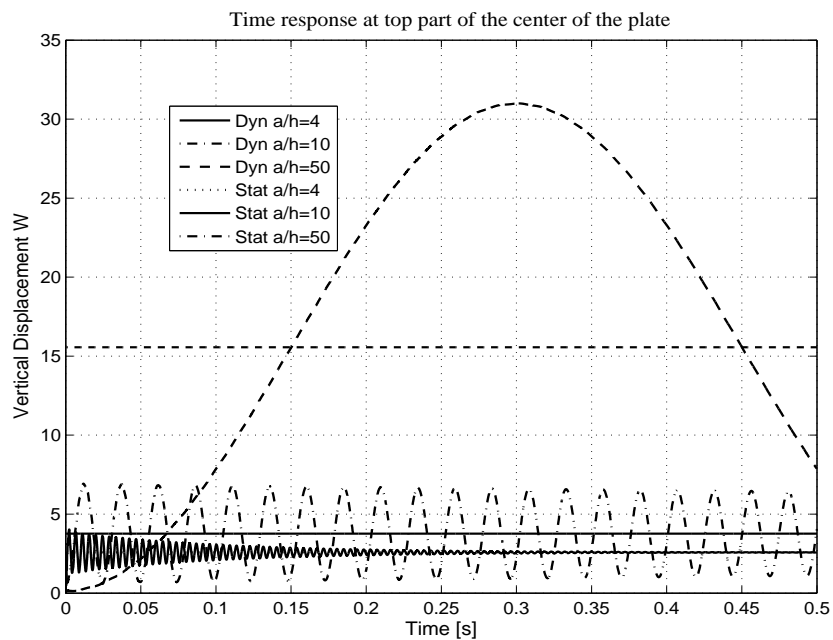


Fig. 49. Time response of the center of the smart FGM plate when a thermal shock is imposed

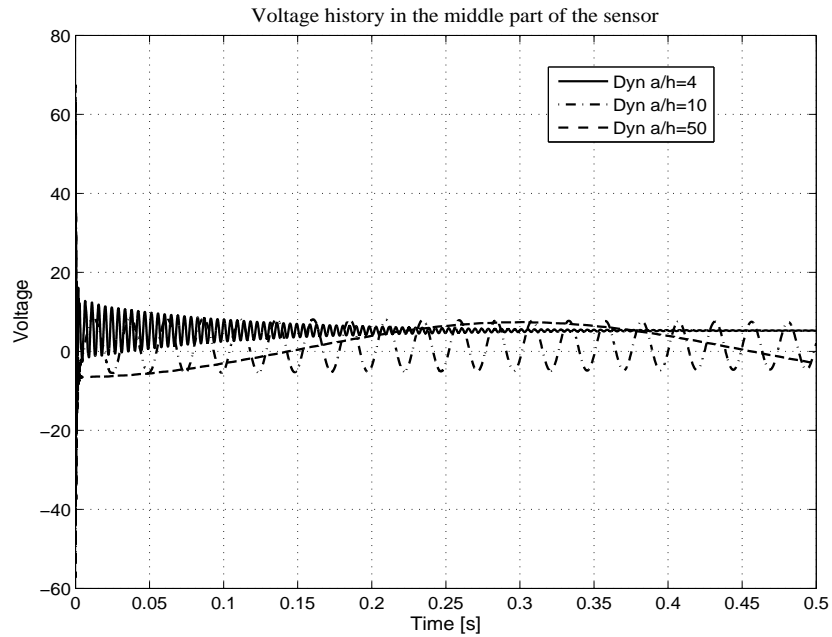


Fig. 50. Voltage evolution in the middle plane of the sensor when a thermal shock is imposed

On the other hand, the results of performing a coupled and uncoupled analysis can be compared in Fig. 51 when $b/h = 4$. Comparing figures 41 and 51, we can notice a difference that is worthy to comment. Either for the coupled or uncoupled analysis, the time history of \bar{w} of the pure FGM plate reaches the equilibrium point only once at the end of the process. However, in the Smart FGM plate this phenomena happens twice, the first one at a relatively early stage and the second time after a long period of time. This means that the electrical field provides an initial boost to the structure due to its capacity to react faster compared to the mechanical and thermal field; in other words, this effect is like an small impact. After some time, the other fields start combining with the electrical one, causing a deceleration process until a maximum point is reached. This is the point where all the effects are present and able to interact, and after this, the process of reaching the equilibrium point starts taking place. In the coupled analysis, since the energy due to the heat conduction

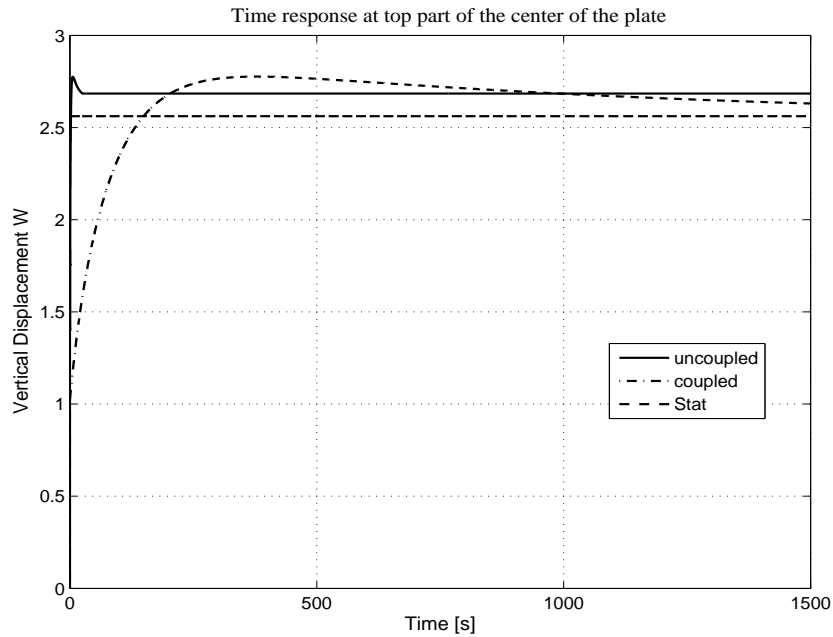


Fig. 51. Time response of the center of the smart FGM plate for an imposed thermal boundary condition

over the plate is used to produce an evolution in three different fields, the system will take a while to reach the equilibrium point. This period of time will be bigger than the time in the pure FGM plate.

c. Electrical Load

Finally, the case where a sinusoidal voltage (Eq. 3.9) imposed over the bottom part of the piezoelectric layer of the plate will be analyzed. Fig 52 shows the evolution of \bar{w} for two different span-thickness ratios. As we can see, the oscillation for the two cases takes place around their corresponding equilibrium point. This kind of load allows us to realize that the structure with greater span-thickness ratio is more flexible.

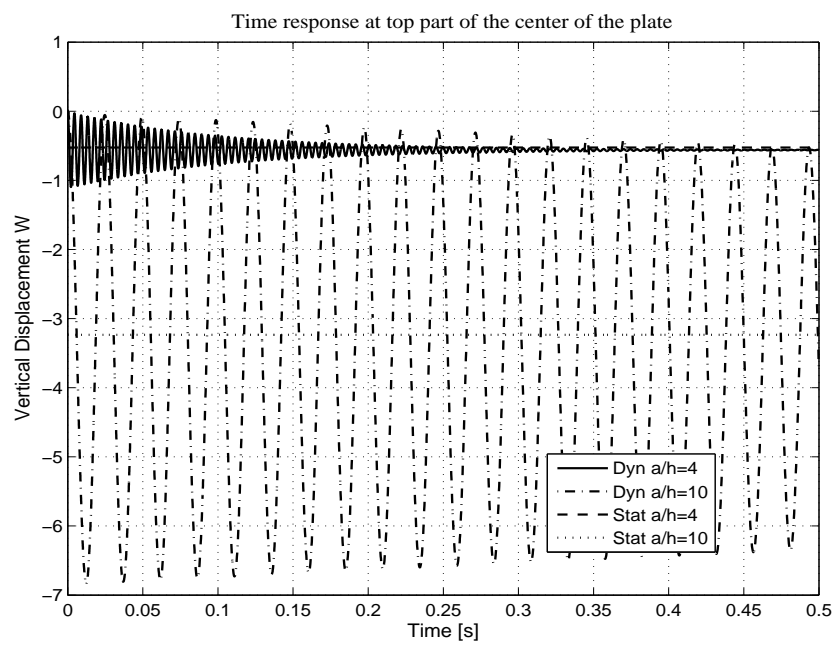


Fig. 52. Time response of the center of the smart FGM plate for an imposed sinusoidal voltage distribution

CHAPTER V

ACTIVE VIBRATION CONTROL OF SMART FGM PLATES

A. Negative Velocity Feedback

Recalling the Eq. 2.269 and considering an isothermal process, we obtain

$$\begin{aligned}
 M_{uu}\ddot{u}_u + C_{uu}\dot{u}_u + K_{uu}u_u + K_{u\phi_s}u_{\phi_s} + K_{u\phi_a}u_{\phi_a} &= F_u \\
 K_{\phi_s u}u_u + K_{\phi_s\phi_s}u_{\phi_s} &= 0 \\
 K_{\phi_a u}u_u + K_{\phi_a\phi_a}u_{\phi_a} &= F_{\phi_a}
 \end{aligned} \tag{5.1}$$

Then, condensing the electrical dofs yields

$$\begin{aligned}
 M_{uu}\ddot{u}_u + C_{uu}\dot{u}_u + \left(K_{uu} - K_{u\phi_s} [K_{\phi_s\phi_s}]^{-1} K_{\phi_s u} - K_{u\phi_a} [K_{\phi_a\phi_a}]^{-1} K_{\phi_a u} \right) u_u \\
 = F_u - K_{u\phi_a} [K_{\phi_a\phi_a}]^{-1} F_{\phi_a}
 \end{aligned} \tag{5.2}$$

When the structure is vibrating, the piezoelectric sensor generates an output voltage. This voltage can be amplified and is fed back to the actuators. From the actuator equation (third expression in Eq. 5.1), we can say that the force induced in the actuator is a linear combination of its voltage and the elastic field

$$F_{\phi_a} = f(u_u, u_{\phi_a}) \tag{5.3}$$

The negative velocity feedback control strategy is based on the assumption of proportionality between the actuator and time derivative sensor voltages, $\phi_a \propto \dot{\phi}_s$. Using the previous assumption and the actuator equation, we can conclude that F_{ϕ_a} is also proportional to $\dot{\phi}_s$, so

$$F_{\phi_a} = f(u_u, \dot{\phi}_s) \tag{5.4}$$

From the sensor equation, we see $\dot{u}_u \propto \dot{\phi}_s$, then

$$F_{\phi_a} = f(u_u, \dot{u}_u) \quad (5.5)$$

Therefore, the electrical flux applied to the actuator should be

$$F_{\phi_a} = G_1 K_{\phi_a u} u_u + G_2 K_{\phi_a u} \dot{u}_u \quad (5.6)$$

in this case $G_1 = 1$ according to the actuator equation. Replacing Eq. 5.6 into Eq. 5.2

$$\begin{aligned} M_{uu} \ddot{u}_u + C_{uu} \dot{u}_u + K_{uu} u_u - K_{u\phi_s} [K_{\phi_s \phi_s}]^{-1} K_{\phi_s u} u_u - K_{u\phi_a} [K_{\phi_a \phi_a}]^{-1} K_{\phi_a u} u_u \\ = F_u - K_{u\phi_a} [K_{\phi_a \phi_a}]^{-1} (K_{\phi_a u} u_u + G_2 K_{\phi_a u} \dot{u}_u) \end{aligned} \quad (5.7)$$

Therefore, the vibration of a plate with a negative velocity feedback control loop can be expressed as

$$M_{uu} \ddot{u}_u + \bar{C}_{uu} \dot{u}_u + \bar{K}_{uu} u_u = F_u \quad (5.8)$$

where

$$\begin{aligned} \bar{C}_{uu} &= C_{uu} + G_2 K_{u\phi_a} [K_{\phi_a \phi_a}]^{-1} K_{\phi_a u} \\ \bar{K}_{uu} &= K_{uu} - K_{u\phi_s} [K_{\phi_s \phi_s}]^{-1} K_{\phi_s u} \end{aligned} \quad (5.9)$$

1. Application

To illustrate the negative feedback control strategy, we will apply an initial displacement (using the sinusoidal load of Eq. 3.7) to a Smart FGM plate of span-thickness ratio of 10. This plate will have a core of FGM with $n = 2.0$, which represents 90% of the thickness, and in its bottom part, it will be attached to a piezoelectric layer that will act as a sensor (5% of the thickness). Similarly, in its top part another piezoelectric layer will be mounted to act as an actuator. The Smart FGM

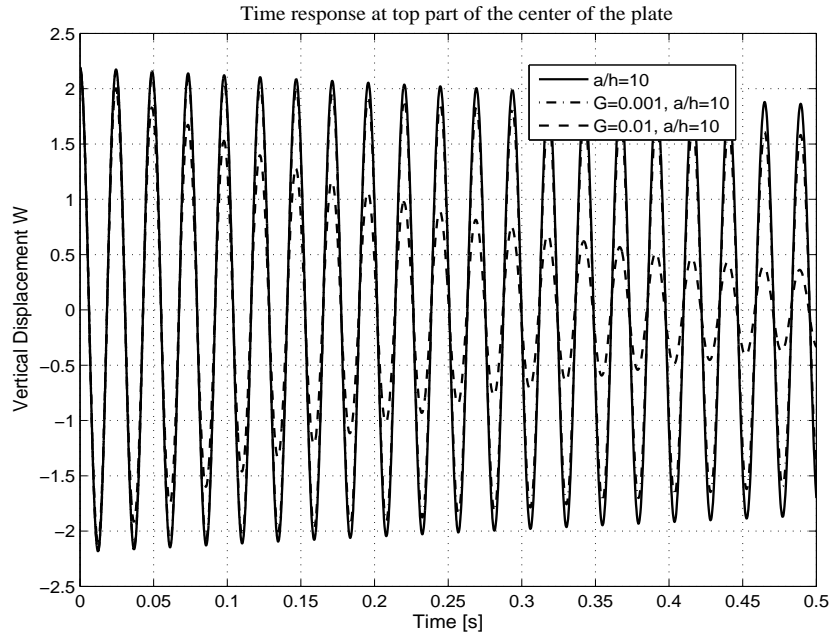


Fig. 53. Time responses at the top part of the center of the plate for different gain values G

plate will be simple supported, and due to the symmetry of the problem, a quarter plate will be used as a computational domain. A mesh of 4×4 elements will be employed and the non dimensionalized displacement \bar{w} represented by Eq. 3.8 will be considered. Moreover, the element to be employed will have 9 nodes, where all of them have LWT for electrical (sensor and actuator) degrees of freedom (dofs), and three levels for each mathematical layer, and only 4 nodes (the one in the corners) will contain ITSDT for mechanical dofs. In order to simplify the electrical dofs, for both sensor and actuator layers will be taken as one mathematical layer for each case.

Fig. 53 shows the \bar{w} time response for different values of G . As it is expected when G grows the damping of the structure increases. It is remarkable that in the case where $G = 0$, the structure only has an structural Rayleigh damping whose coefficients are $\alpha = 10^{-5}$ and $\beta = 10^{-5}$.

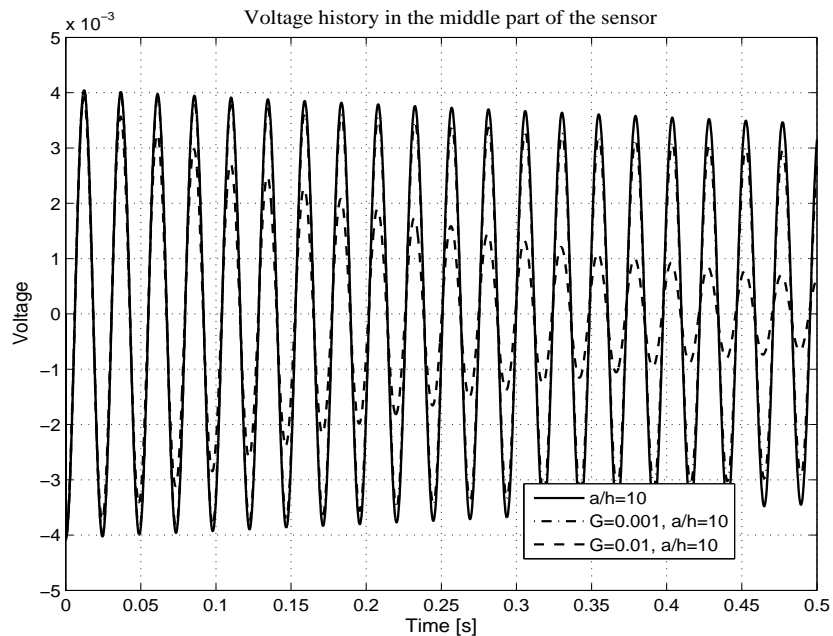


Fig. 54. Voltage history of the middle plane of the sensor for different gain values G

B. Optimal Control

Let's consider the system of first-order ordinary differential equation

$$\dot{x} = f(x, u, t) \quad (5.10)$$

where x is the state variable vector and u the control vector. The optimization problem consists of finding the vector u that minimize the functional

$$J(t_0) = \int_{t_0}^{t_1} L(x, u) dt \quad (5.11)$$

To minimize J with the constraint represented by 5.10, we define the augmented functional J^*

$$J^* = \int_{t_0}^{t_1} \{L(x, u) + r^T [f(x, u, t) - \dot{x}]\} dt \quad (5.12)$$

if we define the Hamiltonian

$$H(x, u, r, t) = L(x, u) + r^T f(x, u, t) \quad (5.13)$$

J^* can be expressed as

$$J^* = \int_{t_0}^{t_1} [H(x, u, r, t) - r^T \dot{x}] dt \quad (5.14)$$

the solution of the expression $dJ^* = 0$ determines the minimum of J provided $d^2J > 0$, then

$$dJ^* = [(H - r^T \dot{x})\delta t]_{t_0}^{t_1} + \int_{t_0}^{t_1} \left[\frac{\partial H^T}{\partial x} \delta x + \frac{\partial H^T}{\partial u} \delta u - r^T \delta \dot{x} + \left(\frac{\partial H}{\partial r} - \dot{x} \right)^T \delta r \right] dt \quad (5.15)$$

after integrating by parts and performing some algebraic manipulation, Eq. 5.15 yields

$$dJ^* = \left[\left(\frac{\partial H^T}{\partial r} \dot{x} \right) \delta t - r^T \delta x \right]_{t_0}^{t_1} + \int_{t_0}^{t_1} \left[\left(\frac{\partial H^T}{\partial x} + \dot{r} \right) \delta x + \frac{\partial H^T}{\partial u} \delta u \right] dt + \int_{t_0}^{t_1} \left[\left(\frac{\partial H}{\partial r} - \dot{x} \right)^T \delta r \right] dt \quad (5.16)$$

Since $dJ^* = 0$ must hold for any δr , δx and δu , we obtain the following equations

$$\frac{\partial H}{\partial x} + \dot{r} = 0 \quad (5.17)$$

$$\frac{\partial H}{\partial u} = 0 \quad (5.18)$$

$$\frac{\partial H}{\partial r} = \dot{x} \quad (5.19)$$

C. Linear Quadratic Regulator (LQR)

Since the quadratic expression $x^T Q x$ measures the distance from the equilibrium $x = 0$ and represent the energy of the system, and $u^T R u$ the control energy, we can write J as

$$J = \frac{1}{2} \int_{t_0}^{t_1} (\hat{x}^T Q \hat{x} + u^T R u) dt \quad (5.20)$$

where Q and R are semi positive definite weighting matrices. Due to asymptotic stability, the quadratic integral J must converge and $x \rightarrow 0$ and $u \rightarrow 0$ as $t \rightarrow \infty$. Moreover, if we define the Hamiltonian as

$$H = \frac{1}{2}(\hat{x}^T Q \hat{x} + u^T R u) + r^T (\hat{A} \hat{x} + \hat{B} u) \quad (5.21)$$

and using Eqs. 5.17, 5.18 and 5.19 yields

$$Q \hat{x} + \hat{A}^T r + \dot{r} = 0 \quad (5.22)$$

$$R u + \hat{B}^T r = 0 \Rightarrow u = -R^{-1} \hat{B}^T r \quad (5.23)$$

$$\dot{\hat{x}} = \hat{A} \hat{x} + \hat{B} u \quad (5.24)$$

If we assume that the Lagrangian multiplier is proportional to the state vector $r = P \hat{x}$, the matrix P can be calculated using the Ricatti equation

$$-\dot{P} = \hat{A}^T P + P \hat{A} + Q - P \hat{B} R^{-1} \hat{B}^T P \quad (5.25)$$

and the Kalman Filter can be calculated as

$$K_g^*(t) = R^{-1} \hat{B}^T P(t) \quad (5.26)$$

Therefore, the close loop system behaves according to

$$\dot{\hat{x}} = (\hat{A} - \hat{B} K_g) \hat{x} + p$$

$$y = \hat{C}\hat{x} \quad (5.27)$$

1. Choice of the Weighted State Matrix

The main purpose of using Optimal control is to minimize the energy due to vibration of the structure. Since the term associated with this energy is $(1/2)x^T Qx$, the weighted matrix Q plays an important role in the optimization process.

We know that the state vector is composed of the modal displacement (χ) and the velocities ($\dot{\chi}$) of the structure

$$\hat{x} = \begin{Bmatrix} \chi \\ \dot{\chi} \end{Bmatrix} \quad (5.28)$$

according to this, the matrix Q can be splitted as

$$Q = \begin{bmatrix} Q_{\chi\chi} & Q_{\chi\dot{\chi}} \\ Q_{\dot{\chi}\chi} & Q_{\dot{\chi}\dot{\chi}} \end{bmatrix} \quad (5.29)$$

As a matter of simplification, let's assume that $Q_{\chi\dot{\chi}} = Q_{\dot{\chi}\chi} = 0$. Then, some important cases can be considered to determine $Q_{\chi\chi}$ and $Q_{\dot{\chi}\dot{\chi}}$.

The first important case is the uniform control of all the modes. Here, we achieved our objective by setting $Q_{\chi\chi} = Q_{\dot{\chi}\dot{\chi}} = I$, where I is the identity matrix. Another important situation is the control of "n" modes of the system. Likewise the first case $Q_{\chi\chi} = Q_{\dot{\chi}\dot{\chi}}$, but $Q_{\chi\chi}$ take the following form

$$Q_{\chi\chi} = \begin{bmatrix} Q_n & 0 \\ 0 & 0 \end{bmatrix} \quad (5.30)$$

If the objective is to control this n modes uniformly $Q_n = I_n$; however if some modes are to be suppressed more than others, Q_n will be a diagonal matrix whose values are the weights of each mode.

A similar case from the previous one can be

$$Q_n = \begin{bmatrix} \omega_1^2 & & & \\ & \cdot & & \\ & & \cdot & \\ & & & \omega_n^2 \end{bmatrix} ; \quad Q_{\dot{x}\dot{x}} = \begin{bmatrix} I & 0 \\ 0 & 0 \end{bmatrix} \quad (5.31)$$

here $Q_{xx} \cong Q_{\dot{x}\dot{x}}$.

2. Application

In this case, we will apply the LQR control to the same Smart FGM plate described in the Negative Velocity Feedback section. The loads, boundary conditions, and mesh to be employed are also the same. The matrix Q chosen for this application has the following form $Q = \gamma I$. Fig. 54 shows the comparison between \bar{w} when the structure is vibrating freely and under the influence of the LQR control strategy. In this situation $\gamma = 10^{-5}$

It is very important to point out that in Negative Velocity Feedback algorithm, we modify the structural damping of the plate through the assumption of proportionality between the sensor reading and the actuator voltages, without giving any additional constraint. However, when applying LQR, the energy of the system is to be minimized over a period of time, and as a consequence a electrical input is applied to the structure according to sensor readings and specific requires such as equally control for all the modes and so on. As a consequence, the decay of the \bar{w} time response is greater when LQR is employed as we can notice in Figures 53 and 55.

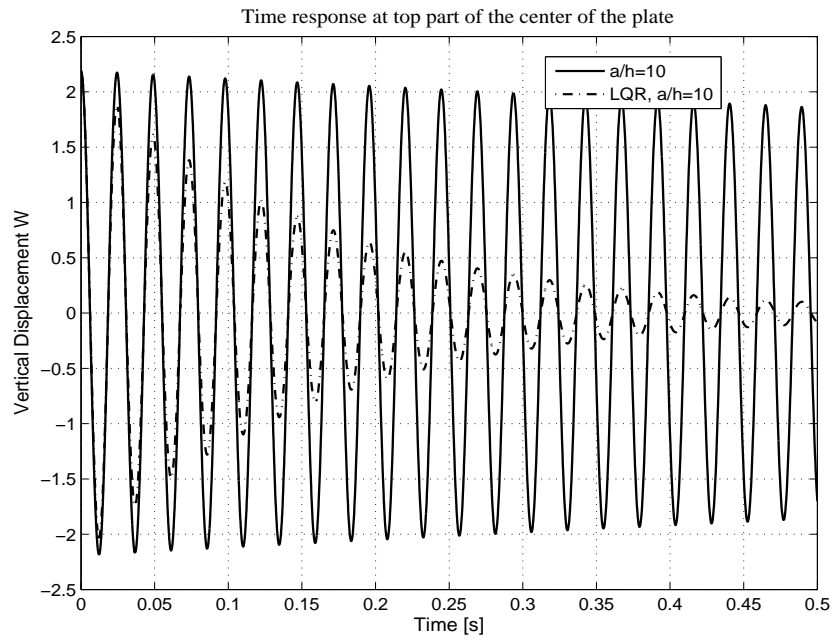


Fig. 55. Time responses at the top part of the center of the plate when LQR is used

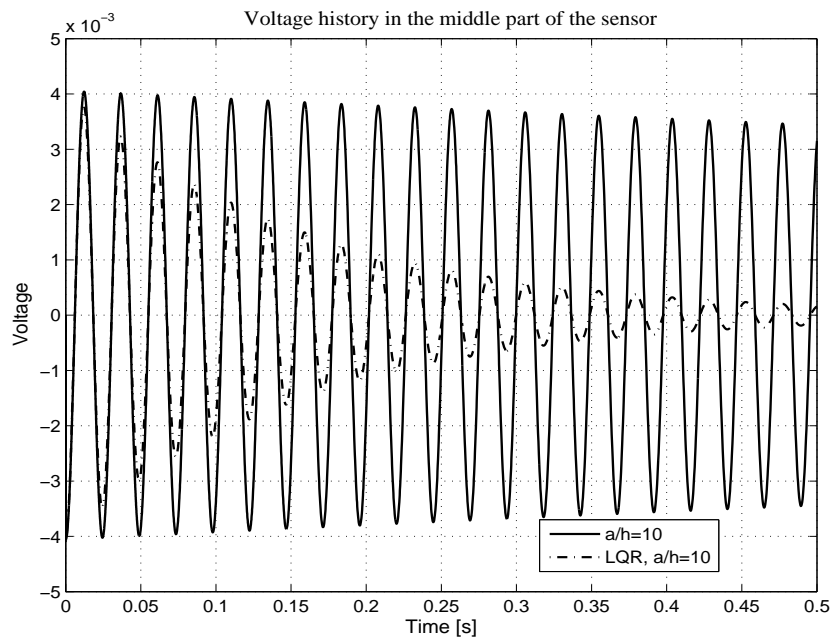


Fig. 56. Voltage history of the middle plane of the sensor when a LQR control is applied

CHAPTER VI

SUMMARY AND CONCLUSIONS

The primary objective of this study was to develop an improved third-order plate theory and associated finite element model to solve plate problems with actuators and sensors that have both 2-D and 3-D fields as well as thermo-piezo-mechanical coupling in the problem. In particular, the following tasks were carried out:

- Used the refined finite element to investigate different issues related to smart structures such as

Diverse configuration of their components

Accurate stress-strain analysis

Analysis several physical effects

- Performed a fully coupled thermo-piezo-elastic analysis of smart structures for static as well as dynamic response.
- Studied vibration control of plates using active control strategies.

The following conclusions are drawn from this study:

- The improved third-order shear deformation theory (ITSDT) developed in this work yield very accurate results compared to any existing single-layer plate theories and yet computationally economical. The Hermite interpolation functions used to generate ITSDT represent a important improvement through the thickness of the displacement field. Consequently, the finite element based on ITSDT has less sensitivity to shear locking as we can see in the examples where the span-to-thickness ratio is equal to 50.

- The fact of using interpolation functions that are continuous along with their derivatives with respect to z allow us to handle the continuous inhomogeneity of the FGM plates. Therefore, we can predict deformation profiles that are in good agreement with LWT.
- In the case of composite plates, the lack of improvement in the \bar{w} values comes from the fact that ITSDT does not have C^0 functions over the thickness; hence the discontinuities of stresses such as σ_{xx} and σ_{yy} can not be fully represented, and in this case the ITSDT's behavior is very similar to TSDT.
- Likewise in composite, the sudden change between materials when a piezoelectric layer is attached to a FGM plate, causes a poor performance of ITSDT. However, after a very simple refinement over the thickness, accurate results were obtained.
- Since the temperature is mainly a 3D effect and its coupling with the elastic field is 3D too, ITSDT clearly yields better thermo-elastic responses than TSDT.
- In the thermo-elastic analysis, the coupling term between the thermal and elastic fields in the heat equation slows down the structure to reach its equilibrium point. In other words, the coupled analysis considers that the energy due to heat conduction are two parts: one that causes the evolution of the thermal field and the other one that produces the changes in the elastic field.
- When a dynamical thermo-piezo-mechanical system is studied, we can notice that the electrical field acts faster than the other fields either for the coupled or uncoupled analysis.
- Using ITSDT , some active vibration control strategies were tested, such as the negative velocity feedback and LQR. As expected, increase in the damping of

the structure is achieved. Moreover, we verified that LQR performs better since it is based in optimization principles.

REFERENCES

- [1] Giurgiutiu, V., Rogers, C.A., and Chaudhary, Z., 1996, "Energy-Based Comparison of Solid-State Induced-Strain Actuators," *Journal of Intelligent Material Systems and Structures*, **7**, pp. 4–14.
- [2] Bayley, A., and Hubbard, J. E., 1985, "Distributed Piezoelectric-Polymer Active Vibration Control of a Cantilevered Beam," *Journal of Guidance, Control, and Dynamics*, **8**, pp. 605–611.
- [3] Hanagud, S., Obal, M.W., and Calise, A. J., 1992, "Optimal Vibration Control by the Use of Piezoelectric Sensors and Actuators," *Journal of Guidance, Control, and Dynamics*, **15**, pp. 1199–1206.
- [4] Dosh, J. J., Inman, D. J., and Garcia, E., 1992, "A Self-Sensing Actuator for Collocated Control," *Journal of Intelligent Material Systems and Structures*, **3**, pp. 166–185.
- [5] Anderson, E.H., and Hagood, N.W., 1994, "Simultaneous Piezoelectric Sensing/actuation: Analysis and Application to Controlled Structures," *Journal of Sound and Vibration*, **174**, pp. 617–639.
- [6] Qui, J., and Tani, J., 1995, "Vibration control of a Cylindrical Shell Using Distributed Piezoelectric Sensors and Actuators," *Journal of Intelligent Material Systems and Structures*, **6**, pp. 474–481.
- [7] Allik H, Hughes T.J.R., 1970, "Finite Element Method for Piezoelectric Vibration," *International Journal of Numerical Methods in Engineering*, **2**, pp. 151–157.

- [8] Allik H, Webman, K.M., Hunt, J.T., 1974, "Vibrational Response of Sonar Transducers Using Piezoelectric Finite Elements," *Journal of the Acoustical Society of America*, **56**, pp. 1782–1791.
- [9] Tzou, H.S., Tseng, C.I., 1990, "Distributed Piezoelectric Sensor/Actuator Design for Dynamic Measurement/Control of Distributed Parameter System: A Piezoelectric Finite Element Approach," *Journal of Sound and Vibration*, **138**, pp. 17–24.
- [10] Reddy, J.N, 1987, "A Generalization of Two-Dimensional Theories of Laminated Composite Plates," *Communications in Applied Numerical Methods*, **3**, pp. 173–180.
- [11] Mitchell, J.A., and Reddy, J.N., 1995, "A Refined Hybrid Plate Theory for Composite Laminates of Piezoelectric Laminae," *International Journal of Solids and Structures*, **32**, pp. 2345–2367.
- [12] Saravanos, D.A., and Heyliger, P.R., 1995, "Coupled Layerwise Analysis of Composite Beams with Embedded Piezoelectric Sensors and Actuators," *Journal of Intelligent Material Systems and Structures*, **6**, pp. 350–363.
- [13] Crawley, E., and Anderson, E., 1990, "Detailed Models of Piezoceramic Actuation of Beams," *Journal of Intelligent Material Systems and Structures*, **1**, pp. 4–25.
- [14] Ghiringhelli, G.L., Masarati, P., and Mantegazza, P., 1997, "Characterization of Anisotropic Non-Homogeneous Beam Sections with Embedded Piezoelectric Materials," *Journal of Intelligent Material Systems and Structures*, **8**, pp. 842–858.

- [15] Raja, S., Rohwer, K., and Rose, M., 1999, “Piezothermoelastic Modeling and Active Vibration Control of Laminated Composite Beams,” *Journal of Intelligent Material Systems and Structures*, **10**, pp. 890–899.
- [16] Robbins, D.H., and Reddy, J.N., 1991, “Analysis of Piezoelectrically Actuated Beams Using a Layer-Wise Displacement Theory,” *Computers and Structures*, **41**, pp. 265–279.
- [17] Benjeddou, a., Trindade, M. A., and Ohayon, R., 1997, “A Unified Beam Finite Element Model for Extension and Shear Piezoelectric Actuation Mechanisms,” *Journal of Intelligent Material Systems and Structures*, **8**, pp. 1012–1025.
- [18] Agnes, G.S., and Napolitano, K., 1993, “Active Constrained Layer Viscoelastic Damping.” *34th AIAA/ASME/ASCE/AHS/ASC Structures, Structural Dynamics, and Materials Conference*, AIAA, Reston, VA, pp. 3499–3506.
- [19] Lesieutre, G.A., and Lee, U., 1996, “A Finite Element for Beam Having Segmented Active Constrained Layers with Frequency-Dependent Viscoelasticities,” *Smart Materials and Structures*, **5**, pp. 615–627.
- [20] Crassidis, J., Baz, A., and Wereley, N., 2000, “ H_∞ Control of Active Constrained Layer Damping,” *Journal of Vibration and Control*, **6**, pp. 113–136.
- [21] Galucio, A.C., Deu, J-F., and Ohayon, R. 2005, “A Fractional Derivative Viscoelastic Model for Hybrid Active-Passive Treatments in Time Domain-Application to Sandwich Beams,” *Journal of Intelligent Material Systems and Structures*, **16**, pp. 33–45.
- [22] Crawley, E.F., and Lazarus, K.B., 1991, “Induced Strain Actuation of Isotropic and Anisotropic Plates,” *AIAA Journal*, **23**, pp. 944–951.

- [23] Lee, C.K., 1990, "Theory of Laminated Piezoelectric Plates for the Design of Distributed Sensors/Actuators: Part I: Governing Equations and Reciprocal Relationships," *Journal of Acoustical Society of America*, **87**, pp. 1144–1158.
- [24] Lee, C.K., 1992, "Piezoelectric Laminates: Theory and Experiment for Distributed Sensors and Actuators," *Intelligent Structural Systems*, edited by H.S. Tzou and G.L. Anderson, Kluwer Academic, Norwell, MA, pp. 75–168.
- [25] Suleman, A., Venkayya, V.B., 1995, "A Simple Finite Element Formulation for a Laminated Composite Plate with Piezoelectric Layers," *Journal of Intelligent Materials and Structures*, **6**, pp. 776–782.
- [26] Yin, L., Shen, Y., 1997, "Strain Sensing of Composite Plates Subjected to Low Velocity Impact with Distributed Piezoelectric Sensors: A Mixed Finite Element Approach," *Journal of Sound and Vibration*, **199**, pp. 17–31.
- [27] Bisegna, P., and Maceri, F., 1996, "A Consistent Theory of Thin Piezoelectric Plates," *Journal of Intelligent Material Systems and Structures*, **7**, pp. 372–389.
- [28] Reddy, J.N., 1984, "A Simple Higher-Order Theory for Laminated Plates," *Journal of Applied Mechanics*, **51**, pp. 745–752.
- [29] Reddy, J.N., 1987, "A Generalization of Two-Dimensional Theories of Laminated Composite Plates," *Communications in Applied Numerical Methods*, **3**, pp. 173–180.
- [30] Mitchell, J.A., and Reddy, J.N., 1995, "A Refined Hybrid Plate Theory for Composite Laminates of Piezoelectric Laminae," *International Journal of Solids and Structures*, **32**, pp. 2345–2367.

- [31] Heyliger P.R., Ramirez G., Saravanos D.A., 1994, “Coupled Discrete-Layer Finite Elements for Laminated Piezoelectric Plates,” *Communications in Numerical Methods in Engineering*, **10**, pp. 971–981.
- [32] Saravanos, D.A., Heyliger, P.R., Hopkins, D.A., 1997, “Layerwise Mechanics and Finite Element for the Dynamic Analysis of Piezoelectric Composite Plates,” *International Journal of Solids and Structures*, **34**, pp. 359–378.
- [33] Reddy, J.N., and Cheng, Z.Q., 2001, “Three-dimensional Solutions of Smart Functionally Graded Plates,” *Journal of Applied Mechanics*, **68**, pp. 234–241.
- [34] Chattopadhyay, A., Steely, C.E., 1997, “A Higher Order Theory for Modeling Composite Laminates with Induced Strain Actuators,” *Composites Part B*, **28B**, pp. 243–252.
- [35] Chattopadhyay, A., Li, J., and Gu, H., 1999, “Coupled Thermo-Piezoelectric-Mechanical Model for Smart Composite Laminate,” *AIAA Journal*, **37**, pp. 1633–1638.
- [36] Zhou, X., Chattopadhyay, A., and Gu, H., 2000, “Dynamic Response of Smart Composites Using a Coupled Thermo-Piezoelectric-Mechanical Model,” *AIAA Journal*, **38**, pp. 1939–1948.
- [37] Reddy, J.N., 2006, *An Introduction to the Finite Element Method*, 3rd ed., McGraw-Hill, New York.
- [38] Reddy, J.N., 2004, *An Introduction to Nonlinear Finite Element Analysis*, Oxford University Press, Oxford, UK.
- [39] Reddy, J.N., 1997, *Mechanics of Laminated Composite Plates and Shells, Theory and Analysis*, 2nd ed., CRC Press, Boca Raton, FL.

- [40] Tiersten, H.F., 1969, *Linear Piezoelectric Plate Vibrations*, Plenum Press, New York.
- [41] Malvern, L.E., 1969, *Introduction to the Mechanics of a Continuous Medium*, Prentice-Hall Inc., New Jersey.
- [42] Turteltaub, S., 2002, “Optimal Control and Optimization of Functionally Graded Materials for Thermomechanical Processes,” *International Journal of Solids and Structures*, **39**, pp. 3175–3197.
- [43] Pagano, N. J., 1967, “Exact Solutions for Composite Laminates in Cylindrical Bending,” *Journal of Composite Materials*, **3**, pp. 398–411.
- [44] Pagano, N. J., 1970, “Exact Solutions for Rectangular Bidirectional Composites and Sandwich Plate,” *Journal of Composite Materials*, **4**, pp. 20–34.
- [45] Trindade, M. A., 2000, *Contrôle Hybride Actif-Passif des Vibrations de Structures par des Matériaux Piézoélectriques et Viscoélastiques: Poutres Sandwich/Multicouches Intelligentes*, Conservatoire National des Arts et Métiers, Paris, France.

Supplementary References

- Bisegna, P., and Caruasa, G., 2000, “Mindlin-Type Finite Elements for Piezoelectric Sandwich Plates,” *Journal of Intelligent Material Systems and Structures*, **11**, pp. 14–25.
- Lam, M.J., Inman D.J., and Saunders, W.R., 1997, “Vibration Control through Passive Constrained Layer Damping and Active Control,” *Journal of Intelligent Material Systems and Structures*, **8**, pp. 663–677.

- Robbins D.H., and Reddy, J.N., 1996, “An Efficient Computational Model for the Stress Analysis of Smart Plate Structures,” *Smart Materials and Structures*, **5**, pp. 353–360.
- Shen, M.H., 1994, “Analysis of Beams Containing Piezoelectric Sensors and Actuators,” *Smart Materials and Structures*, **3**, 439–447.
- Shen, M.H., 1995, “A New Modeling Technique for the Piezoelectric Actuated Beams,” *Computers and Structures*, **57**, pp. 361–366.
- Varadan, V.V., Lim, Y.-H., and Varadan, V.K., 1996, “Closed Loop Finite-Element Modeling of Active/Passive Damping in Structural Vibration Control,” *Smart Materials and Structures*, **5**, pp. 685–694.

APPENDIX A

MATERIAL PROPERTY RELATIONS

For a two-phase composite plate, matrix (1) and particulate (2) phase, reinforced by a random distribution of spherical particles in the plane of the plate, the locally effective Bulk Modulus can be calculated as

$$\frac{K - K_1}{K_2 - K_1} = \frac{V_2 \left(K_1 + \frac{4}{3} \mu_1 \right)}{\left(K_1 + \frac{4}{3} \mu_1 \right) + (1 - V_2)(K_2 - K_1)} \quad (\text{A.1})$$

and the Shear Modulus

$$\frac{\mu - \mu_1}{\mu_2 - \mu_1} = \frac{V_2(\mu_1 + \pi_1)}{(\mu_1 + \pi_1) + (1 - V_2)(\mu_2 - \mu_1)} \quad (\text{A.2})$$

where

$$\pi_1 = \frac{\mu_1(9K_1 + 8\mu_1)}{6(K_1 + 2\mu_1)} \quad (\text{A.3})$$

and V_2 is the volume fraction of the particular phase. Eqs. A.1 and A.2 are very well-known as Mori-Tanaka estimates. Moreover, the locally effective heat conductivity coefficient κ can be obtained from

$$\frac{\kappa - \kappa_1}{\kappa_2 - \kappa_1} = \frac{3V_2\kappa_1}{3\kappa_1 + (1 - V_2)(\kappa_2 - \kappa_1)} \quad (\text{A.4})$$

and the coefficient of thermal expansion is given by

$$\frac{\alpha - \alpha_1}{\alpha_2 - \alpha_1} = \frac{1/K - 1/K_1}{1/K_2 - 1/K_1} \quad (\text{A.5})$$

APPENDIX B

MODEL REDUCTION

Modal Analysis is a very popular technique in vibration problems. According to this, the dynamic of a structure can be expressed as the summation of fundamental modes which are orthogonal among them. It is important to point out that in many cases, some modes are more relevant than the other ones. For instance, if the system is excited in a determined frequency range, the modes corresponding to frequencies outside this range are not going to contribute significantly to the structure dynamics; therefore, they can be neglected. In other words, we are performing a system reduction which makes the system more computationally tractable. Here, we are going to use the approach used in [45].

For a linear system represented by Eq. 5.24, the right and the left eigenvectors of the system matrix A holds the following condition

$$AT_r = \Lambda T_r \quad ; \quad A^T T_l = \Lambda T_l \quad (\text{B.1})$$

with $T_r^T T_l = I$. Let's express Λ as

$$\Lambda = \begin{bmatrix} \Lambda_r & 0 \\ 0 & \Lambda_n \end{bmatrix} \quad (\text{B.2})$$

this is similar to decompose the matrices T_r and T_l

$$T_r = \begin{bmatrix} T_{rr} & T_{rn} \end{bmatrix} \quad ; \quad T_l = \begin{bmatrix} T_{lr} & T_{ln} \end{bmatrix} \quad (\text{B.3})$$

Then, if $x \approx T_{rr} x_r$

$$\dot{x}_r = \Lambda_r x_r + T_{lr}^T B u + T_{lr}^T p$$

$$\hat{B} = T_c T_l^T T_r B = \begin{bmatrix} \cdot \\ \cdot \\ \cdot \\ \text{Im}(\psi_j)/\text{Im}(\lambda_j) \\ \cdot \\ \cdot \\ \cdot \\ \text{Re}(\psi_j) + \text{Im}(\psi_j) (\text{Re}(\lambda_j)/\text{Im}(\lambda_j)) \\ \cdot \\ \cdot \\ \cdot \end{bmatrix} \quad (\text{B.10})$$

$$\hat{p} = T_c T_l^T T_r p = \begin{bmatrix} \cdot \\ \cdot \\ \cdot \\ \cdot \\ \text{Im}(\varphi_j)/\text{Im}(\lambda_j) \\ \cdot \\ \cdot \\ \cdot \\ \text{Re}(\varphi_j) + \text{Im}(\varphi_j) (\text{Re}(\lambda_j)/\text{Im}(\lambda_j)) \\ \cdot \\ \cdot \\ \cdot \end{bmatrix} \quad (\text{B.11})$$

$$\hat{C} = C T_{rr} T_c^{-1} = \begin{bmatrix} \cdot & \cdot & -2 [\text{Re}(\phi_j) \text{Re}(\lambda_j) + \text{Im}(\phi_j) \text{Im}(\lambda_j)] & \cdot & \cdot & 2 \text{Re}(\phi_j) & \cdot & \cdot \end{bmatrix} \quad (\text{B.12})$$

VITA

James Wilson Aliaga Salazar was born in March 1975, in Lima, Peru. He received his B.S. degree from Universidad Nacional de Ingenieria, Peru in 1997 and M.S. degree from Pontificia Universidade Catolica do Rio de Janeiro, Brazil in 2000, both in mechanical engineering. He received his Ph.D. degree in mechanical engineering in August 2006 from Texas A&M University. His research interests include finite element analysis and identification and control of structures. Mr. Aliaga's permanent address is:

Calle 2 181 int 16 La Florida, Rimac

Lima

Peru

Email: jwaliaga@hotmail.com

The typist for this dissertation was James Wilson Aliaga Salazar.